Fakultät Mathematik und Naturwissenschaften Institut für Kern- und Teilchenphysik

Determination of muon reconstruction efficiencies in the ATLAS detector using a tag & probe approach in $Z \to \mu\mu$ events

CERN-THESIS-2011-058
16 August 2011

Diplomarbeit
zur Erlangung des akademischen Grades
Diplom-Physiker

vorgelegt von

Tino Michael
geboren am 1.6.1987 in Cottbus

INSTITUT FÜR KERN- UND TEILCHENPHYSIK
DER TECHNISCHEN UNIVERSITÄT DRESDEN
2011

Eingereicht am 08.08.2011

1. Gutachter: Prof. Dr. Michael Kobel
2. Gutachter: Jun.-Prof. Dr. Arno Straessner

Abstract

Of all detectable Standard Model particles produced through proton-proton collisions at the LHC, muons are the only ones reaching the outermost layers of the ATLAS detector. They are a potent and clean tool to examine known and unknown physics processes as well as to monitor detector effects and performance. Measuring the efficiency of muon reconstruction algorithms is one essential tool to conduct searches for the Higgs boson and particles beyond the Standard Model. To determine those efficiencies, an implementation of the "Tag & Probe" method has been developed. This method was tested, using the data recorded by the ATLAS detector at a center of mass energy of $7\ \mathrm{TeV}$ in the year 2010. The efficiencies were measured on a sub-sample of jet associated $\mu^+\mu^-$ final states.

Kurzdarstellung

Von allen nachweisbaren Elementarteilchen des Standadmodells, die bei Proton-Proton Kollisionen am LHC erzeugt werden können, sind Myonen die einzigen, welche die äußeren Lagen des ATLAS-Detektors erreichen. Diese Myonen bieten eine vielversprechende Möglichkeit, sowohl neue als auch bereits bekannte, physikalische Prozesse zu untersuchen und die Leistungsfähigkeit des Detektors zu überwachen. Die Messung der Myon-Rekonstruktionseffizienzen ist wichtig für die Suche nach dem Higgs-Boson und neuen Teilchen, die von Theorien zur Erweiterung des Standardmodells vorhergesagt werden. Zur Bestimmung dieser Effizienzen wurde eine „Tag & Probe"-Methode entwickelt und an den Daten getestet, die der ATLAS-Detektor im Jahre 2010 bei einer Schwerpunktsenergie von $7\ \mathrm{TeV}$ aufgezeichnet hat. Die Effizienzen wurden in einer Untermenge an Ereignissen mit Jet-assoziierten Zwei-Myon-Endzuständen gemessen.

Contents

1. Introduction

Physics has come a long way since the ancient Greek tried to understand our world only with the power of their minds: Galileo Galilei studied the motion of free fall in the 16^{th} century whilst taking the time with his pulse, Sir Isaac Newton laid the foundations of analytical physics with his *Philosophiæ Naturalis Principia Mathematica* in the late 17^{th} century. At the beginning of the 20^{th} century the two cornerstones of modern physics were developed: Quantum mechanics and Einstein's general relativity. Quantum mechanics was soon refined to include the concepts of special relativity. The result was the principle of quantum field theory, where our current knowledge of particle physics is condensed into the *Standard Model of Particle Physics*. This Standard Model is a local gauge theory, where physics is described as discrete interactions of spin 1/2 fermions through exchange of spin 1 gauge bosons. All but one of the particles predicted by the Standard Model have been found. The only missing piece is the *Higgs boson* which is held responsible for the origin of mass of the elementary particles.
Searching for the Higgs boson is one of the major tasks of the Large Hadron Collider (LHC) near Geneva at the Franco-Swiss border. The LHC particle accelerator collides two beams of either protons at a center of mass energy of up to $14\ \mathrm{TeV}$ (2.24 µJ) or lead nuclei up to $1148\ \mathrm{TeV}$ (184 µJ) by design. One of the experiments at the LHC is the ATLAS detector which is capable of detecting and identifying a large variety of particles that can arise in the nuclei collisions. One of those particles is the muon which is heavy enough to reach the outer layers of the detector without being completely absorbed on its way, but light enough to not decay before it reaches the outer edge. This unique detector signature and the various processes it can originate from make it an excellent probe for new physics studies, like the search for Supersymmetry or the Higgs boson, but also to measure already known processes like jet associated production of W and Z bosons.
This thesis uses the well known kinematic properties of the decay of Z bosons into a muon pair to measure the efficiencies those muons are reconstructed with. For this task, a pure $Z \to \mu\mu$ subsample is selected from the data recorded by ATLAS in the year 2010 (corresponding to an integrated luminosity of $34\ \mathrm{pb}^{-1}$, see section 2.2) at a center of mass energy of $7\ \mathrm{TeV}$ and then a tag & probe method is applied onto this set of events. As a cross-check these results are also compared to the efficiencies found in Monte Carlo event simulations.

The muon reconstruction efficiency will be determined in dependence of various phase space regions and jet variables.

Throughout this thesis natural units are used, setting the speed of light and Planck's reduced constant to unity: $c = \hbar = 1$. This renders mass and momentum as well as inverse length and inverse time to be measured in units of energy. The energy unit used is the electron volt (eV), which is the energy a particle, carrying an elementary charge of $\mathrm{e} = 1.602176487(40) \times 10^{-19}$ C, acquires while traversing an electrical potential difference of one volt.

2. Theoretical Framework

This chapter gives an overview of the theory used in particle physics and how observables can be derived from that theory.

2.1. Standard Model of Particle Physics

The Standard Model is one of the most successful theories in the history of physics. It is a quantum field theory and describes with high precision the basic building blocks of matter and three of the four known, fundamental forces acting between them, namely: the electromagnetic, the weak and the strong interaction[1]. The fourth fundamental interaction—the gravitational force—is weaker by several orders of magnitude and negligible on the energy scales accessible with modern machineries (e.g. the Large Hadron Collider, see section 3.1)[2]. The theory of gravitation—Einstein's General Relativity—is a classical field theory where the interaction of any form of energy (e.g. mass, kinetic energy, binding energy) is described by the curvature of space-time itself[3]. Despite all efforts it still lacks a consistent quantum field theoretical description.

In the framework of the Standard Model, elementary particles are represented as four dimensional Dirac Spinors ψ with half-integer spin obeying Fermi-Dirac statistics. Those fermions appear as

quarks *q* interacting through all three fundamental forces and

leptons *l* which do not take part in the strong interaction.

Leptons can furthermore be divided into charged leptons $l^{\pm}$ and neutrinos ν, where the latter interact neither electromagnetically nor strongly. All those particles can be grouped into three families, where the corresponding particles from the different families have nearly identical properties but increasing mass. An overview of these particles is given in table 2.1.

Even though neutrinos were considered massless in the past, experiments have shown oscillations induced by mass differences between the neutrinos of these three families[4]. This proves that at least two of those three neutrino types have non-vanishing rest masses. The values given in table 2.1 are upper limits originating from the combination of various experiments[5].

Table 2.1.: The Elementary particles of the Standard Model with their charges and masses[5].

Family	Particle		Charge / e	Mass
I	e	electron	-1	0.511 MeV
	ν_e	electron neutrino	± 0	< 2 eV
	u	up-quark	$+2/3$	$2.49^{+0.81}_{-0.79}$ MeV
	d	down-quark	$-1/3$	$5.05^{+0.75}_{-0.95}$ MeV
II	μ	muon	-1	106 MeV
	ν_μ	muon neutrino	± 0	< 0.19 MeV
	c	charm-quark	$+2/3$	$1.27^{+0.07}_{-0.09}$ GeV
	s	strange-quark	$-1/3$	$3.77^{+1.03}_{-0.77}$ MeV
III	τ	tauon	-1	1777 MeV
	ν_τ	tau neutrino	± 0	< 18.2 MeV
	t	top-quark	$+2/3$	$(172.0 \pm 0.9 \pm 1.3)$ GeV
	b	bottom-quark	$-1/3$	$4.19^{+0.18}_{-0.06}$ GeV

For every particle there is an anti-particle incorporating the same rest mass but carrying opposite charge.
The forces are described by local gauge theories, where each generator of a gauge group corresponds to an (apparently) massless spin 1 gauge boson. The Standard Model is based on the $SU(3)_C \otimes SU(2)_L \otimes U(1)_Y$ symmetry group and a Lagrangian density function $\mathscr{L}$ that has to be invariant under the symmetry transformations of those groups.

2.1.1. Quantum Chromodynamics, QCD

The strong interaction is described by the $SU(3)_C$ sub-group, where "C" denotes the *color*-charge which strongly interacting particles carry. With the $SU(3)_C$, eight massless gluons G^i and a strong coupling constant g_s arise. Due to the shape of the strong force's potential, quarks and gluons, as the carriers of color charge, are confined and cannot exist as free particles[6]. They are bound to color-singlet states, called *hadrons*, consisting of a quark-antiquark-pair (*meson*) or a quark triplet (*baryon*). Due to this confinement, quarks, generated in particle collisions, form *jets*, i.e. cascades of multiple hadrons. In figure 2.1 some examples for quark and gluon interactions are given.

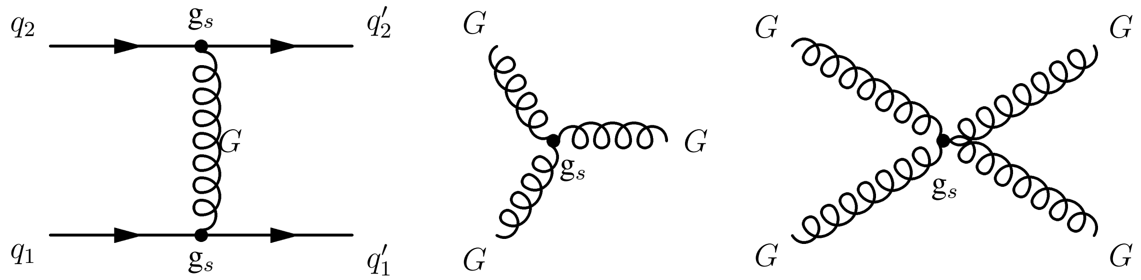

Figure 2.1.: Quark-quark-scattering via gluon exchange (left); three- (middle) and four-point (right) gluon self-interaction

The full, gauge invariant QCD Lagrangian that describes the dynamics of the quarks and gluons is given as:

$$\begin{aligned} \mathscr{L}_{\text{QCD}} = \quad & \overline{\psi}_\alpha i\gamma^\mu \partial_\mu \psi_\alpha && \text{kinetic term of the quark field} \\ - \quad & \mathrm{g_s}\overline{\psi}_\alpha \gamma^\mu \mathrm{T}^a_{\alpha\beta} G^a_\mu \psi_\beta && \text{interaction term between quarks and gluons} \\ - \quad & m\overline{\psi}_\alpha \psi_\alpha && \text{quark-mass term} \\ - \quad & \tfrac{1}{4} G^a_{\mu\nu} G^{a,\,\mu\nu}. && \text{kinetic term of gluon field} \end{aligned} \tag{2.1}$$

Here, $G^a_{\mu\nu} = \partial_\mu G^a_\nu - \partial_\nu G^a_\mu - \mathrm{g_s} f^{abc} G^b_\mu G^c_\nu$ denotes the field strength tensor of the gluon field G^a_μ with f^{abc} as the structure constants of SU(3). The covariant derivative $(D^\mu)_{\alpha\beta} = \delta_{\alpha\beta}\partial^\mu - \mathrm{g_s}\mathrm{T}^a_{\alpha\beta}G^a_\mu$, where $\mathrm{T}^a_{\alpha\beta}$ is the strong isospin—the generator of SU(3)$_\mathrm{C}$, ensures gauge invariance of the Lagrangian and introduces the coupling of the gluon and quark fields. Furthermore, $\alpha,\, \beta = 1,\, 2,\, 3$ or $red,\, blue,\, green$ are the the color charges, $\mu,\, \nu = 0 \cdots 3$ are Lorentz indices and $a = 1\, \cdots\, 8$ refers to the eight different gluon fields.

Even though QCD is mathematically well formulated, higher order terms get overly complex to solve analytically and therefore have to be approximated[7]. One straight forward and systematically improvable approach at high energies is to use a perturbative approximation, involving a series expansion in the strong coupling $\mathrm{g_s}$. Consequently, cross sections are written in the form: $\sigma = \mathrm{c}_0 + \mathrm{c}_1\mathrm{g_s} + \mathrm{c}_2\mathrm{g_s^2} + \mathrm{c}_3\mathrm{g_s^3} + \cdots$. Therefore, an improvement in the cross section estimate can be obtained by calculating one further coefficient c_i. Even though the strong coupling at energy scales of the LHC yields $\mathrm{g_s}(\mathrm{m_Z}) = 0.118$, second order calculations can modify the cross sections by a factor of 2 (e.g. Higgs production[8]) up to $\mathscr{O}(50)$ in $Z + jets$ events[9].

This perturbative approach is not longer applicable when the color-charged particles diverge. Here, non-perturbative models are used to estimate the hadronization of the partons, i.e. the cascade of the quarks and gluons into jets[10].

2.1.2. Electroweak Mixing

Until now, there is no known, autonomous theory of weak interaction, but Sheldon Lee Glashow, Abdus Salam and Steven Weinberg contributed to the combination of electromagnetism and weak interaction to a unified electroweak theory[11, 12, 13], for which they were jointly awarded the Nobel Prize in physics in 1979[(1)][14].
The electroweak $\mathrm{SU}(2)_\mathrm{L}\otimes\mathrm{U}(1)_\mathrm{Y}$ sub-group incorporates chiral symmetry and, as the "L" subscript implies, the gauge bosons of $\mathrm{SU}(2)_\mathrm{L}$, W_μ^j $(j = 1, 2, 3)$, only act on left-handed fermions. The left- and right-handed fermion fields are defined as:

$$\psi_{\mathrm{L/R}} = \frac{1}{2}\left(1 \mp \gamma_5\right)\psi. \tag{2.2}$$

Here, $\gamma_5 = i\gamma_0\gamma_1\gamma_2\gamma_3$ and $\gamma_{0\cdots3}$ are the *Dirac matrices*. The corresponding generator is the weak isospin T_W^j and the coupling constant is g_1. Left-handed fermion fields form isospin-doublets, right-handed fields are isospin-singlets (see table 2.2).
From the abelian $\mathrm{U}(1)_\mathrm{Y}$, gauge bosons B_μ arise, coupling to both left- and right-handed fermions with coupling constant g_2. "Y" refers to the weak hypercharge. The electroweak Lagrangian reads:

$$\mathscr{L}_{\mathrm{EW}} = \overline{F}_\mathrm{L} i\gamma^\mu D_\mu F_\mathrm{L} + \overline{f}_\mathrm{R} i\gamma^\mu D_\mu f_\mathrm{R} - \frac{1}{4}(W_{\mu\nu}^j W^{j,\mu\nu} + B_{\mu\nu}B^{\mu\nu}), \tag{2.3}$$

implying a summation over all left-handed isospin-doublets F_L and right-handed isospin-singlets f_R. The terms can be interpreted similarly to the ones in equation (2.1). The covariant derivative $D_\mu = \partial_\mu + i\mathrm{g}_1\vec{\mathrm{T}}_\mathrm{W}\vec{W}_\mu + i\mathrm{g}_2\mathrm{Y}B_\mu$ again provides both gauge invariance and the fermion-boson interaction. A fermion mass term like $m\overline{\psi}\psi = m(\overline{\psi}_\mathrm{L}\psi_\mathrm{R} + \overline{\psi}_\mathrm{R}\psi_\mathrm{L})$ would not be gauge invariant and is thus forbidden. Gauge invariant terms for the fermion masses arise through the coupling to a complex, scalar Higgs field $\phi = (\phi^+,\, \phi^0)^\mathrm{T}$ with a Lagrangian:

$$\mathscr{L}_{\mathrm{Higgs}} = (D^\mu\phi)^\dagger D_\mu\phi - V(\phi). \tag{2.4}$$

The Higgs potential $V(\phi)$ has the form

$$V(\phi) = \mu^2\phi^\dagger\phi + \lambda(\phi^\dagger\phi)^2, \tag{2.5}$$

where $\mu^2 < 0$ causes *spontaneous symmetry breaking* with a non-zero vacuum expectation value $\langle 0|\phi|0\rangle = v = \sqrt{\frac{-\mu^2}{\lambda}}$ (see figure 2.2). Due to vacuum stability, λ has to be positive. Otherwise, the potential would open downwards preventing a global, finite minimum. After spontaneous

[1] *"... for their contributions to the theory of the unified weak and electromagnetic interaction between elementary particles, including, inter alia, the prediction of the weak neutral current"*

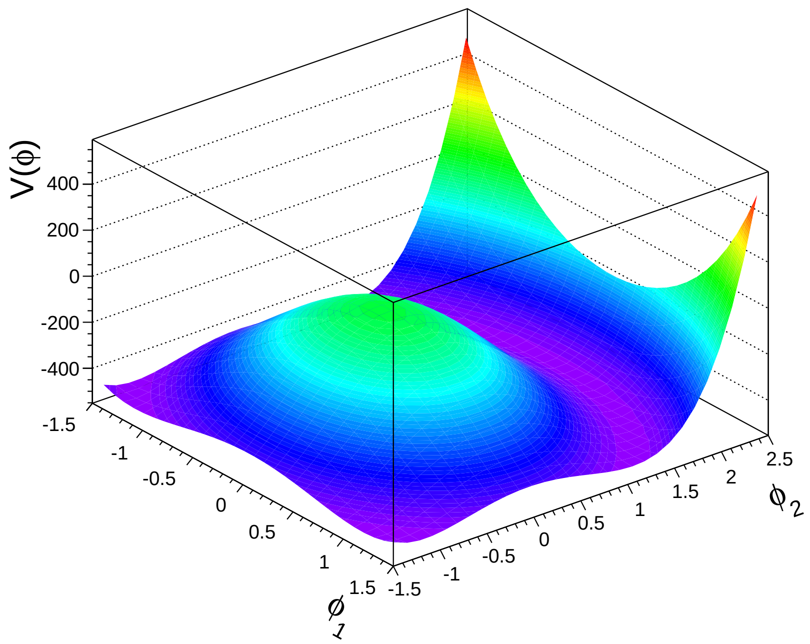

Figure 2.2.: Higgs potential $V(\phi)$ with $\phi^+ = 0,\ \phi^0 = \phi_1 + i\phi_2$, $\mu^2 < 0$ and therefore non-zero $v = \langle 0|\phi|0\rangle$. The units on the axes are completely arbitrary.

symmetry breaking, B_μ and W^3_μ are mixed into the massless photon A_μ and the massive Z boson Z_μ essentially by rotating the (B_μ, W^3_μ)-plane by the *weak mixing angle* ϑ_W:

$$\begin{pmatrix} A_\mu \\ Z_\mu \end{pmatrix} = \begin{pmatrix} \cos\vartheta_\mathrm{W} & \sin\vartheta_\mathrm{W} \\ -\sin\vartheta_\mathrm{W} & \cos\vartheta_\mathrm{W} \end{pmatrix} \begin{pmatrix} B_\mu \\ W^3_\mu \end{pmatrix}, \tag{2.6}$$

whilst the W^1_μ and W^2_μ superpose to the charged, massive W^+_μ and W^-_μ:

$$W^\pm_\mu = \frac{W^1_\mu \mp iW^2_\mu}{\sqrt{2}}. \tag{2.7}$$

The weak mixing angle is defined by the ratio of the coupling constants of the B_μ and W^j_μ fields, g_1 and g_2:

$$\tan\vartheta_\mathrm{W} = \frac{\mathrm{g}_1}{\mathrm{g}_2}. \tag{2.8}$$

Fermionic and bosonic mass terms induced by the Higgs field are given by:

$$\mathscr{L}_\mathrm{mass} = -\frac{v}{\sqrt{2}} \sum_f c_f \overline{\psi}_f \psi_f + \left(\frac{v\mathrm{g}_2}{2}\right)^2 W^{+\mu} W^-_\mu + \frac{(\mathrm{g}_1^2 + \mathrm{g}_2^2)v^2}{8} Z^\mu Z_\mu. \tag{2.9}$$

Table 2.2.: The weak isospin-multiplets with their quantum numbers weak hypercharge Y, third component of weak isospin $\mathrm{T_W^3}$ and electrical charge Q.

Fermions			Y	$\mathrm{T_W^3}$	Q
Leptons					
$\begin{pmatrix} \nu_e \\ e \end{pmatrix}_\mathrm{L}$	$\begin{pmatrix} \nu_\mu \\ \mu \end{pmatrix}_\mathrm{L}$	$\begin{pmatrix} \nu_\tau \\ \tau \end{pmatrix}_\mathrm{L}$	$1/2$ $-1/2$	$-1/2$ $-1/2$	0 -1
$\nu_{\mathrm{e,\,R}}$	$\nu_{\mu,\,\mathrm{R}}$	$\nu_{\tau,\,\mathrm{R}}$	0	0	0
e_R	μ_R	τ_R	0	-1	-1
Quarks					
$\begin{pmatrix} u \\ d' \end{pmatrix}_\mathrm{L}$	$\begin{pmatrix} c \\ s' \end{pmatrix}_\mathrm{L}$	$\begin{pmatrix} t \\ b' \end{pmatrix}_\mathrm{L}$	$1/2$ $-1/2$	$1/6$ $1/6$	$2/3$ $-1/3$
u_R	c_R	t_R	0	$2/3$	$2/3$
d'_R	s'_R	b'_R	0	$-1/3$	$-1/3$

The weak mixing angle is also given by the ratio of the W and Z boson masses:

$$\frac{\mathrm{M_W}}{\mathrm{M_Z}} = \cos\vartheta_\mathrm{W}. \tag{2.10}$$

The weak hypercharge Y and the third componend of the weak isospin $\mathrm{T_W^3}$ are combined to an electrical charge in a way that the couplings of photon and Z boson match the phenomenological prescriptions (i.e. no photon-neutrino-interactions):

$$\mathrm{Q} = \mathrm{Y} + \mathrm{T_W^3}. \tag{2.11}$$

Electrical charge, weak hypercharge, and weak isospin of the fermion fields are listed in table 2.2. The down-type quarks take part in interactions as *flavor eigenstates* d', s' and b' but propagate through space-time as *mass eigenstates* d, s and b. The discrepancy between those quantum states is described by the CKM-matrix[(2)]:

$$\begin{pmatrix} d' \\ s' \\ b' \end{pmatrix} = \begin{pmatrix} \mathrm{V_{ud}} & \mathrm{V_{us}} & \mathrm{V_{ub}} \\ \mathrm{V_{cd}} & \mathrm{V_{cs}} & \mathrm{V_{cb}} \\ \mathrm{V_{td}} & \mathrm{V_{ts}} & \mathrm{V_{tb}} \end{pmatrix} \cdot \begin{pmatrix} d \\ s \\ b \end{pmatrix}, \tag{2.12}$$

which technically gives the probability of the transition from a quark of flavor i into a quark of flavor j via weak interactions. This probability is proportional to $|\mathrm{V_{ji}}|^2$.

[2]Makoto Kobayashi and Toshihide Maskawa introduced this matrix, based on the work of Nicola Cabibbo, to preserve the universality of the weak interactions.

The choice of mixing the down-type quarks is purely arbitrary. One could also define the matrix for the up-type quarks and receive the same matrix, due to its unitarity. Fitting to experimental data yields[5]:

$$\mathrm{V_{CKM}} = \begin{pmatrix} 0.97428 \pm 0.00015 & 0.2253 \pm 0.0007 & 0.003477^{+0.00016}_{-0.00012} \\ 0.2252 \pm 0.0007 & 0.97345^{+0.00015}_{-0.00016} & 0.0410^{+0.0011}_{-0.0007} \\ 0.00862^{+0.00026}_{-0.00020} & 0.0403^{+0.0011}_{-0.0007} & 0.999152^{+0.000030}_{-0.000045} \end{pmatrix}. \quad (2.13)$$

The muon decay, first described by Enrico Fermi through an effective four-point theory[15, 16], is shown as an example of electroweak interaction in figure 2.3.
Table 2.3 gives an overview of the fundamental forces and the particles mediating them.

There are also proposals of non-local quantum field theories that produce mass without introducing a Higgs boson of any kind[17].

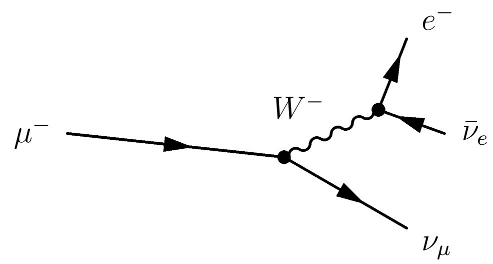

Figure 2.3.: Decay of a muon via emitting a charged W^- boson.

Table 2.3.: The three fundamental forces of the Standard Model and the bosons carrying them[5]. The mass of the gluon is a theoretical prediction. A value of a few MeV cannot be precluded.

Force	Particles		Range / m	Mass / GeV	Spin
electromagnetism	γ	photon	∞	$< 10^{-27}$	1
strong force	G	gluon	10^{-15}	0	1
weak force	$W^{\pm}$	W boson	10^{-18}	80.399 ± 0.023	1
	Z	Z boson	10^{-18}	91.188 ± 0.002	1

2.2. Physical Observables and Feynman Diagrams

One of the most important points of a physical theory is its capability to predict observables. In particle physics, those observables are for example the mean life time τ of an instable particle or the cross section σ for a given process. Both depend on the probability that one (or several) distinct interactions occur. To acquire the cross section one has to consider the transition of an initial state $|i\rangle = |p_1^i, p_2^i\rangle$ into a different final state $|f\rangle = |p_1^f \cdots p_m^f\rangle$. These two quantum states are connected by the *transition amplitude* M:

$$M_{fi} = \langle f|M|i\rangle, \tag{2.14}$$

where M_{fi} is called the matrix element of that distinct process. In canonical quantum field theory, M is derived in the interaction picture in a perturbation series in the powers of the interaction Lagrangian. In Wick's theorem, each expansion of this series can be represented by a *Feynman diagram*. Diagrams with the same (or similar) final states as the process in question also contribute to the observables and have to be taken into account. Figure 2.4 shows an example of the production and decay of a Z boson with higher order corrections.

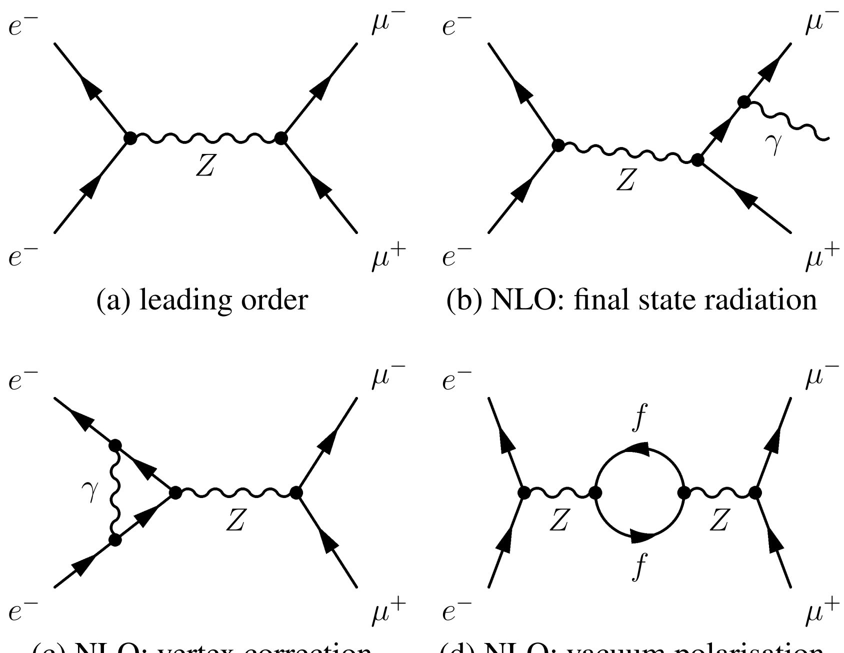

(a) leading order (b) NLO: final state radiation

(c) NLO: vertex correction (d) NLO: vacuum polarisation

Figure 2.4.: Production and decay of the Z boson with higher order corrections (NLO = next to leading order)

The cross section then is:

$$\sigma = \frac{S(2\pi)^4}{4\sqrt{(p_1^i p_2^i)^2 - (m_1^i m_2^i)^2}} \int \left\{ |M_{fi}|^2 \cdot \delta^4 \left(p_1^i + p_2^i - \sum_{k=1}^{m} p_k^f \right) \cdot \prod_{k=1}^{m} \frac{d^3 p_k^f}{2(2\pi)^3 E_k^f} \right\}. \quad (2.15)$$

The statistical factor S has to be included to avoid double-counting of identical final states. Conservation of energy and momentum is secured by the four-dimensional delta distribution $\delta^4(\cdots)$.

Another interesting figure is the *instantaneous luminosity* $\mathcal{L}$ which in scattering theory and accelerator physics is the number of particles at the collision point per unit area and unit time. It is usually expressed in units of $\mathrm{cm}^{-2}\mathrm{s}^{-1}$ or $\mathrm{b}^{-1}\mathrm{s}^{-1}$, where one *barn* is defined as: $1\ \mathrm{b} = 10^{-24}\ \mathrm{cm}^2$. For a ring collider experiment like the LHC, the luminosity can be calculated with:

$$\mathcal{L} = nf \frac{N_1 N_2}{A}, \quad (2.16)$$

where

n is the number of particle bunches in each ring,
f is the circulation frequency,
N_i are the number of particles in the respective bunches and
A is the cross section of the beam.

With the luminosity $\mathcal{L}$ provided by the collider parameters and the cross section σ for a given process, the expected number of events would be:

$$N = \alpha\varepsilon\sigma \int \mathcal{L}\, dt, \quad (2.17)$$

where α denotes the detector acceptance, incorporating for example non-complete coverage of the full solid angle of the detector and ε is the particle identification efficiency, incorporating trigger and reconstruction efficiencies. The determination of the reconstruction efficiency of muons is the subject of this thesis.

3. LHC and the ATLAS Experiment

This thesis uses data taken by the ATLAS experiment at the Large Hadron Collider at CERN. Both machines are described in the following two sections.

3.1. Large Hadron Collider

The Large Hadron Collider (LHC) is a particle accelerator designed to collide opposing beams of protons at a center of mass energy of $14\ \mathrm{TeV}$ with an instantaneous luminosity of $10^{34}\ \mathrm{cm}^2\mathrm{s}^{-1}$[18]. This synchrotron is build 50–$175\ \mathrm{m}$ under ground by the European Organization of Nuclear Research (CERN[(1)]) in the $26.6\ \mathrm{km}$ long tunnel of its predecessor, the Large Electron Positron Collider (LEP), near Geneva, Switzerland. Before injected into the LHC, the protons are pre-accelerated in several stages (see figure 3.1):
First the LINAC2, a linear accelerator, brings the protons to an energy of $50\ \mathrm{MeV}$ and feeds the Proton Synchrotron Booster (PSB), where they are accelerated to $1.4\ \mathrm{GeV}$. From there, the protons are injected into the Proton Synchrotron (PS) and Super Proton Synchrotron (SPS), where their energy is increased to $26\ \mathrm{GeV}$ and $450\ \mathrm{GeV}$, respectively. Finally injected into the LHC the protons get ramped up to their operating energy of $7\ \mathrm{TeV}$[(2)].
For one month a year the LHC is operated in heavy ion mode colliding lead nuclei at an energy of $574\ \mathrm{TeV}$ per nucleus. The first stages of the lead acceleration are LINAC3 feeding the Low Energy Ion Ring (LEIR) for beam cooling rather than LINAC2 feeding PSB.
The LHC consists of 9593 superconducting magnets shaping the proton beam. A total of 1232 dipole magnets bend the protons around the LHC ring. The dipole field strength reaches a maximum of $8.33\ \mathrm{T}$ when the proton energy peaks at $7\ \mathrm{TeV}$. Additional 392 quadrupoles focus the beam to a cross section as low as possible. The whole construction is cooled down by superfluid Helium to a temperature of $1.9\ \mathrm{K}$ ($-271.25\ °\mathrm{C}$) to render the niobium-titanium (NbTi) cables of the main dipoles superconductive. Through the dipoles flows a current of $11\,850\ \mathrm{A}$ to sustain the high magnetic fields which are required to bend $7\ \mathrm{TeV}$ protons around the cir-

[1] Conseil Européen pour la Recherche Nucléaire
[2] By the end of this work, the LHC is operating at half its design energy: $3.5\ \mathrm{TeV}$ per proton. After a major shut down for upgrade installations in late 2012, the energy will be increased to said $7\ \mathrm{TeV}$ per proton.

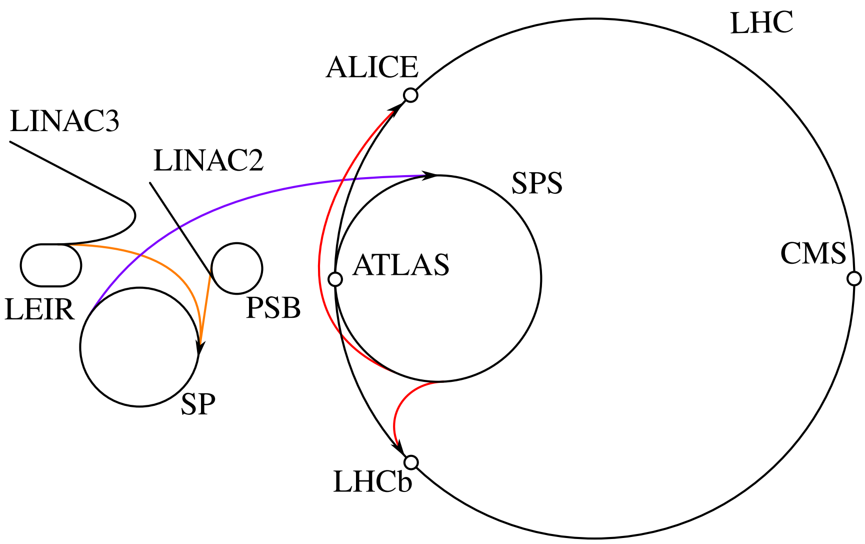

Figure 3.1.: Schematics of the LHC accelerator, its experiments and pre-accelerators (not to scale).

cular path. The protons are arranged into bunches and travel with nearly the speed of light ($\mathrm{c} = 299\,792\,458\ \mathrm{m/s}$), making 11 245 circulations a second. This leads to a bunch collision rate of up to $40\ \mathrm{MHz}$ at two of the four interaction points. At these two points, the general purpose detectors A Toroidal LHC Apparatus[19] (ATLAS) and Compact Muon Solenoid[20] (CMS) are located. The other two interaction points are occupied by the more specialized detectors A Large Ion Collider Experiment[21] (ALICE) and LHCb[22] (the 'b' refers to the bottom quark physics it is designed to investigate).

3.2. ATLAS Detector

ATLAS[19] is a multi-purpose particle detector which covers almost the whole solid angle with its onion-like structure. The cylindrical construction is about $22\ \mathrm{m}$ in diameter, $42\ \mathrm{m}$ long and weights 7000 metric tons. A sketch of the detector is given in figure 3.2. Due to the high luminosity of the LHC and the great number of particles arising in the collisions, fast and radiation-hard detector components and read-out electronics with a high resolution in space and time are required. The detector itself can be divided into three sub-detectors:

- **Inner Detector (ID):** precise reconstruction of tracks and vertices, momentum measurement of charged particles
- **Calorimeter (Cal):** identification and energy measurement of jets (hadrons), electrons and photons with high resolution (in space as well as in energy)
- **Muon Spectrometer (MS):** identification and momentum measurement of muons

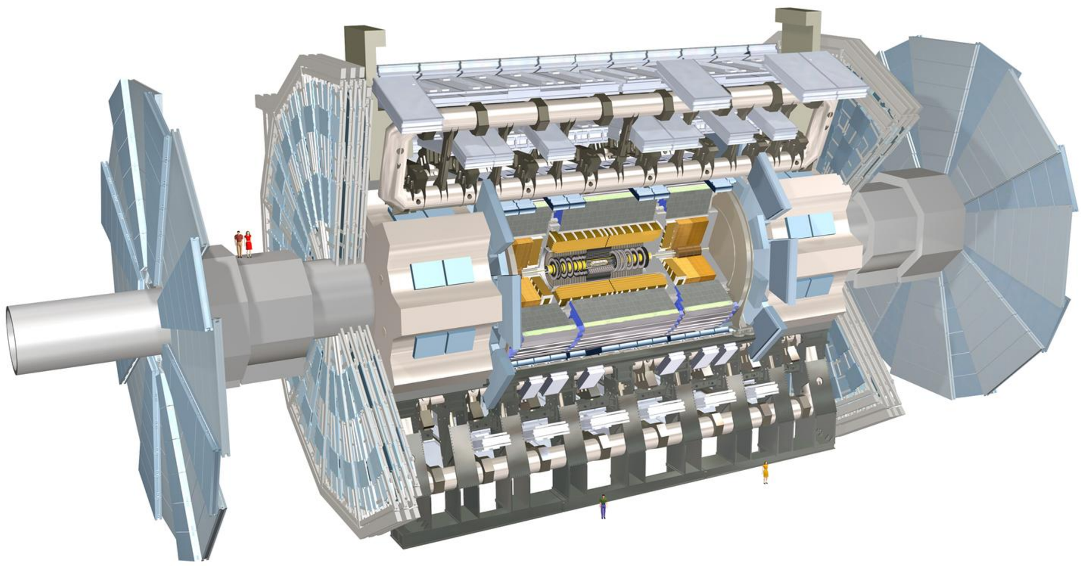

Figure 3.2.: The ATLAS detector at the LHC[23].

Each sub-detector consists again of three parts: A cylindrical barrel and two circular end-caps closing it on both sides.

3.2.1. ATLAS Coordinate System and Parametrization

The origin of the Cartesian coordinate system is set at the nominal interaction point at the center of the detector. The y-axis points upwards and the x-axis to the center of the LHC ring. The z-axis points into beam direction in a way that x, y and z form a right-handed orthogonal basis. The polar angle $\vartheta = 0 \cdots \pi$ is measured from the z-axis and the azimuthal angle $\phi = -\pi \cdots \pi$ from the x-axis positive upwards. Because of the solenoidal magnetic field parallel to the beam axis (see section 3.2.5), only the part of the particle's momentum transverse to the beam axis can be measured in the inner detector. For this reason, the transverse momentum p_{T} is widely used:

$$p_{\mathrm{T}}^2 = p_{\mathrm{x}}^2 + p_{\mathrm{y}}^2. \tag{3.1}$$

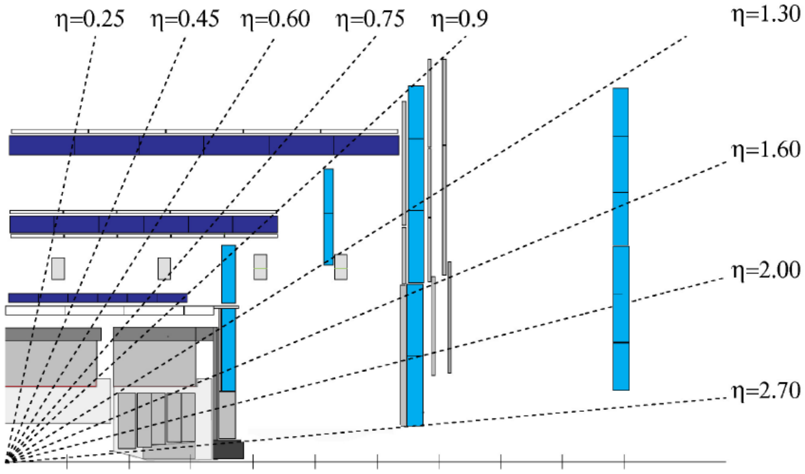

Figure 3.3.: An illustration of the values of the pseudo-rapidity η according to different directions from the coordinate system's origin (lower left corner). The polar angle ϑ would be measured from the horizontal axis, positive upwards. The dark and light blue boxes are the muon spectrometer's barrel and end-cap modules, respectively (see section 3.2.4 for the muon spectrometer). Picture from [24]

A very common coordinate at particle collider is the *rapidity* y:

$$y = \frac{1}{2} \ln \left(\frac{E - p_z}{E + p_z} \right) , \tag{3.2}$$

which has the great advantage that it is invariant under Lorentz-boosts along the beam axis. Most QCD cross sections tend to be flat with respect to rapidity and therefore the number of partons (quarks and gluons) is constant in each rapidity interval of fixed width. In the high relativistic limit, the rapidity can be simplified to the *pseudo-rapidity* η:

$$\eta = \frac{1}{2} \ln \left(\frac{|p| - p_z}{|p| + p_z} \right) = - \ln \left(\tan \frac{\vartheta}{2} \right) . \tag{3.3}$$

An illustration of the η-values for different directions from the origin of the coordinate system is given in figure 3.3.
Additional parameters to fully describe the track of a charged particle are the transverse impact parameter d_0, which is the distance of the track's point of closest approach to the beam axis in the transverse plane, and z_0, the longitudinal distance of this particular point. The spatial separation of two particle tracks is expressed in terms of $\Delta R = \sqrt{(\Delta\phi)^2 + (\Delta\eta)^2}$. In contrast to ΔR, $R = \sqrt{x^2 + y^2}$ is the radial distance from the beam axis.

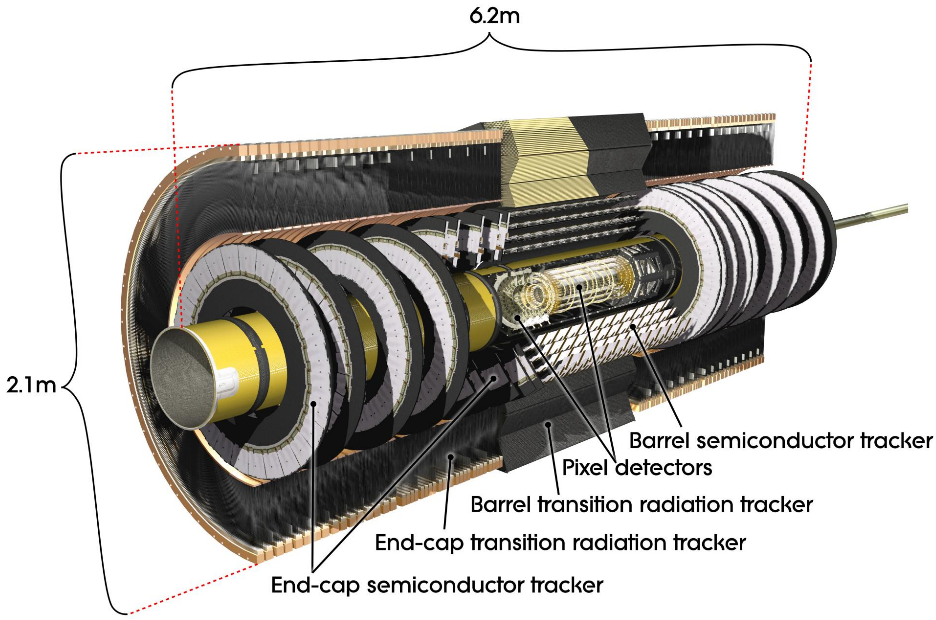

Figure 3.4.: Cutaway view of the ATLAS inner detector[23].

3.2.2. Inner Detector

The inner detector (ID) is contained within a $2\ \mathrm{T}$ solenoidal magnetic field (see section 3.2.5) and provides primary and secondary vertex reconstruction and high momentum resolution for charged tracks with a transverse momentum higher than $0.5\ \mathrm{GeV}$ in a pseudo-rapidity range of $|\eta| < 2.5$. Over a range of $|\eta| < 2.0$ and transverse momenta between $0.5\ \mathrm{GeV}$ and $150\ \mathrm{GeV}$, it also provides reliable electron identification. It has a length of $6.2\ \mathrm{m}$, a diameter of $2.1\ \mathrm{m}$ and consists of (from inner to outer) the silicon pixel detector, the silicon cathode tubes (SCT) and and multiple gaseous straw tubes in the transition radiation tracker (TRT). A picture of the inner detector is shown in figure 3.4.

Silicon Pixels

The pixel detector is the innermost tracking system in the ATLAS detector. It consists of three barrel layers and five end-cap disks with a total of 1744 identical silicon sensors and an intrinsic resolution of $10\ \mu\mathrm{m}$ in R–ϕ and $115\ \mu\mathrm{m}$ in z (barrel) and R (end-caps). The innermost layer is build at a radius of $51\ \mathrm{mm}$. The highest granularity is realized around the vertex region. Initially, the sensors will operate at a bias voltage of $150\ \mathrm{V}$ which will rise to $600\ \mathrm{V}$ after ten years of operation to maintain charge collection efficiency. Charged particles traversing the sensors will ionize the material and produce electron-hole-pairs. The produced electrons drift to the readout due to the applied voltage where they are collected by bump bonds.

Silicon Cathode Tubes

The SCT incorporates four double-layers of silicon sensors, with the first part of each layer aligned parallel to the beam pipe and the second tilted by a stereo angle of $40\ \mathrm{mrad}$. In contrast to the pixel detector, the SCT sensors are segmented into micro-strips. The 15 912 SCT sensors have an intrinsic resolution of $17\ \mu\mathrm{m}$ in R–ϕ and $580\ \mu\mathrm{m}$ in z and R.

Transition Radiation Tracker

The TRT straw tubes are $40\ \mathrm{mm}$ in diameter, $144\ \mathrm{cm}$ (barrel) or $37\ \mathrm{cm}$ (end-cap) long and filled with a mixture of 70% Xe, 27% CO_2 and 3% O_2 with an over-pressure of 5–$10\ \mathrm{mbar}$. The anodes are gold plated tungsten wires, $31\ \mu\mathrm{m}$ in diameter. The intrinsic resolution of the TRT sensors lays at $130\ \mu\mathrm{m}$. In the barrel, the TRT contains up to 73 layers of straws (up to 160 in the end-cap) leading to an average of 36 hits per track and providing a continuous tracking over a wide range of energies.

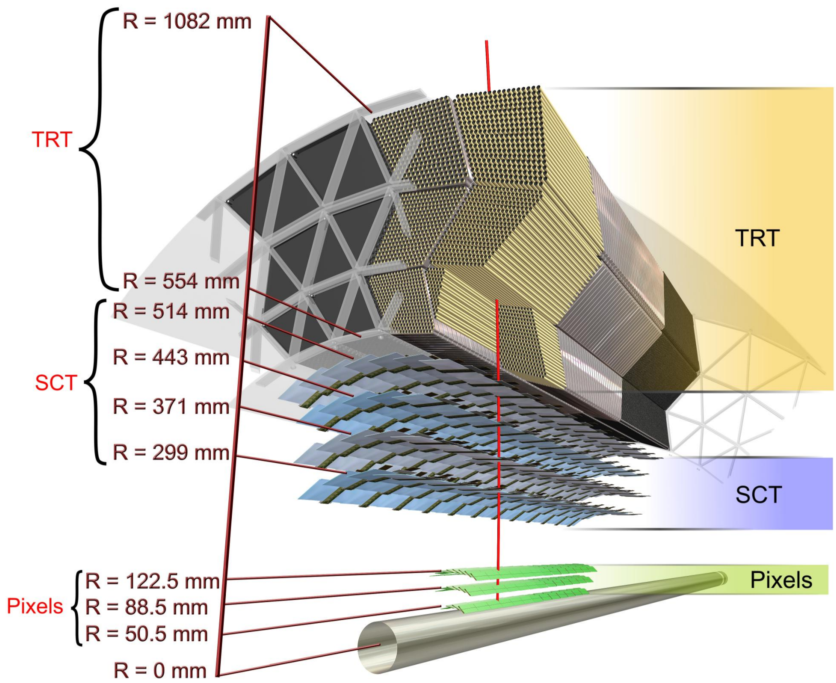

Figure 3.5.: Labeled layers of the inner detector traversed by a $p_{\mathrm{T}} = 10$ GeV particle[23].

The combination of the precise pixel and SCT trackers at small radii with the TRT at a larger radius gives high precision both in R–ϕ and z coordinate as well as robust pattern recognition. The labeled components of the inner detector with a high energy particle crossing them are shown in figure 3.5.

3.2.3. Electromagnetic and Hadronic Calorimeters

The calorimeters are designed to measure the energy of any electromagnetically or strongly interacting objects and cover a range of $|\eta| < 4.9$, where the electromagnetic calorimeter provides good conditions for electron and photon measurement with its high granularity over the range of the inner detector. The coarser granularity of the hadronic calorimeter is still sufficient for jet reconstruction and missing energy measurements. To provide full ϕ coverage without any azimuthal cracks, the electromagnetic calorimeter uses an accordion geometry, folding layers of liquid argon (LAr) sensors with lead absorbers around the beam axis. The hadronic calorimeter uses scintillator tiles as active material and steel absorbers to shower any hadronic objects. The calorimetry system is designed to stop any particles except muons and neutrinos. A schematic view of the calorimeters is shown in figure 3.6.

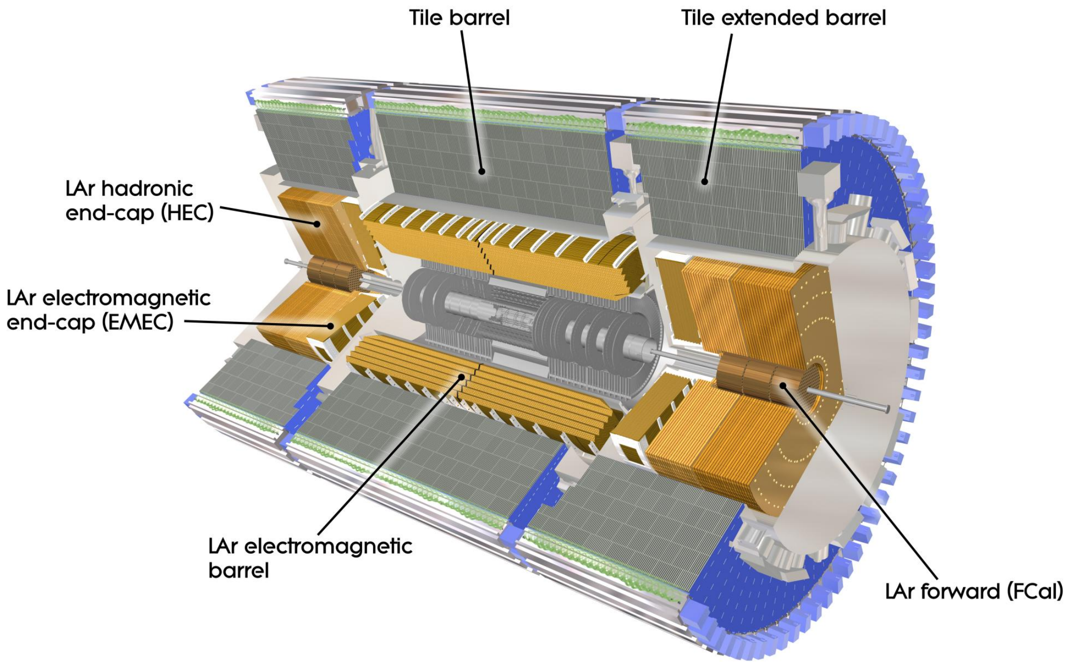

Figure 3.6.: Sketch of the ATLAS calorimeter system[23]. The inner detector at the center is shaded in gray.

To study the energy resolution of the calorimeter systems, electron, positron and pion test beams of energies between 1 and 250 GeV were used[19]. The results were fitted according to the following formula:

$$\frac{\sigma(E)}{E} = \frac{a}{\sqrt{E/\mathrm{GeV}}} \oplus b, \tag{3.4}$$

where a is the stochastic and b the constant term. For the electromagnetic barrel and end-cap calorimeters, values of $a = 10.1\%$ and $b = 0.17\%$ have been determined. The energy resolution performance of the hadronic end-cap is particle dependent. The fit-values for a were found to be $(21.4\pm0.1)\%$ for electrons and $(80\cdots85)\%$ for pions. The values for b are compatible with zero within errors. Tests on the hadronic barrel part yield $a = (56.4 \pm 0.4)\%$ and $b = (5.5 \pm 0.1)\%$ (all numbers for a and b from [19]).

3.2.4. Muon Spectrometer

The tracks in the muon system are measured by three cylindrical layers in the barrel and three circular wheels in the end-cap as shown in figure 3.7. The three barrel-layers are arranged at radii of $5\ \mathrm{m}$, $7.5\ \mathrm{m}$ and $10\ \mathrm{m}$ with a longitudinal extent in each direction of about $6\ \mathrm{m}$, $10\ \mathrm{m}$ and $13\ \mathrm{m}$, respectively. In the end-cap, muon chambers are located at distances of $|z| \approx 7.4\ \mathrm{m}$, $10.8\ \mathrm{m}$, $14\ \mathrm{m}$ and $21.5\ \mathrm{m}$. To maintain service access to the calorimeter, the solenoid and the inner detector, a small gap in the $|\eta| \approx 0$ region has been left open. Additional gaps in the acceptance are in the feet region due to the supporting structure and in the transition region, where barrel and end-cap parts overlap. The angular range as seen from the interaction point, wherein a straight track would not hit any muon spectrometer sensors and therefore would not be recorded due to the service gaps, is about $|\vartheta| \leq 2.3°$ ($|\eta| \leq 0.04$) to $|\vartheta| \leq 4.8°$ ($|\eta| \leq 0.08$), depending on the azimuth of the track. Implemented into the muon system is the toroidal magnet system, which is explained in more detail in the next section.
The muon spectrometer incorporates several sub-systems: The monitored drift tubes (MDT), cathode strip chambers (CSC), resistive plate chambers (RPC) and the thin gap chambers (TGC) whose main parameters are summarized in table 3.1.

Monitored Drift Tubes

The MDTs cover a range of $|\eta| < 2.7$. In the range of $2.0 < |\eta| < 2.7$ the innermost barrel layer of drift tubes has been replaced by cathode strip chambers because the MDTs limit on the counting rate of $150\ \mathrm{Hz/cm^2}$ would not be sufficient for safe operation in the high particle fluxes in high η-regions. The MDT chambers consist of three to eight layers of drift tubes which are filled with a mixture of 93% Ar and 7% CO_2 at a pressure of $3\ \mathrm{bar}$. In the barrel as well as in

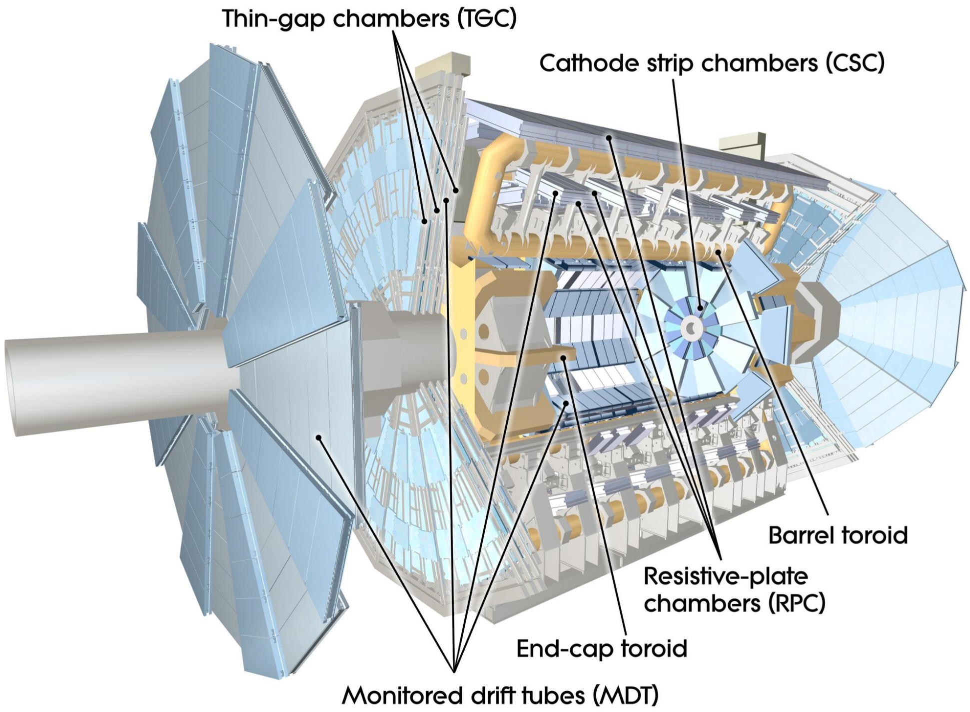

Figure 3.7.: The ATLAS muon spectrometer[23]. Inner detector and calorimetry were removed from this view (compare figure 3.2).

Table 3.1.: Main parameters for the muon spectrometer sub-detectors and their function. The number of chambers in parenthesis refer to the final configuration in 2009—numbers without parenthesis to the original design.

Monitored Drift Tubes	**MDT**
• coverage	$\|\eta\| < 2.7$ (innermost layer $\|\eta\| < 2.0$)
• number of chambers	1088 (1150)
• function	precision tracking
Cathode Strip Chambers	**CSC**
• coverage	$2.0 < \|\eta\| < 2.7$
• number of chambers	32
• function	precision tracking
Resistive Plate Chambers	**RPC**
• coverage	$\|\eta\| < 1.5$
• number of chambers	544 (606)
• function	triggering, second coordinate
Thin Gap Chambers	**TGC**
• coverage	$1.05 < \|\eta\| < 2.7$ (2.4 for triggering)
• number of chambers	3588
• function	triggering, second coordinate

the end-caps, the tubes are arranged tangentially to circles around the beam pipe. A single tube provides a spatial resolution of about $80\ \mu\mathrm{m}$, a chamber up to $35\ \mu\mathrm{m}$ perpendicular to the wire direction.

Cathode Stripe Chambers

Both CSC wheels consist of eight small and eight large chambers, each containing four planes of sensors. They are located in the high η-regions ($2.0 < |\eta| < 2.7$) of the muon systems innermost end-cap wheel where particle fluxes exceed the rates of safe MDT operation. CSC operation is considered safe for counting rates of up to $1000\ \mathrm{Hz/cm^2}$. The CSCs are multi-wire proportional chambers filled with $80\%\ \mathrm{Ar}$ and $20\%\ \mathrm{CO_2}$. The CSC cathodes are segmented into strips perpendicular to each other providing two-coordinate measurements with a spatial resolution of $60\ \mu\mathrm{m}$ per chamber.

Resistive Plate Chambers

The RPC system in the barrel consists of three layers around the beam axis. In each chamber two parallel, resistive electrode-plates made of phenolic-melaminic plastic are kept at a distance of $2\ \mathrm{mm}$. The gap between the two plates is filled with a gas mixture of $C_2H_2F_4$ (94.7%), iso-C_4H_{10} (5%) and SF_6 (0.3%). The electrical field in this gas has a strength of $4.9\ \mathrm{kV/mm}$ and the signal is read out via capacitive coupling to two orthogonal sets of metallic strips on the outer side of the plates. The ionized charges, produced by traversing charged particles, drift to the strips where each set provides one coordinate for the track reconstruction. The gas volume has no segmentation in ϕ-direction and thus covers the chamber over its whole length of $3.2\ \mathrm{m}$. An RPC unit consists of two such gaseous chambers, each $13\ \mathrm{mm}$ high and separated by light-weight paper honeycomb. The whole unit has a height of about $10\ \mathrm{cm}$. In the outer and middle layers of the barrel muon system, MDTs are combined with one (outer) or two (middle) layers of RPC units to so-called stations and super-stations, respectively.

Thin Gap Chambers

TGCs are multiwire proportional chambers where the wire-to-cathode distance of $1.4\ \mathrm{mm}$ is shorter than the wire-to-wire distance of $1.8\ \mathrm{mm}$ (see figure 3.9). The chambers are $2.8\ \mathrm{mm}$ high with wires $50\ \mu\mathrm{m}$ thick. The gap is filled with a mixture of CO_2 and n-C_5H_{12}. The TGCs are located on two concentric, non-overlapping rings in a rapidity range of $1.5 < |\eta| < 1.92$ for the outer and $1.92 < |\eta| < 2.4$ for the inner disk.

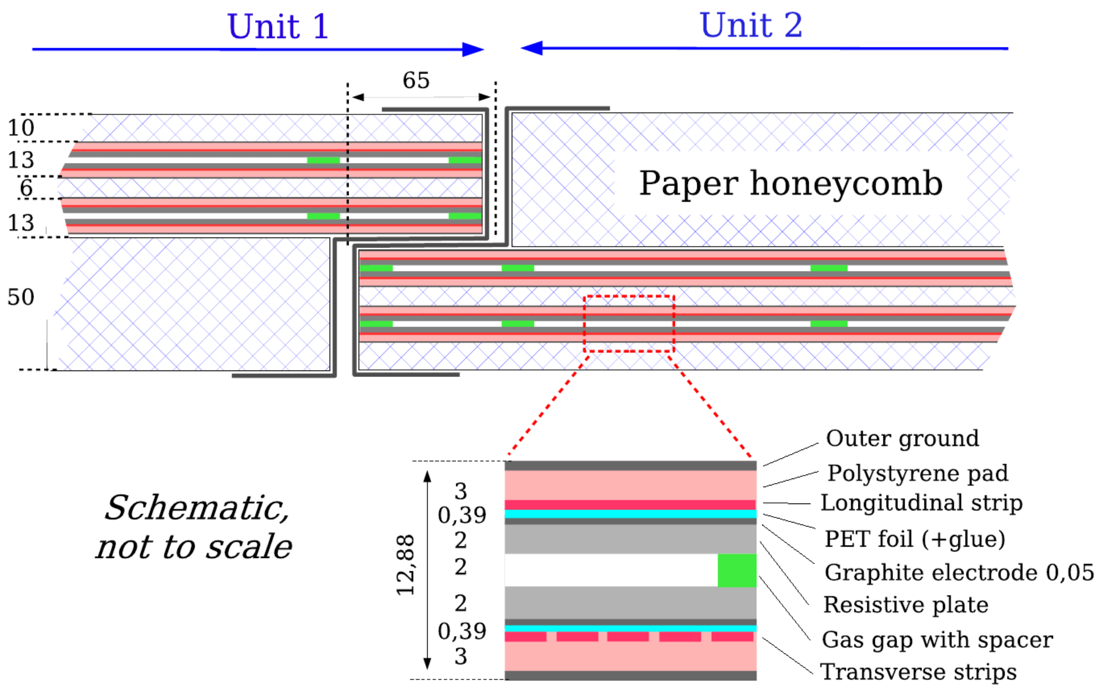

Figure 3.8.: Cross section through an RPC, where two units are combined to form a chamber. Each unit consists of two gas volumes (white) surrounded by two resistive plates (gray). The plates are held apart by spacers (green). Readout is performed by longitudinal and transversal strips (solid and dashed, red line, respectively), each measuring one coordinate. Dimensions are given in mm. [19]

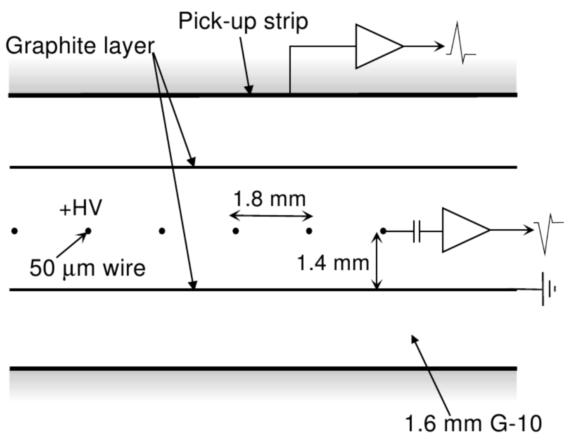

Figure 3.9.: Sketch of the TGC structure width anode wires, graphite cathodes and pick-up strips orthogonal to the wires. [19]

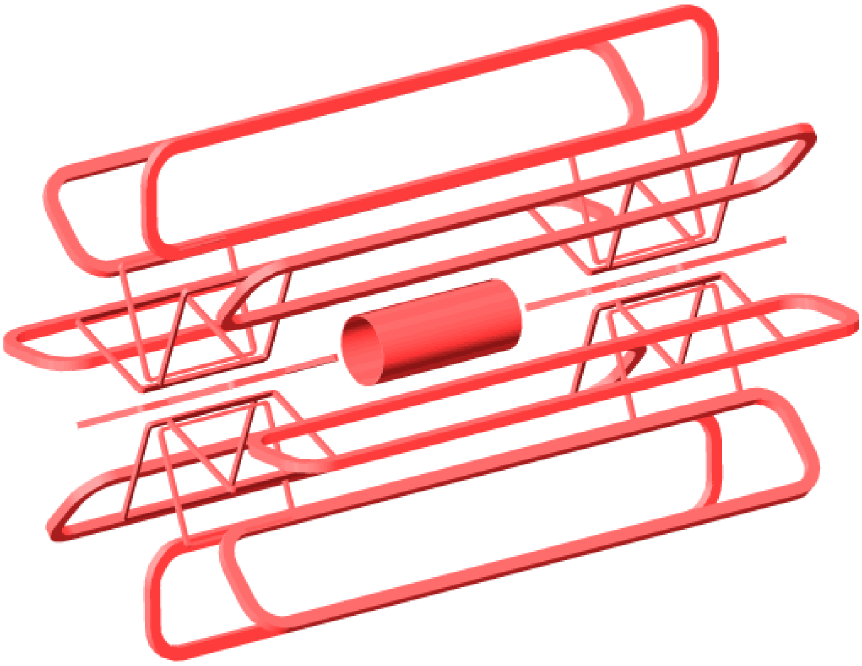

Figure 3.10.: ATLAS magnet system with the inner solenoid (middle cylinder) and the barrel and end-cap toroid coils (large and small loops, respectively).

3.2.5. Magnet System

ATLAS houses a unique, hybrid system of superconducting magnets which stores a total energy of 1.6 GJ. The whole system consists of the barrel and two end-cap toroids and the inner solenoid (see figure 3.10). Each toroid has 8 large, air cooled coils. The whole magnet system generates a magnetic field over a volume of $12\,000\ \mathrm{m}^3$ (defined as the region in which the field exceeds the value of $50\ \mathrm{mT}$).

Central Solenoid

The solenoid provides an axial and homogeneous $2\ \mathrm{T}$ field for the inner detector at a nominal operational current of $7.73\ \mathrm{kA}$. It is $5.8\ \mathrm{m}$ long and has an outer diameter of $2.56\ \mathrm{m}$ with a mass of $5.4\ \mathrm{t}$. To keep the material thickness in front of the calorimeter as low as possible the solenoid is $10\ \mathrm{cm}$ thick and shares a vacuum vessel with the LAr calorimeter, eliminating the need of two vacuum walls.

Barrel and End-Cap Toroids

The toroid magnets—integrated into the muon spectrometer—generate a toroidal field of a strength between $0.5\ \mathrm{T}$ and $1\ \mathrm{T}$. The barrel system is $20.1\ \mathrm{m}$ in diameter, $25.3\ \mathrm{m}$ long and weighs $830\ \mathrm{t}$. The end-cap toroids are each $10.7\ \mathrm{m}$ high, $5\ \mathrm{m}$ long with a weight of $239\ \mathrm{t}$.

3.2.6. Trigger System and Data Acquisition

Event Selection

ATLAS uses a three level trigger system subsequently reducing the amount of data that needs to be processed. The Level-1 trigger (L1) searches for the detector signatures of high-p_{T} muons, electrons, photons, jets and τ-leptons as well as large missing transverse energy ($E_{\mathrm{T}}^{\mathrm{miss}}$) and large total transverse energy ($\sum(E_{\mathrm{T}})$). It uses reduced-granularity information from the RPCs, TGCs and the calorimeter sub-systems to decide whether to keep the event or not within $2.5\ \mu\mathrm{s}$, reducing the event rate from $40\ \mathrm{MHz}$ to 75–$200\ \mathrm{kHz}$. Seeded by the L1, the Level-2 trigger (L2) uses Regions-of-Interest (RoI) around the L1-triggered objects. Within these RoIs, the L2 has access to higher granularity information to further decrease the event rate to below $3.5\ \mathrm{kHz}$ with an average processing time of $40\ \mathrm{ms}$ per event. The Event Filter (EF) uses fully reconstructed events to further reduce the event rate to below $200\ \mathrm{Hz}$ within an average event processing time of $4\ \mathrm{s}$.
L2 and EF are referred to as the High Level Trigger (HLT) and make use of the whole detector information, including the inner detector for track reconstruction, as well as the full granularity of the detector sub-systems. The algorithms for both the L2 and EF run on dedicated computing farms at the experiment.

Data Formats

There are various data streams according to the objects of interest to which an event can be assigned (e.g. muons, electron/photon, jet/$E_{\mathrm{T}}^{\mathrm{miss}}$). After an event passed all the trigger levels, the EF writes it into one or more of those data streams, making it accessible for physics analysis. The detector information is stored in Raw Data Object-format (RDO) with a size of $1.3\ \mathrm{MB}$/event. Event physics object reconstruction algorithms use the RDOs as input and convert them into Event Summary Data (ESD) reducing the the size per event to approximately $500\ \mathrm{kB}$. Using ESDs as input, Analysis Object Data (AOD) is derived which is already suited for common physics analysis. Its average event size is $100\ \mathrm{kB}$. Another very common data format are ROOT[25] files or n-tuples where the variables are saved in a flat branch/leaf hierarchy and the event size is reduced to the order of $10\ \mathrm{kB}$, depending on the number of variables included. The analysis of this thesis was done on such ROOT files.

3.3. Pile-Up

The inelastic cross section of proton-proton-interactions at the LHC is approximately $70\ \mathrm{mb}$ which leads to an average of 23 interactions per recorded event at the design luminosity of $10^{34}\ \mathrm{cm}^2\mathrm{s}^{-1}$, varying according to a Poisson distribution[26]. Each event is therefore a superposition of multiple collisions. This circumstance is referred to as *in-time pile-up*. Tracks from those additional collisions are not related to the event which triggered the readout and account as a considerable background.
The so-called *out-of-time pile-up* occurs because the signal from the calorimeter cells is integrated over a time window larger than the time spread between two proton collisions. Therefore a recorded event is also sensitive to events before and after itself.

Jet Vertex Fraction

There are several methods that allow to distinguish between physical objects from main and pile-up vertices. By assigning inner detector tracks to different vertices one can introduce a discriminating variable, the *Jet Vertex Fraction (JVF)*, which measures the probability that a jet originated from a particular vertex. The $JVF(i,j)$ is the fraction of transverse momenta of the tracks within a jet i that originated from the vertex j as sketched in figure 3.11. Jet selection based on this discriminant proved to be insensitive to the contributions from simultaneous, uncorrelated soft collisions that occur during pile-up and shows good performance in a wide range of instantaneous luminosities.

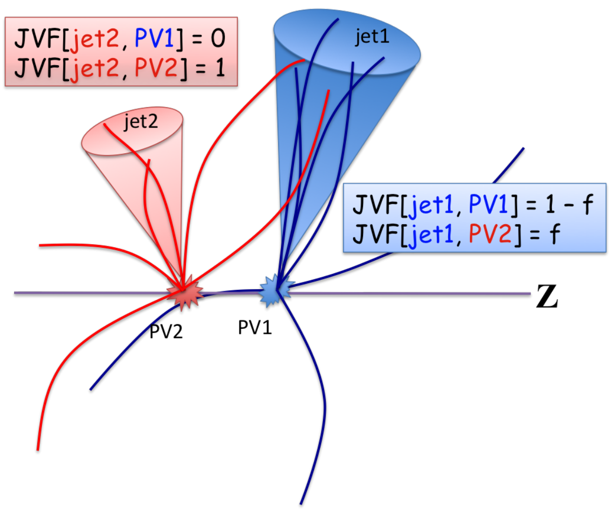

Figure 3.11.: Schematic explanation of the jet vertex fraction. Jet1 consists to a fraction of tracks originating from the vertex PV2. The momentum fraction of the tracks according the whole jet momentum is f. Considering PV1 as the main primary vertex, a cut of $JVF(\text{jet2, PV1}) > 0$ would omit jet2 as a pile-up jet.

4. Muon and Jet Identification

4.1. Muon Identification

The ATLAS detector has been designed for efficient muon identification and momentum resolutions as low as 3% for transverse momenta of $p_{\mathrm{T}} = 200\,\mathrm{GeV}$ and less then 10% up to $p_{\mathrm{T}} = 1\ \mathrm{TeV}$[19]. This is achieved by a combination of measurements from the inner detector and the muon spectrometer as shown in the following section. How muons are associated to decays of Z bosons is presented in section 4.1.2.

4.1.1. Muon Types

At ATLAS, four types of muons are defined to achieve high purity, efficiency and momentum resolution: combined, stand-alone, segment tagged and calorimeter tagged muons.

Combined Muons (CB): Muon spectrometer and inner detector perform an independent track reconstruction. After successful combination, a joint track is formed (see figure 4.1(a)). Combined muons are the standard muon objects for physics analysis and provide candidates of highest purity.

Segment Tagged Muons (ST): If the hits in the muon spectrometer are not sufficient for a proper measurement, an inner detector track is still considered a muon, if the extrapolated track can be associated with a reconstructed muon segment (see figure 4.1(b)). Segment tagged muons are used to recover low detector efficiencies in low-p_{T} and badly covered η regions.

Stand-Alone Muons (SA): Only the hits in the muon spectrometer are used to reconstruct the track. Its parameters are extrapolated through the calorimeters and the inner detector, energy losses taken into account, back to the beam axis (see figure 4.1(c)). In this thesis, stand-alone muons are used for the determination of the calorimeter tagged muon and inner detector efficiencies.

Calorimeter Tagged Muons (CT) A trajectory in the inner detector is identified as a muon if the associated energy depositions in the calorimeters are compatible with the hypothesis of a minimum ionizing particle.

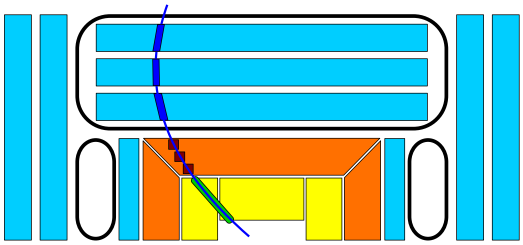

(a) **combined muon:** A track in the muon spectrometer (blue), extrapolated through the calorimeter (orange) and matched with a track in the inner detector (yellow)

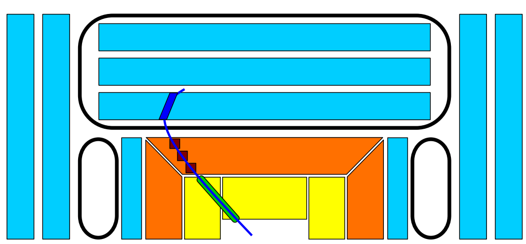

(b) **segment tagged muon:** An inner detector track (yellow) matched with one hit segment in the muon spectrometer (blue)

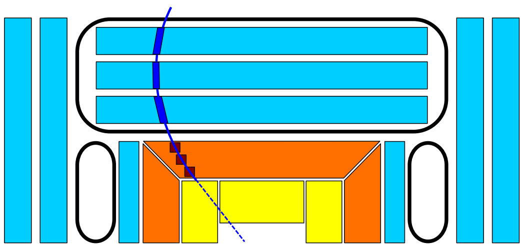

(c) **stand-alone muon:** A track in the muon spectrometer (blue), extrapolated through the calorimeter (orange) but without a matching inner detector track (dashed line)

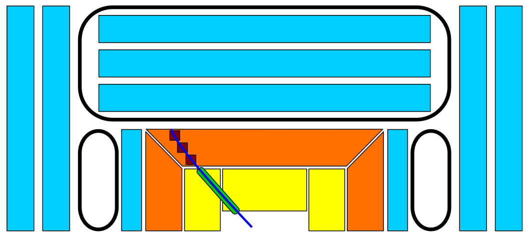

(d) **calorimeter tagged muon:** An inner detector track (yellow) extrapolated into the calorimeter (orange) and compatible with the signature of a minimum ionizing particle

Figure 4.1.: The four types of muon candidates defined at ATLAS: combined (a), segment tagged (b), stand-alone (c) and calorimeter tagged (d).

Furthermore, there are two distinct algorithm families capable of reconstructing three of these four muon types: MuID[27, 28] and Staco[27, 29]. Calorimeter tagged muons are reconstructed by separate algorithms[30]. The main difference between these two families comes with the combined muon algorithm: Whilst MuID does a complete refit of the track through all inner detector and muon spectrometer hits, Staco combines the ID and MS tracks with a weighted average. The inner detector measurement dominates the combination up to $p_{\mathrm{T}} = 80\ \mathrm{GeV}$ in the barrel and $p_{\mathrm{T}} = 20\ \mathrm{GeV}$ in the end-caps. For transverse momenta up to $100\ \mathrm{GeV}$ the inner detector and muon spectrometer measurements have similar weights while the muon spectrometer dominates at $p_{\mathrm{T}} \gtrsim 100\ \mathrm{GeV}$. After the Staco combined algorithm found a muon candidate, its track segments in the muon spectrometer are ignored by the following Staco segment tagged algorithm. This is not the case in the MuID family, where the overlap between combined and segment tagged muons has to be taken into account.

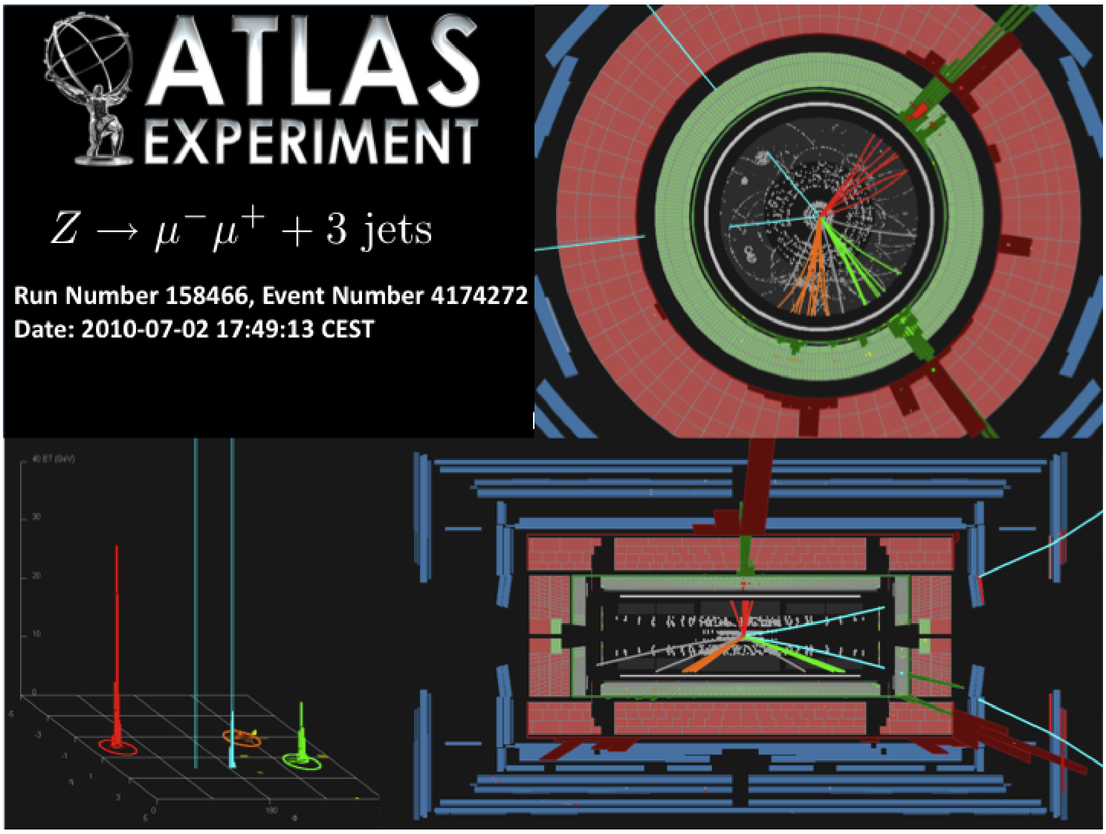

Figure 4.2.: A candidate of a Z decay into a muon pair accompanied by three jets. The two muons (blue tracks) have a transverse momentum of 96 GeV and 68 GeV and their invariant mass is 79 GeV. Due to the Z boson's transverse momentum of 144 GeV, the angular seperation of the muons is significantly smaller then 180° which would be expected in the Z's rest frame. The three jets (red, yellow and orange tracks) have transverse energies of 168, 105, and 45 GeV, respectively[23].

4.1.2. Muon Properties in $Z \rightarrow \mu\mu$ Events

Muons arising from Z decays ($m_Z = (91.1876 \pm 0.0021)$ GeV[5]) have a distinct signature: Because Z bosons are electrical neutral and electrical charge is conserved, the muons are oppositely charged. In the Z boson's rest frame, they carry the whole boson's energy in their momentum in opposite directions due to momentum conservation. In the case of a non resting Z, the stereo angle between the muons decreases. In any case, the invariant mass $m_{\text{inv}} = \sqrt{(P_1 + P_2)^2}$, where P_i are the muons's four-momenta, is at the Z's rest mass. Furthermore, the muons are expected to be isolated, meaning that no additional high energetic particles were reconstructed in a given ΔR around the muon. If there were additional jets produced in the hard scattering process (see figures 4.2 and 4.3) the muons would still be isolated, because of the conservation of momentum, the jets would boost the Z away from themselves.

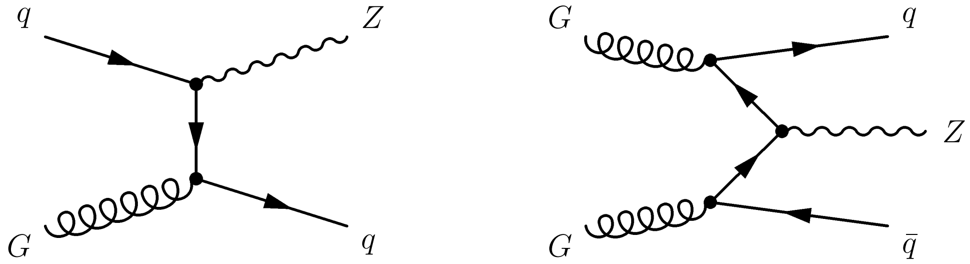

(a) Compton scattering-like Z production

(b) Gluon fusion into $Z + 2q$

Figure 4.3.: Production of a Z boson in association of one (a) or two (b) hard scattered quarks, where each will most likely cascade into a jet. The quarks again can radiate a gluon producing further jets.

4.1.3. Backgrounds

There are other processes besides Z decays which can produce muons. W bosons (with $m_W = 80.399 \pm 0.023$ GeV[5]) decay into high-p_T muons, too. But unlike Z bosons, a W produces only one muon accompanied by a neutrino. Neutrinos hardly interact at all and therefore induce a large imbalance in the meassured energy in the R–ϕ plane making the W's detector signature very distinguishable from a Z decay into two high momentum muons. Though a W^+W^- event could produce two oppositely charged muons, their momenta are not correlated in a way that their invariant mass would be found significantly often near the Z mass.

Furthermore, muons can originate from leptonic decays of heavy quarks in jets and hadrons, especially mesons containing b and/or c quarks. These mesons are all too light to produce high-p_T muon pairs, even though the J/Ψ ($c\bar{c}$, $m_{J/\Psi} = 3096.916 \pm 0.011$ MeV[5]) and the Υ-meson ($b\bar{b}$, $m_\Upsilon = 9460.30 \pm 0.26$ MeV[5]) produce detector signatures very similar to the Z's.

Light mesons like $\pi^\pm$ or $K^\pm$ have also muonic decay channels with high branching ratios (with $m_{\pi^\pm} = 139.57$ MeV and $m_{K^\pm} = 493.677 \pm 0.016$ MeV)[5]. Due to their long life time, π and K mesons tend to decay off of the primary vertex or even in the calorimeters. Such *decay-in-flight muons* can be avoided by selecting combined muons whose tracks originate close to the primary vertex. If such mesons were to be found in jets, the muons produced in their decays would not be isolated and therefore omitted.

If in a $t\bar{t}$-pair, the W bosons emitted by both quarks decay leptonically, they can produce two muons with high momenta. As this is essentially the W^+W^- process mentioned before, the two muon momenta would not be correlated.

Even though the ATLAS detector is located about 100 m under ground, it is still sensitive to muons arising from collisions of cosmic particles in the upper atmosphere. Due to the high energy of the cosmic particles, these muons can have a considerable momentum. Additionally, they will be reconstructed as an oppositely charged pair, because the different direction of the

magnetic field in the upper and lower part of the muon spectrometer causes a change in the muon's track's curvature. The reconstruction algorithms only consider the interior of the detector as the track's origin and therefor reconstruct two objects with different charge. The tracks of those *cosmic muons* are distributed uniformly over the whole x-z-plane and can be reduced by cuts on the distance from the track to the primary vertex.
Another source of background events comes from *fake muons*, i.e. particles or detector signals that were falsely identified as muons. Due to the stringent requirements on the combined muon's track, fake rates are of the order of 10^{-2} per η interval and event, depending on the track's p_{T} threshold, as shown in Monte Carlo studies (see figure 4.4)[27].

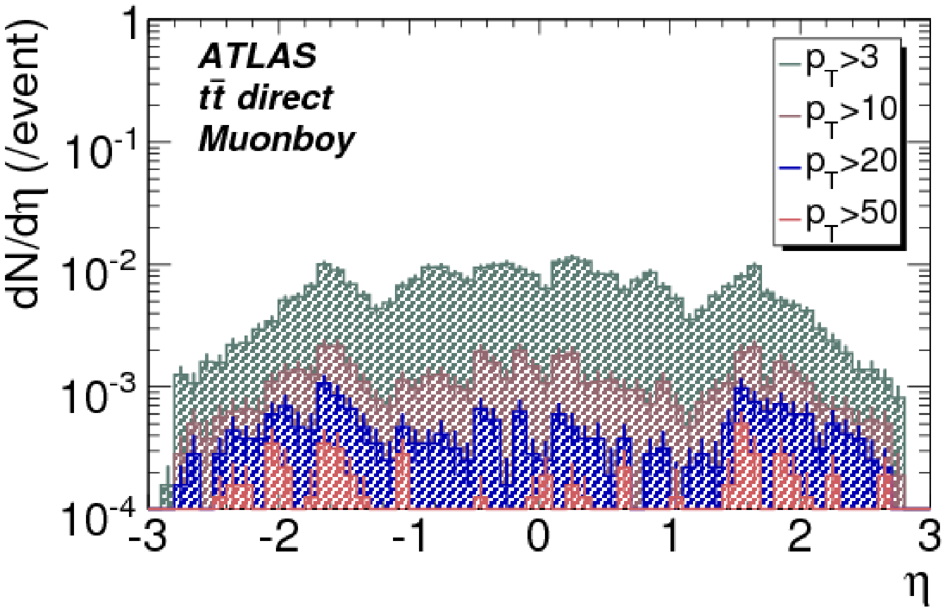

Figure 4.4.: Muon fake rates as a function of η in dependence of different p_{T} thresholds. "Muonboy" is the name of the Staco stand-alone muon reconstruction algorithm. Picture from [27]

4.2. Jet Reconstruction

Jets are bundles of particles. They can be produced in QCD processes and play a major role at hadron collider—being either a tool to measure cross sections of the strong interaction, for the determination of the parton distribution functions of the proton or as a background source. Due to the non-perturbative nature of the hadronization, it is difficult to assign soft-radiated particles unambiguously to one parton emitted at leading order processes. There are several algorithms using different methods on defining when a bundle of tracks actually has to be separated into two jets. The algorithm used in this thesis is the anti-k_T algorithm[31].
The anti-k_T algorithm introduces a distance $d_{i,j}$ between two 4-vectors i and j and a distance $d_{i,B}$ between the 4-vector i and the beam line:

$$d_{i,j} = \min(k_{\mathrm{T}\,i}^{-2}, k_{\mathrm{T}\,j}^{-2}) \frac{\Delta_{i,j}^2}{R^2}, \tag{4.1}$$

$$d_{i,B} = k_{\mathrm{T}\,i}^{-2}, \tag{4.2}$$

where

$k_{\mathrm{T}\,i}$ is the transverse momentum of the 4-vector i—giving the algorithm its name,[1]
$\Delta_{i,j}^2 = (y_1 - y_2)^2 + (\phi_1 - \phi_2)^2$, with y_i and ϕ_i the rapidity and azimuth, respectively and
R the jet's radius parameter.

The algorithm clusters tracks to jets by looking for the smallest distance $d_{i,j}$ and combining i and j to one entity. If $d_{i,B}$ is smaller than any $d_{i,j}$, the cluster i is called a jet and removed from further searches. This procedure is repeated until no track is left.
The consequence of this approach is, that the shape of a hard jet is exclusively determined by the containing high-p_T track and soft tracks are simply collected around the hard one, resulting in a conical jet of radius R. If another hard particle 2 is present with $R < \Delta_{1,2} < 2R$ to a jet 1, it is not possible to form two perfectly conical jets. In this case, jet 1 will be conical and jet 2 misses the part overlapping with jet 1 ($p_{\mathrm{T}\,1} \gg p_{\mathrm{T}\,2}$) or the overlapping part will be divided by a straight line ($p_{\mathrm{T}\,1} = p_{\mathrm{T}\,2}$) or by a path depending on both jet's momenta ($p_{\mathrm{T}\,1} \approx p_{\mathrm{T}\,2}$). Figure 4.5 shows the behavior of the anti-k_T algorithm on a randomly generated event in comparison with three alternative algorithms: k_T[32], Cambridge/Aachen[33, 34] and SISCone[35].
The advantage of the anti-k_T algorithm compared to the alternative ones is its infrared and collinear safety.

[1] For the sole purpose of pointing out the origin of the algorithms name, the original nomenclature has been adapted. In the following, p_T is used for the transverse momentum again.

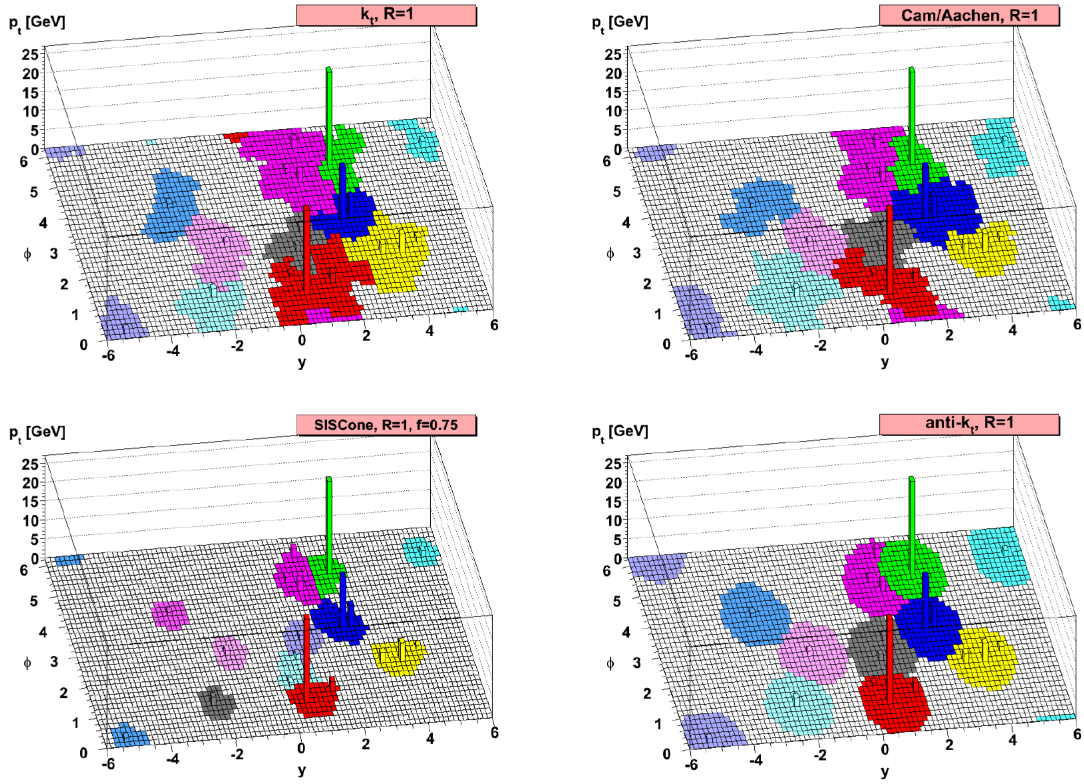

Figure 4.5.: Comparison of the jet cluster definition of four different algorithms: k_T (upper left), Cambridge/Aachen (upper right), SISCone (lower left) and anti-k_T (lower right). Here, the anti-k_T algorithm produces the "roundest" jet clusters, especially around the high-p_T objects (red, green and dark blue). Picture from [31]

5. Muon Reconstruction Efficiency

The reconstruction efficiency for combined muons is the product of three independent sub-efficiencies:

$$\varepsilon_{\mathrm{reco}} = \varepsilon_{\mathrm{ID}} \times \varepsilon_{\mathrm{MS}} \times \varepsilon_{\mathrm{match}}, \tag{5.1}$$

where

$\varepsilon_{\mathrm{ID}}$ is the efficiency that the inner tracking system reconstructs a track from the muon,
$\varepsilon_{\mathrm{MS}}$ is the efficiency of the muon spectrometer reconstructing a track from the muon and
$\varepsilon_{\mathrm{match}}$ is the efficiency of combining the two tracks to a combined one.

To determine these efficiencies, a so called *Tag & Probe* method is used, which is explained in more detail in the following section.

5.1. The Tag & Probe Method

Efficiency measurements with the tag and probe method utilize any known correlation between two separately reconstructed objects, e.g. the tracks from the decay of a known, instable particle. With stringent selection criteria on the tag object's side and the correlation to the probe, one can ensure the identity of the probe object without direct, hard cuts on this object.

In this analysis, the well known decay of the Z boson is used.
In the first step a combined muon candidate is selected, using measurements and hit information from the whole detector and tight selection criteria. This is called the *Tag Muon*.
Then, a *Probe Muon* is selected depending on the desired sub-efficiency. For the inner detector efficiency ($\varepsilon_{\mathrm{ID}}$), the probe would be a stand-alone muon candidate reconstructed only by the muon spectrometer. The muon spectrometer and matching efficiencies ($\varepsilon_{\mathrm{MS}} \times \varepsilon_{\mathrm{match}}$) can be measured together using inner detector tracks as probes.
The tag and probe muons are consecutively combined and further pair criteria are applied. They have to be of opposite charge, originate from the same vertex and their invariant mass has to be at the nominal Z boson mass.

In the final step, it is checked if the probe muon can be associated with a matching object, which is again depending on the sub-efficiency: The inner detector efficiency is the fraction of stand-alone muon candidates that can be associated with an inner detector track:

$$\varepsilon_{\text{ID}} = \frac{\text{\# of SA muons matching ID track}}{\text{\# of SA muons}}. \tag{5.2}$$

The matching and muon spectrometer efficiency is the fraction of inner detector probe muons matching a baseline muon (see below):

$$\varepsilon_{\text{MS}} \times \varepsilon_{\text{match}} = \frac{\text{\# of ID probes matching baseline muons}}{\text{\# of ID probes}}. \tag{5.3}$$

The calorimeter tagged muon efficiency is the fraction of stand-alone muon candidates matching calorimeter tagged muon candidates:

$$\varepsilon_{\text{Calo}} = \frac{\text{\# of SA muons matching calo muons}}{\text{\# of SA muons}}. \tag{5.4}$$

The matching between the inner detector probes and the baseline muons is considered successful if the spacial separation between the probe muon and the matching object is $\Delta R < 0.01$. For a successful matching of a stand-alone probe muon to an inner detector track/calorimeter tagged muon, ΔR has to be smaller than 0.05. The ΔR distribution between the inner detector probes and the baseline muons as well as between stand-alone probes and inner detector tracks can be seen in figure 5.1

The tag and probe selection criteria are summarized in table 5.2. The selection criteria for muon analysis objects, incorporating combined and segment tagged muons, are summarized in table 5.1. In the following, this class of muon candidates will be referred to as *baseline muons*. In this thesis, the reconstruction efficiency of these baseline muons and, additionally, of calorimeter tagged muons will be determined.

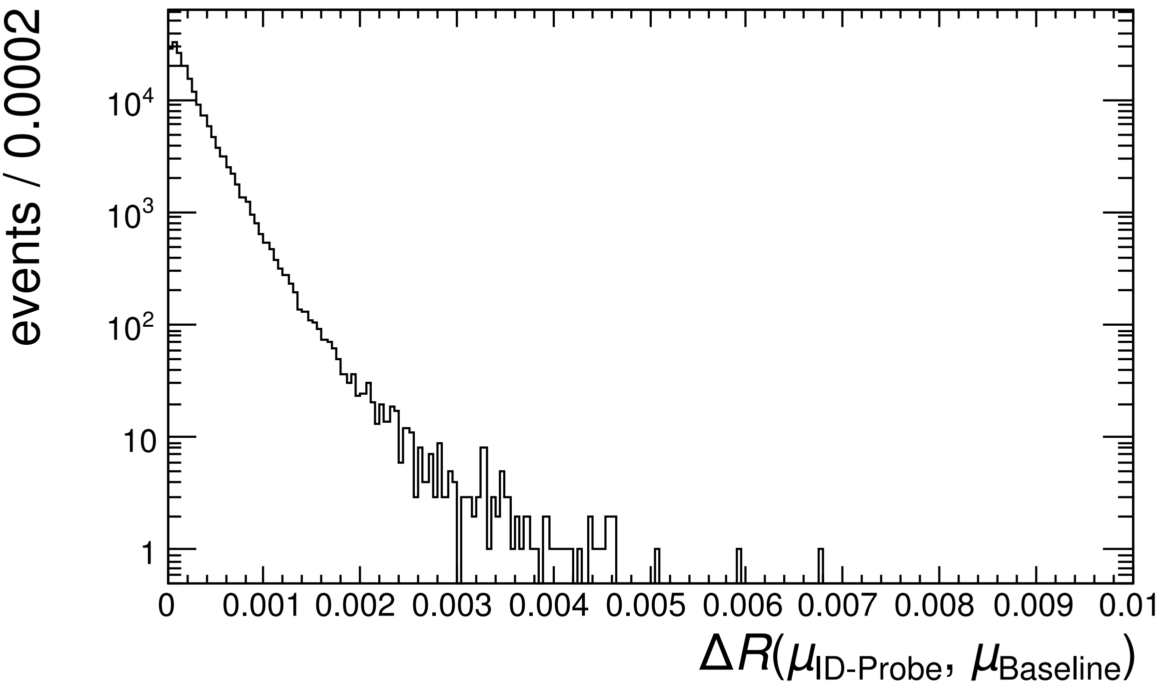

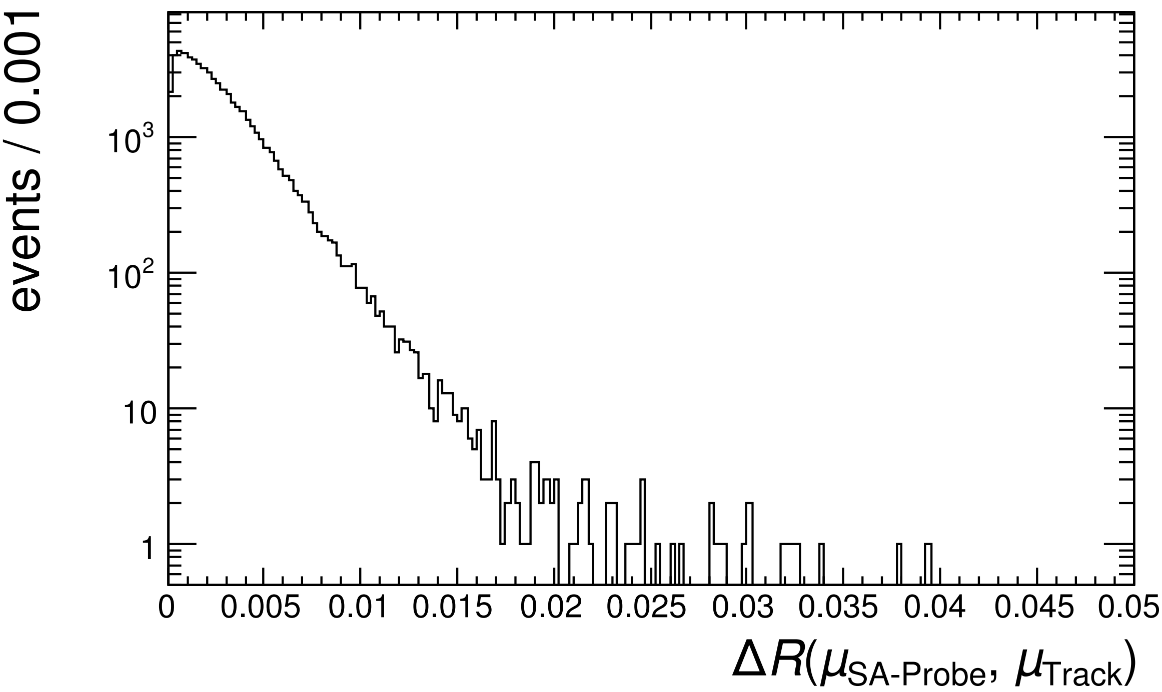

Figure 5.1.: ΔR distribution between the inner detector probes and the baseline muons (top) and between stand-alone muons and inner detector tracks (bottom) in Monte Carlo simulated signal events. The cut value for a successful match is respectively the right hand edge of the histogram.

5.2. Muon Selection

In this section, the selection criteria are summarized in tabular form and described more detailed in the following.

5.2.1. Trigger

Demanding a trigger ensures that an object of interest is indeed in an event and therefore reduces unwanted background processes. Due to the steadily increasing luminosity (see figure 5.2), the trigger menu is in permanent alteration. For this reason, a run period (labeled with capital letters in alphabetical order) dependent trigger is used. To ensure the trigger was indeed fired by a selected muon candidate, the tag muon has to be associated to the object reconstructed by the Event Filter.

5.2.2. Vertex

Due to in-time pile-up, there can be several hard scattering vertices in the event. The number of primary vertices per event in 2010 data is shown in figure 5.3. There is an average of 3.1 primary vertices per event in this data taking period.

In general, one wants a well reconstructed primary vertex (PV) which is not too far off of the nominal interaction point. The main primary vertex is defined as that vertex with the highest sum of squared transverse momenta of the tracks associated to it $(\sum p_{\mathrm{T}}^2)$[36].

The focus of this analysis is on muons from the hard scattering process, so the longitudinal and transverse distances from the primary vertex have to be as small as the resolution allows. Furthermore, cuts on the distance to the primary vertex reduces the contamination from muons arising from collisions of high energetic, cosmic particles in the upper earth's atmosphere.

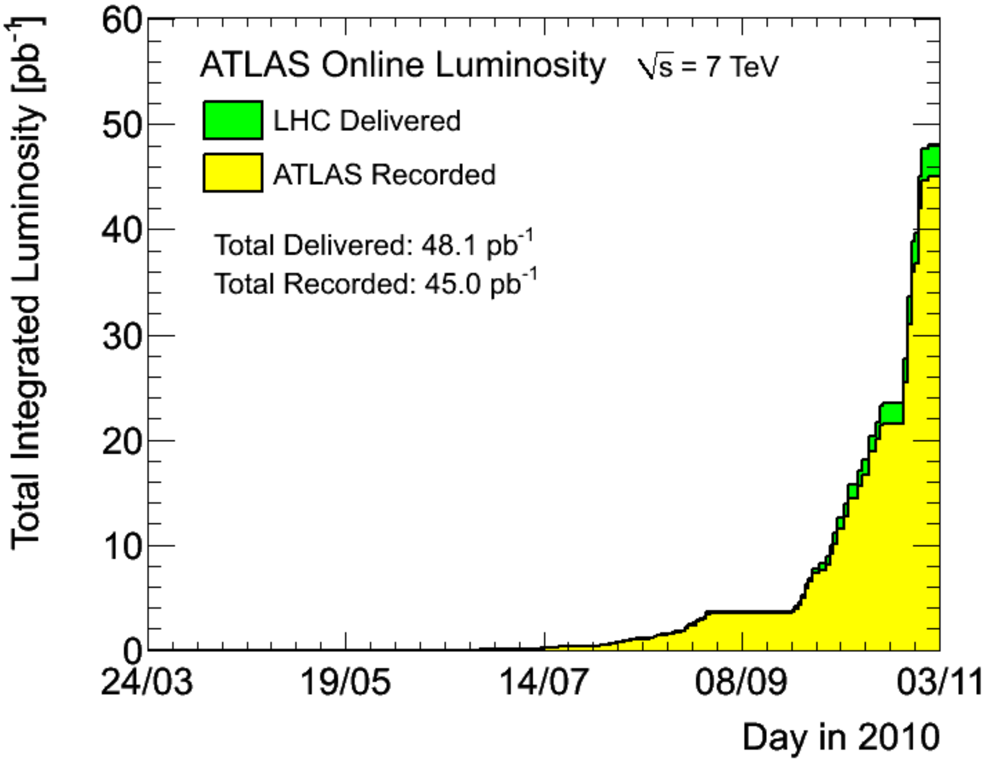

Figure 5.2.: Integrated luminosity delivered by the LHC (green) and recorded by ATLAS (yellow) in the year of 2010.

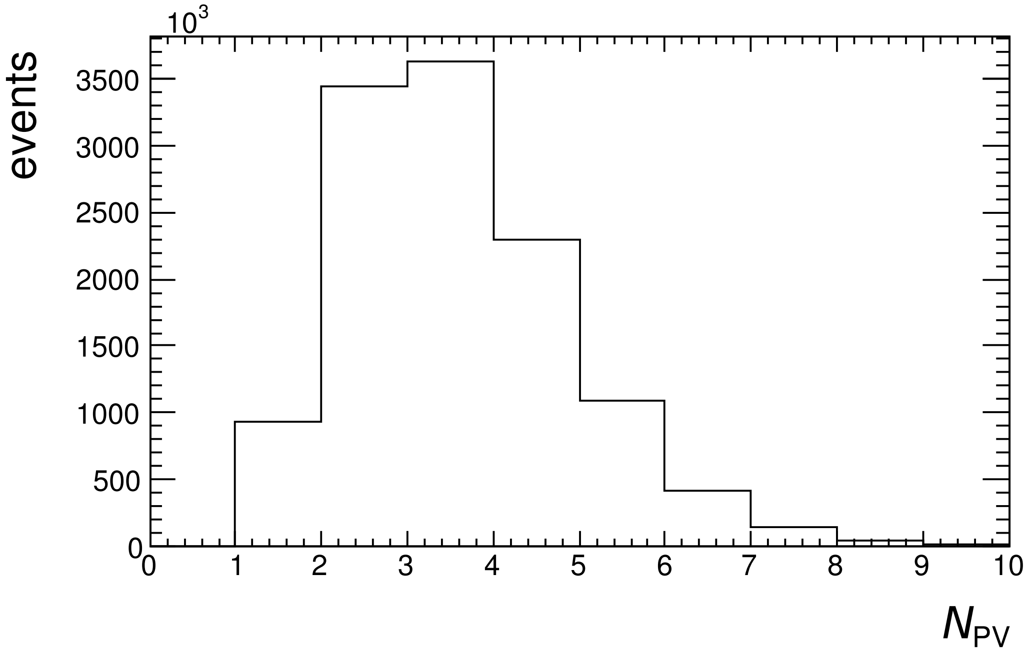

Figure 5.3.: Distribution of the number of primary vertices per event in 2010 data. mean value: 3.1 vertices per event

5.2.3. GoodRunsList

The *ATLAS data quality* group monitors the functionality of the detector and the quality of the taken data online, i.e. while data taking, as well as offline. If there were problems of any kind, the corresponding detector sub-system would get flagged accordingly. An analysis depending on the proper functionality of one or more particular parts of the detector can implement a list of run periods which were flagged "good" for these sub-systems: A *GoodRunsList* (GRL).
In this thesis, the GoodRunsList recommended by the *ATLAS Z+jets cross-section* group was used, demanding that following detector parts, important for this analysis, were working properly (a full list of required flags can be found in appendix A.1): Inner detector, all calorimeter sub-systems, muon spectrometer, muon trigger, muon reconstruction, jet reconstruction, solenoid and toroid magnetic fields.

5.2.4. Kinematics

Restraining muon candidates by a minimal transverse momentum and a maximal pseudo-rapidity defines the working phase space and suppresses background: A higher p_{T} threshold reduces the muon fake rate by 1–2 orders of magnitude (see figure 4.4), while the η requirement restricts the working space to the range of the sensors of the muon spectrometer (see figure 3.3).
The transverse momentum of all combined muon candidates in Monte Carlo simulated signal events is shown in figure 5.4.

5.2.5. Isolation

Because muons from Z decays tend to be isolated, an isolation criterion rejects background muons from unwanted processes. The $ptconeX$ criterion sums up the transverse momenta of all tracks from the primary vertex in a cone of $\Delta R = 0.X$ around the muon candidate, excluding the momentum of the muon candidate's track itself:

$$ptconeX_{\mu} = \sum_{n} p_{\mathrm{T},\,n} \qquad \text{with: } \Delta R(\mu, n) < 0.X \tag{5.5}$$

The $nuconeX$ only counts the additional tracks around the corresponding particle's track.
The summed track momenta in a cone of $\Delta R = 0.2$ divided by the candidate's track's momentum ($ptcone20/p_{\mathrm{T}}$) is shown in figure 5.5.

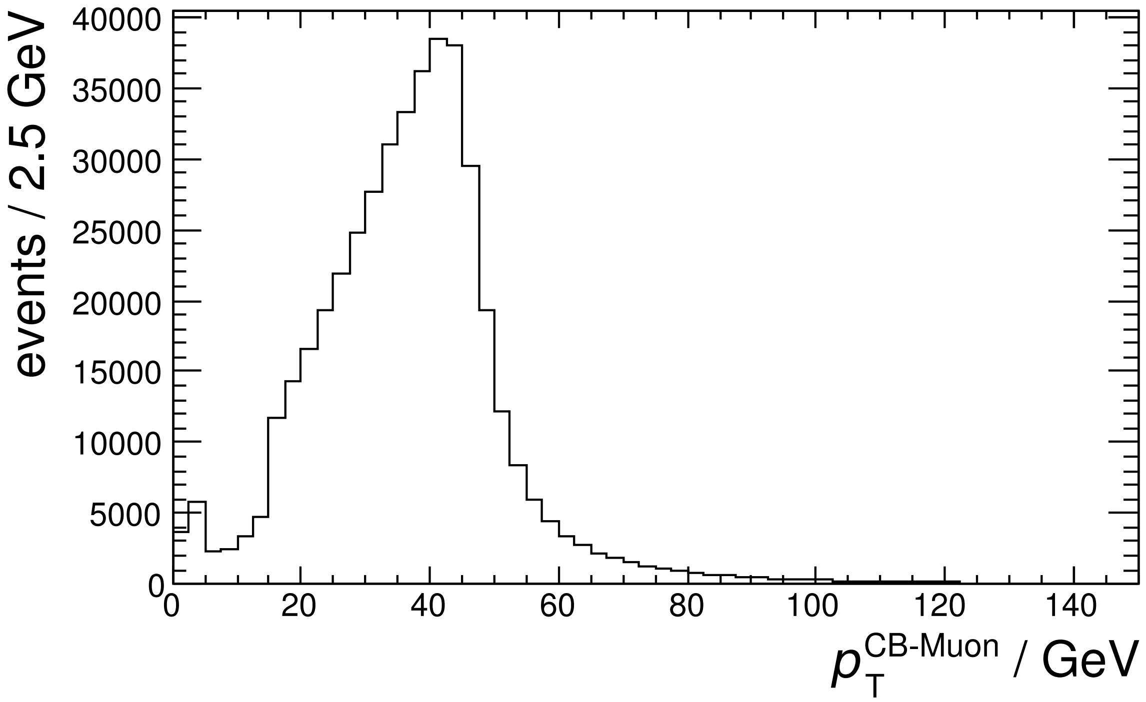

Figure 5.4.: Transverse momentum of combined muon candidates before all cuts in Monte Carlo simulated signal events before all cuts. Cut value: > 15 GeV for tag and baseline muons, > 20 GeV for probe muons

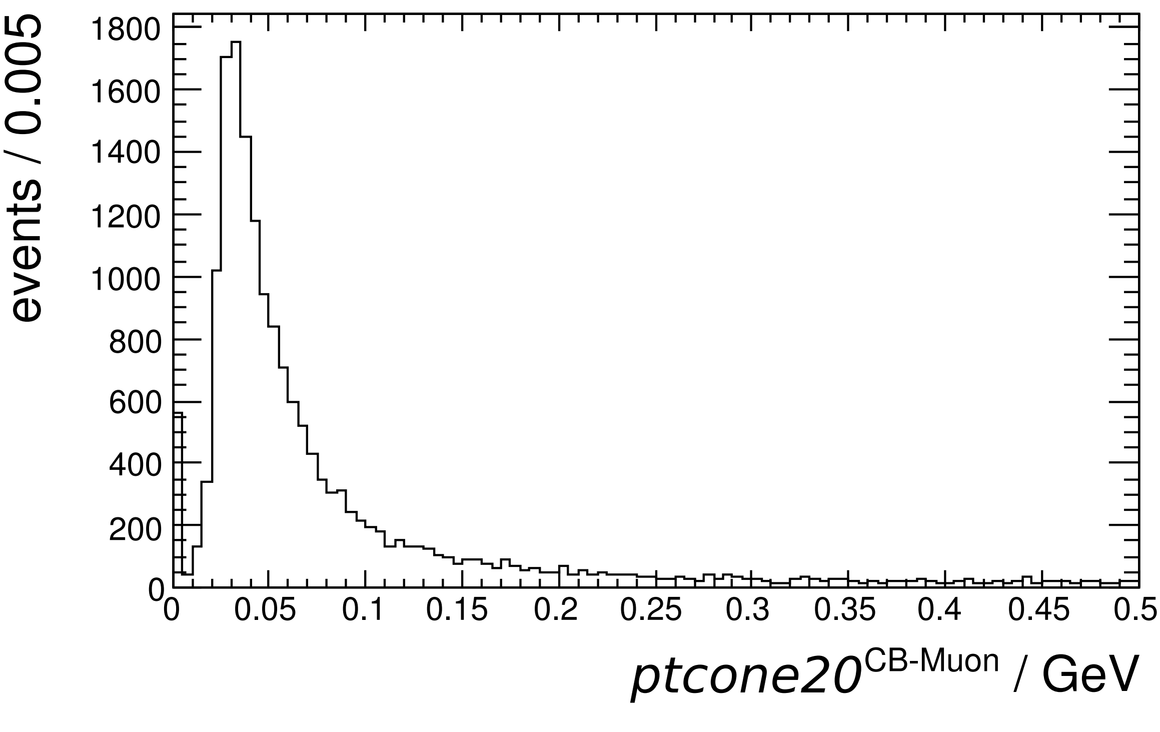

Figure 5.5.: Relative track isolation of combined muon candidates in Monte Carlo simulated signal events before all cuts. Cut value: < 0.1

5.2.6. ID Track Quality

Cuts on the number of inner detector sensors hit by a selected particle ensure a well reconstructed track with good momentum resolution. Here, TRT-Outliers are hits in the TRT straw tubes that were not crossed by a near-by track, furthermore: $n_{\mathrm{TRT}} = n_{\mathrm{TRTHits}} + n_{\mathrm{TRTOutliers}}$. Known nonfunctional pixel and SCT sensors on a track are counted as hits ("dead"-index). The B-Layer refers to the first pixel layer (see table 5.1 and 5.2).
See figure 5.6 for the η-dependent number of TRT hits produced by combined muons.

5.2.7. Pair Criteria

Muons associated to a Z boson have to be oppositely charged and originate from the same vertex. To further reduce background, an invariant mass window of ± 5 GeV around the nominal Z mass is applied. A cut on the azimuthal separation of the tag and probe (e.g. $\Delta\phi > 2$) was not applied to not reject high-p_{T} Zs (see figure 4.2, where the Z has a transverse momentum of 144 GeV). The invariant mass distribution of combined tag and inner detector probe muons is shown in figure 7.1.

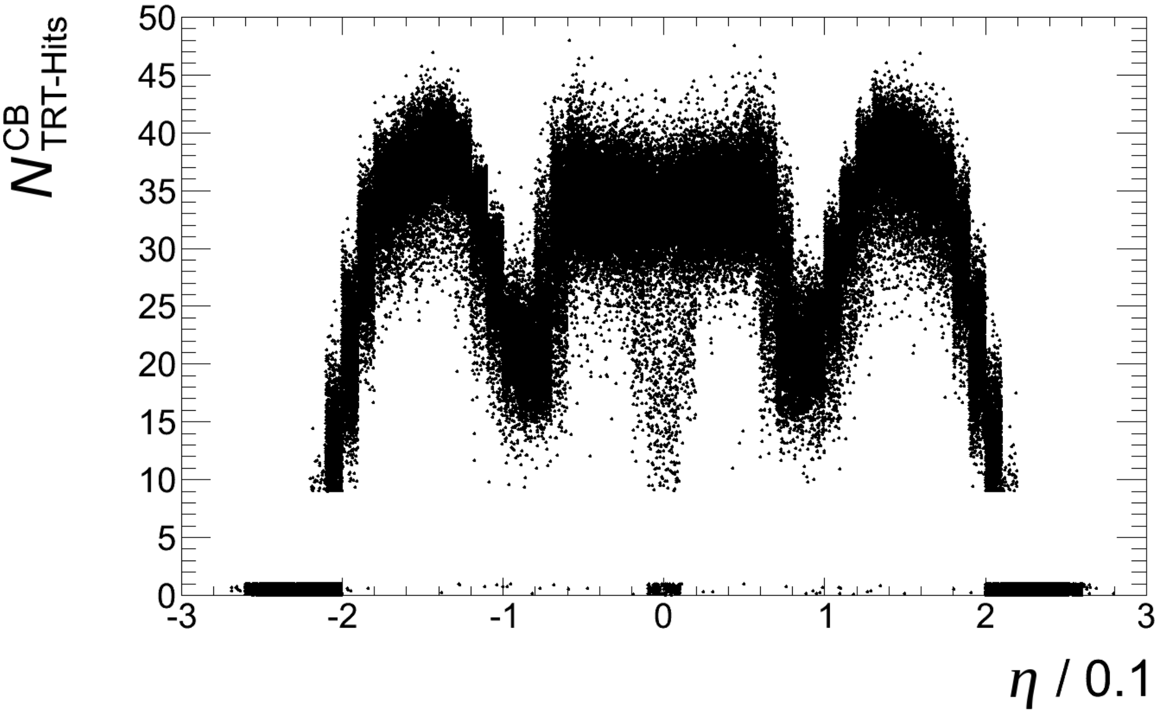

Figure 5.6.: Hits in the TRT of combined muon candidates according to their η direction in Monte Carlo simulated signal events.

Table 5.1.: Event, baseline muon, calorimeter tagged muon and jet selection criteria.

Event Selection	
Data Quality	GoodRunsList
at least 1 Primary Vertex	$z_{\text{vertex}} < 200\,\text{mm}$
with at least 3 tracks	
Trigger:	L1_MU10 (for MC)
(Data Period dependant)	EF_mu10_MG: E4-G1
	EF_mu13_MG: G2 - I1 (167576)
	EF_mu13_MG_tight: I1 (167607) - I2
Baseline Muon	
Algorithm Family	Staco
	is (combined and bestMatch) or segment tagged
Kinematics	$p_{\text{T}} > 15\,\text{GeV}$
	$\lvert\eta\rvert < 2.4$
Longitudinal Distance	$\lvert z_0\rvert < 10\,\text{mm}$ (to primary vertex)
Transversal Distance	$\lvert d_0\rvert < 0.1\,\text{mm}$ (to primary vertex)
Isolation	$ptcone20/pt < 0.1$
ID Track Quality	
TRT Hits $\lvert\eta\rvert < 1.9$	$n_{\text{TRTHits}} > 5$ and $n_{\text{TRTOutliers}} < 0.9 \cdot n_{\text{TRT}}$
TRT Hits $\lvert\eta\rvert > 1.9$	if $(n_{\text{TRTHits}} > 5)$ then $n_{\text{TRTOutliers}} < 0.9 \cdot n_{\text{TRT}}$
Pixel Hits	$n_{\text{PixHits}} + n_{\text{PixDead}} > 1$
SCT Hits	$n_{\text{SCTHits}} + n_{\text{SCTDead}} > 5$
ID Holes	$n_{\text{PixHoles}} + n_{\text{SCTHoles}} < 2$
B-Layet Hits	if expectBLayerHit then BLayerHits > 0
Calorimeter Tagged Muon	
Kinematics	$p_{\text{T}} > 15$ GeV
	$\eta < 2.4$
Jet	
Algorithm	anti-k_{T}
Radius Parameter	$R = 0.4$
Kinematics	$p_T > 30$ GeV
	$y < 4.5$
Jet Vertex Fraction	> 0.75

Table 5.2.: Tag and probe selection criteria.

Tag Muon		
Algorithm Family	Staco	
	is combined and bestMatch	
Kinematics	$p_{\mathrm{T}} > 20$ GeV	
	$\|\eta\| < 2.4$	
Longitudinal Distance	$\|z_0 \cdot \sin\vartheta\| < 0.5$ mm	(to primary vertex)
Transversal Distance	$\|d_0\| < 0.1$ mm	(to primary vertex)
Isolation	$ptcone20/p_{\mathrm{T}} < 0.1$	
	$nucone20 < 2$	
ID Track Quality		
Pixel Hits	$n_{\mathrm{PixHits}} > 0$	
SCT Hits	$n_{\mathrm{SCTHits}} > 5$	
ID Holes	$n_{\mathrm{PixHoles}} + n_{\mathrm{SCTHoles}} < 2$	
TRT Hits $\|\eta\| < 1.9$	$n_{\mathrm{TRTHits}} > 5$ and $n_{\mathrm{TRTOutliers}} < 0.9 \cdot n_{\mathrm{TRT}}$	
TRT Hits $\|\eta\| > 1.9$	if $(n_{\mathrm{TRTHits}} > 5)$ then $n_{\mathrm{TRTOutliers}} < 0.9 \cdot n_{\mathrm{TRT}}$	
Trigger Object Matching	$\Delta R(\mu_{\mathrm{tag}}, \mu_{\mathrm{EF}}) < 0.2$	

Probe Muon: ID Track		
Kinematics	$p_T > 20$ GeV	
	$\|\eta\| < 2.4$	
Longitudinal Distance	$\|z_0 \cdot \sin\vartheta\| < 0.3$ mm	(to primary vertex)
Transversal Distance	$\|d_0\| < 0.1$ mm	(to primary vertex)
Isolation	$ptcone30/p_{\mathrm{T}} < 0.5$	
Match Calo Tagged Muon	$\Delta R(\mu_{\mathrm{probe}}, \mu_{\mathrm{calo}}) < 0.1$	
ID Track Quality		
Pixel Hits	$n_{\mathrm{PixHits}} > 0$	
SCT Hits	$n_{\mathrm{SCTHits}} > 5$	
ID Holes	$n_{\mathrm{PixHoles}} + n_{\mathrm{SCTHoles}} < 2$	
TRT Hits	if $\|\eta\| < 1.9$ then $n_{\mathrm{TRTHits}} > 10$	

Probe Muon: SA Track		
Algorithm Family	Staco	
	StandAlone	
Kinematics	$p_T > 20$ GeV	
	$\|\eta\| < 2.4$	
Longitudinal Distance	$\|z_0 \cdot \sin\vartheta\| < 0.5$ mm	(to primary vertex)
Transversal Distance	$\|d_0\| < 0.1$ mm	(to primary vertex)

Pair Criteria	
	opposite charge
Longitudinal Seperation	$\Delta(z_0 \cdot \sin\vartheta) < 0.3$ mm
Transversal Seperation	$\Delta d_0 < 0.03$ mm
Invariant Mass	$m_{\mathrm{inv}} = \mathrm{m_Z} \pm 5$ GeV

6. Data Samples

The subject of this work is the data recorded by ATLAS at a center of mass energy of $7\ \mathrm{TeV}$ in the year 2010, which corresponds to an integrated luminosity of $37\ \mathrm{pb}^{-1}$. The results are compared with Monte Carlo simulations as a cross check and to provide efficiency scale factors which are the ratios of the muon reconstruction efficiencies from data and simulation (see section 7.1).

6.1. Monte Carlo Event Generation

The ATLAS collaboration also produces simulations of proton-proton collisions reenacting the experimental conditions at the interaction point as accurate as possible. For the generation of simulated collisions, Monte Carlo (MC) methods[37] are used. Here, the outcome of physical processes is not calculated but estimated by parameterizing the phase space and conducting a large number of trial experiments.

The 'event'—meaning: the outgoing particles from the collision process which enter the detector—is produced by an event generator. This task is factorized into different steps which are handled on their respective energy scale. The hard scattering process between two initial partons is derived by calculating Feynman diagrams, while parton density functions (PDF) give the probability of finding a quark or a gluon with a given momentum inside a proton. These PDFs cannot be derived from calculations but are parametrized from experimental data. After this hard process, bremsstrahlung corrections are applied and the result is hadronized. This means that the color carrying partons are to recombine into color neutral mesons and baryons.

After this procedure, the four-vectors of the generated objects are handed over to a GEANT4[38] simulation of the ATLAS detector. Here, the particles are propagated through a three-dimensional model of the detector and the energy depositions in the various sensors they pass are estimated. GEANT4 is not only capable of simulating the detector with all its sub-components and different materials in great detail but also to let charged particles get deflected by electromagnetic fields and instable particles decay on their way. In the next step the detector response to the determined energy depositions is simulated and saved in a data format equivalent to that of the real data recorded by ATLAS. The event and object reconstruction thereafter is the same as for real data.

6.2. Monte Carlo Samples

In this thesis's $Z \to \mu\mu$ signal process, the PYTHIA event generator[39, 40] is used which emphasizes on processes with strongly interacting particles. A collection of background samples is selected to generate an environment as closely to the real physics environment present in the collisions as possible. This set consists of samples produced by MC@NLO[41] or ALPGEN[42] generators. Because the number of generated events as well as the cross section of the corresponding processes spread over a large region, the Monte Carlo samples have to be reweighted in a way, that they correspond all to the same luminosity, i.e. the luminosity of the signal sample (see equation 2.17). An overview of the used Monte Carlo samples and the most important numbers is given in table 6.1 (see appendix A.2 for full dataset names). The lowest order Feynman diagrams for those processes are given in figure 6.1.

Table 6.1.: The used data samples, their number of events, corresponding luminosity and weighting factors to fit the luminosity of signal sample. In the $c\bar{c}$ and $b\bar{b}$ samples, at least one of the quarks decays into a muon with a transverse momentum higher than 15 GeV.

Process	# of Events	$\mathcal{L}$ in pb^{-1}	Weighting Factor
2010 Data	12 019 135	37.4	/
Signal Sample:			
$Z \to \mu\mu$	299 964	359.4	1
Background:			
$Z \to \tau\tau$	399 000	467.2	0.7693
$W \to \mu\nu$	863 872	110.1	3.265
$W \to \tau\nu$	998 868	127.3	2.823
$c\bar{c} \to \mu + X$	1 467 218	38.01	9.456
$b\bar{b} \to \mu + X$	4 473 780	60.54	5.937
$t\bar{t}$	771 423	9630	3.732×10^{-2}
single top:			
– t-channel	118 384	16 640	2.161×10^{-2}
– s-channel	8449	18 036	1.993×10^{-2}
– Wt-channel	265 668	18 211	1.974×10^{-2}

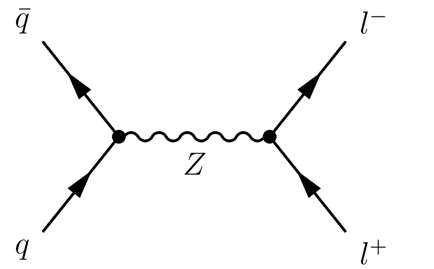

(a) Z production and decay

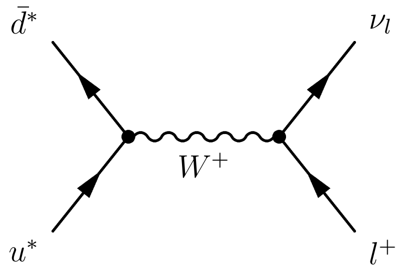

(b) W production and decay

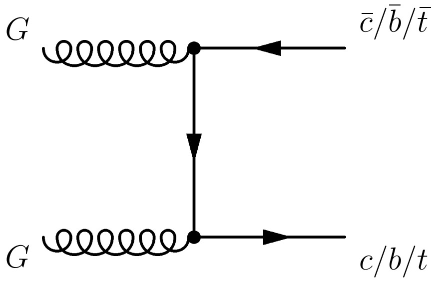

(c) $c\bar{c}$, $b\bar{b}$ and $t\bar{t}$ production

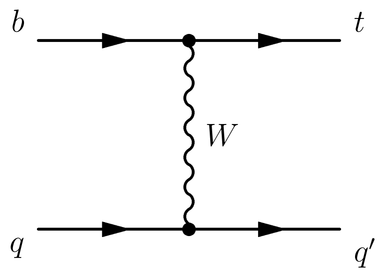

(d) single top production, t-channel

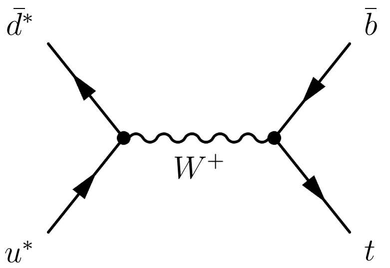

(e) single top production, s-channel

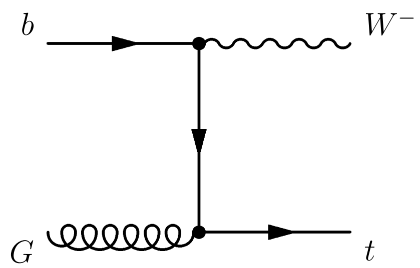

(f) single top production, Wt-channel

Figure 6.1.: Feynman diagrams of the used Monte Carlo processes. The leptons $l^\pm$ may be muons or tauons. Quarks u^* and d^* are meant to be read as any up- and down-type, respectively. Charge conjugation is always implied where applicable.

7. Results

In this chapter, the muon reconstruction efficiencies and scale factors in bins of p_{T}, η, ϕ, ΔR between the muon candidate and the nearest jet, number of jets and p_{T} of the leading jet as well as an estimation of the background contamination are presented.

7.1. Efficiencies and Scale Factors

Scale factors are the ratios of the efficiencies found in data and predicted by Monte Carlo simulations:

$$SF(x) = \varepsilon^{\mathrm{data}}(x)/\varepsilon^{\mathrm{MC}}(x), \tag{7.1}$$

where the efficiencies depend on an arbitrary variable x (e.g. p_{T}, η, number of jets in the event). They are particularly important if one wants to compare real data with Monte Carlo predictions in search of new physics, especially if they deviate significantly from unity. The scale factors are provided for every distribution as the combined and inner detector efficiencies are: p_{T}, η, ϕ, ΔR to the nearest jet, number of jets and p_{T} of the leading jet (i.e. the most energetic one).

The average MS and matching efficiency has been determined to 96.93% in data and 96.83% in Monte Carlo including all background samples. It follows a flat distribution in all variables except for a clear efficiency loss in $|\eta| \lesssim 0.1$ (service access) and $|\eta| \approx 1.2$ (transition region). The inner detector efficiency was measured as 98.84% in data and 99.02% in Monte Carlo. Again, a clear η-dependence is visible, while the efficiency does not depend on any other variable. Like the combined muons, the calorimeter tagged muons suffer from efficiency loss in the region around $|\eta| = 1.1$ but additionally from muons with low transverse momentum ($p_{\mathrm{T}} < 30$ GeV). Their average reconstruction efficiency is 98.88% in data ind 98.62% in Monte Carlo. The scale factors are very close to unity, yielding an excellent agreement between data and Monte Carlo in terms of muon reconstruction: $SF^{\text{MS+matching}} = 1.001$, $SF^{\mathrm{ID}} = 0.998$ and $SF^{\mathrm{CT}} = 1.003$.

For an overview of all average reconstruction efficiencies and scale factors, including statistical and systematical errors, see table 7.1. The efficiencies in dependence of the various phase space and jet variables can be found in figures 7.4–7.6 for the MS and matching efficiencies, in figures 7.7–7.9 for the inner detector efficiencies and in figures 7.10–7.12 for the calorimeter tagged efficiencies. Plots binned two dimensional in p_{T} and η can be found in A.3.

Table 7.1.: Average muon reconstruction efficiencies in Monte Carlo simulation and recorded ATLAS data, including statistical and systematical errors and scale factors.

Signal-MC only	
MS and Matching Efficiency:	$96.89 \pm 0.04(\mathrm{stat}) \pm 0.04(\mathrm{syst})\%$
Inner Detector Efficiency:	$99.04 \pm 0.04(\mathrm{stat}) \pm 0.04(\mathrm{syst})\%$
Calorimeter Muon Efficiency:	$98.85 \pm 0.04(\mathrm{stat})\%$
Truth Muon Efficiency:	$96.49 \pm 0.03(\mathrm{stat})\%$
Calorimeter Purity:	$99.78 \pm 0.01(\mathrm{stat})\%$

Data and MC (signal + background)	
Data:	
MS and Matching Efficiency:	$96.93 \pm 0.12(\mathrm{stat})\%$
Inner Detector Efficiency:	$98.84\,^{+0.14}_{-0.16}(\mathrm{stat})\%$
Calorimeter Muon Efficiency:	$98.88\,^{+0.14}_{-0.15}(\mathrm{stat})\%$
Monte Carlo:	
MS and Matching Efficiency:	$96.83 \pm 0.04(\mathrm{stat}) \pm 0.04(\mathrm{syst})\%$
Inner Detector Efficiency:	$99.02 \pm 0.04(\mathrm{stat}) \pm 0.03(\mathrm{syst})\%$
Calorimeter Muon Efficiency:	$98.62 \pm 0.05(\mathrm{stat})\%$
Scale Factor:	
MS and Matching Efficiency:	$1.001 \pm 0.001(\mathrm{total})$
Inner Detector Efficiency:	$0.998 \pm 0.002(\mathrm{total})$
Calorimeter Muon Efficiency:	$1.003 \pm 0.002(\mathrm{stat})$

7.1.1. Error Calculation

The statistical errors on the efficiencies were estimated using Clopper-Pearson intervals[43]. This is the standard implementation in the ROOT framework. The Clopper-Pearson interval guarantees that the actual coverage probability is always equal to or above the nominal confidence level.

For systematical errors, several uncertainties were taken into account: the combined muon, stand-alone muon, the inner detector and jet momentum uncertainties as well as the jet energy scale uncertainty. These uncertainties were provided by the corresponding ATLAS combined performance groups: *Combined Muon Working Group*, *Jet/EtMiss Working Group* and *Inner Tracking Working Group*. In Monte Carlo simulated events, the momenta were separately smeared by a Gaussian with the corresponding uncertainty as its standard deviation. Additionally, the jet momenta were (always) risen and (always) lowered by the respective jet energy scale uncertainty. Using the modified objects for the analysis leads to additional results: $\varepsilon_{\text{tag smeared}}$, $\varepsilon_{\text{probe smeared}}$, $\varepsilon_{\text{jet smeared}}$, $\varepsilon_{\text{jet scaled up}}$ and $\varepsilon_{\text{jet scaled down}}$. The absolute difference between the nominal efficiency and the modified one is used as the respective error, where, with respect to the jet energy scale errors, only the bigger one is used: $\Delta_{\text{tag smeared}}$, $\Delta_{\text{probe smeared}}$, $\Delta_{\text{jet smeared}}$ and $\Delta_{\text{jet scale}} = \max(\Delta_{\text{jet scaled up}}, \Delta_{\text{jet scaled down}})$. Assuming high correlation between the miss-measurements of combined muon and inner detector track—the combined track is build from an inner detector track, after all—their errors are added linearly and afterwards added in quadrature with the jet errors:

$$\Delta_{\text{syst.}} = \sqrt{(\Delta_{\text{tag smeared}} + \Delta_{\text{probe smeared}})^2 + (\Delta_{\text{jet smeared}})^2 + (\Delta_{\text{jet scale}})^2}. \tag{7.2}$$

Statistical and systematical errors are added in quadrature:

$$\Delta_{\text{all}} = \sqrt{(\Delta_{\text{syst.}})^2 + (\Delta_{\text{stat.}})^2}. \tag{7.3}$$

The upper (lower) errors of the scale factors are a combination of the upper (lower) data and lower (upper) Monte Carlo errors and calculated as follows:

$$\Delta^{\text{SF}}_{\text{up/down}} = \sqrt{\left(\Delta^{\text{data}}_{\text{up/down}} \times \frac{1}{\varepsilon_{\text{MC}}}\right)^2 + \left(\Delta^{\text{MC}}_{\text{down/up}} \times \frac{\varepsilon_{\text{Data}}}{\varepsilon^2_{\text{MC}}}\right)^2}. \tag{7.4}$$

The errors in figures 7.4–7.12 include the statistical as well es the systematical uncertainties.

7.1.2. Truth Muons in Signal Monte Carlo

Using simulations, one has access to the values of the underlying physics produced by the event generator. In the muon case, these objects are called *truth muons*. With truth muons, the muon reconstruction efficiency can be estimated directly by matching them to baseline muons without the need of combining two separate measurements. This leads to $\varepsilon_{\text{truth}} = (96.49 \pm 0.03(\text{stat}))\%$, which agrees quite well with the combined efficiencies of $96.93\% \times 98.84\% = (95.81 \pm 0.19(\text{stat}))\%$ in data and $96.83\% \times 99.02\% = (95.88 \pm 0.07(\text{total}))\%$ in Monte Carlo. Additionally, the purity of the calorimeter tagged muon candidates can be estimated as the fraction of calorimeter tagged muon candidates matching truth muons. This leads to an estimated purity of $\rho_{\text{calo}} = (99.79 \pm 0.01(\text{stat}))\%$ (see figure 7.16–7.18). The calorimeter tagged muon purity is essentially 100% with drops of one percent at $p_{\text{T}}^{\text{calo muon}} < 30$ GeV, $|\eta| > 2$, $\Delta R < 0.05$ and $p_{\text{T}}^{\text{leading jet}} \approx 40$ GeV.

7.1.3. Background Estimation

The background contamination of the tag and probe selection can be estimated from Monte Carlo simulated events. For that, an additional weighting factor is applied to the Monte Carlo simulated events, so that the number of selected tag and ID-probe pairs after all cuts are equal in data and Monte Carlo simulations (signal + background). The number of background events then is the weighted number of selected tag and probe pairs from all background samples.

For an error estimation of the background contamination, the cross sections used to calculate the weighting factors have been varied by its experimental error.

This approach estimates the background contamination to 18 ± 2 muon pairs in contrast to $19\,860$ signal pairs, yielding a selection purity of 99.9%. The numbers of all selected muons (baseline, tag, probe and pairs) can be found in table 7.2.

The main background sources at the Z resonance are the $W \to \mu\nu$- and $t\bar{t}$-samples, as can be seen in figure 7.1. After the pair selection, they contribute with 5.4 ± 0.5 and $5.2^{+1.9}_{-1.5}$ muon pairs, respectively.

Table 7.2.: Numbers of selected muon objects: baseline, tag and probe muons as well as tag & probe pairs. For the background estimation, the Monte Carlo simulated events are normalized in a way that $N^{\mathrm{MC}}_{\mathrm{pairs}} = N^{\mathrm{Data}}_{\mathrm{pairs}}$, corresponding to a luminosity of $\mathscr{L} = 34\ \mathrm{pb}^{-1}$. This leads to a contamination of 18 muon pairs (0.1%) from background Monte Carlo simulated events.

Signal	Monte Carlo
Baseline Muons:	39 336
Tag Muons:	37 815
ID-Probe Muons:	37 058
SA-Probe Muons:	35 986
Muon Pairs (ID-Probes):	19 860

Signal + Background	Monte Carlo	Data
Baseline Muons:	606 591	831 551
Tag Muons:	549 849	757 195
ID-Probe Muons:	323 855	332 486
SA-Probe Muons:	325 661	321 842
Muon Pairs (ID-Probes):	19 878	19 878

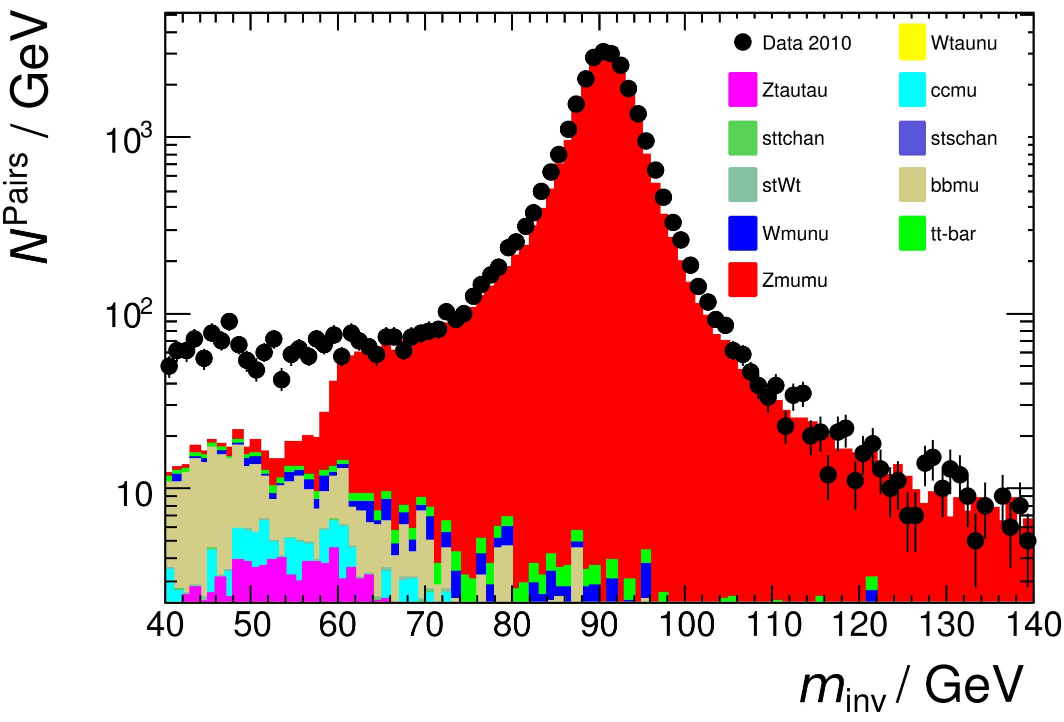

Figure 7.1.: Invariant di-muon mass after tag and ID-probe selection but before applying pair cuts. The discrepancy between data and Monte Carlo simulation in the region below 60 GeV is due to a cut during the event generation.

7.2. Effects of a $\Delta\phi$ Cut

A cut on the angular separation between the tag and probe muon candidates was applied to investigate its effects. For this reason, the transverse momentum of the Z boson candidate, defined as the as the transverse component of the summed tag and probe muon candidates' momenta:

$$p_{\mathrm{T}}^{\mathrm{Z}} = \left(\vec{p}^{\mu 1} + \vec{p}^{\mu 2}\right)_{\mathrm{T}} = \sqrt{\left(p_{\mathrm{x}}^{\mu 1} + p_{\mathrm{x}}^{\mu 2}\right)^2 + \left(p_{\mathrm{y}}^{\mu 1} + p_{\mathrm{y}}^{\mu 2}\right)^2}, \tag{7.5}$$

has been plotted after the standard pair selection with and without the cut on $\Delta\phi > 2$ (see figures 7.2 and 7.3). The number of Z boson candidates decrease because of this cut at transverse momenta of more than 30 GeV. In the high transverse momentum region ($p_{\mathrm{T}} \approx 100$ GeV), the cut reduces the number of Z boson candidates by an order of magnitude. This leads to a background reduction of 4 (weighted) events (22%) and a loss of 1098 (5.5%) tag and probe pairs in Monte Carlo signal and 1053 (5.3%) in data, which improves the signal to background ratio by a factor of 1.2. Because the background contamination is already of the order of a per mil, a $\Delta\phi$ cut was not applied for the efficiency studies. Although, it can be useful for analyses where the background contamination is a bigger problem.

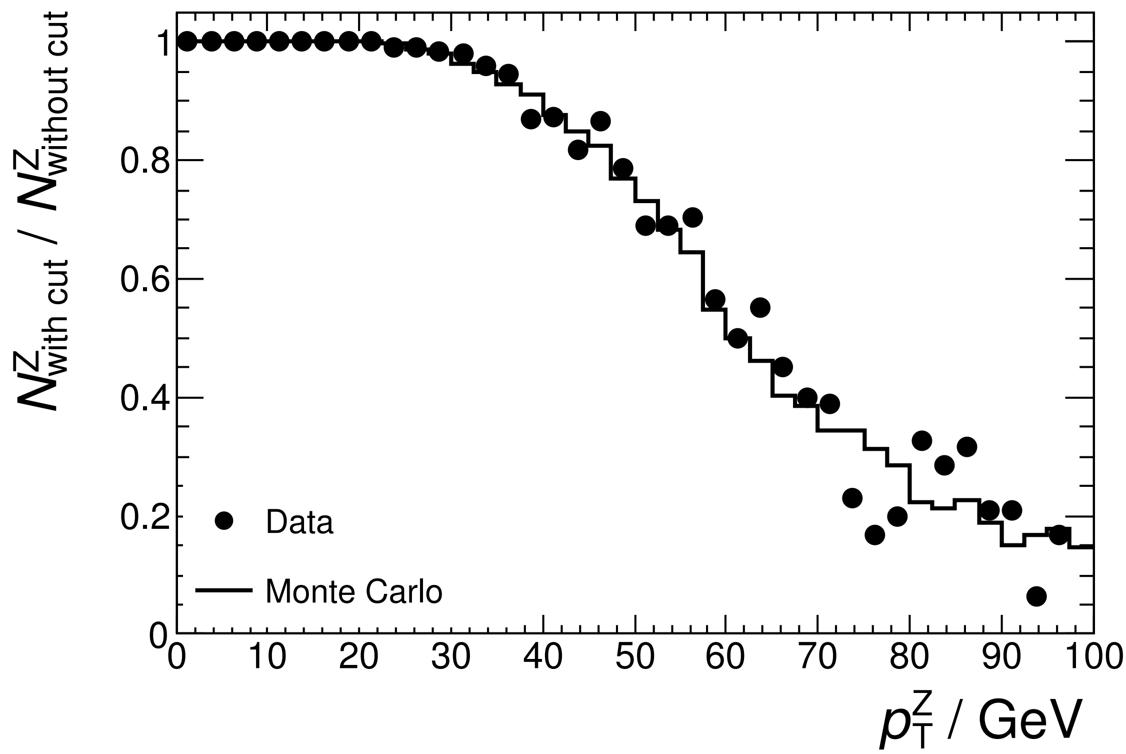

Figure 7.2.: The relative loss of Z candidates as a function of the Z's p_{T} due to a $\Delta\phi < 2.0$ cut between the combined tag muon and the inner detector probe muon.

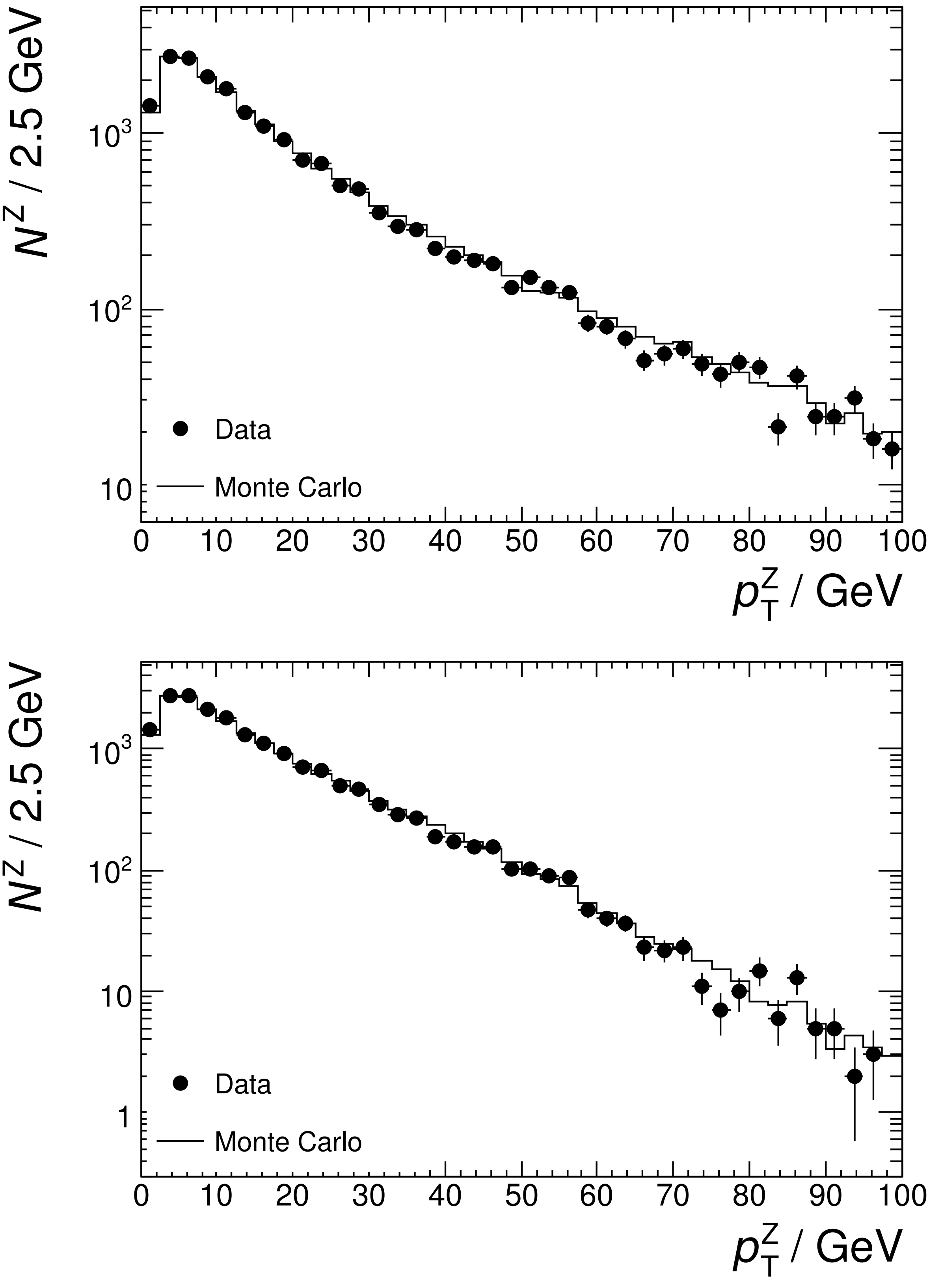

Figure 7.3.: The p_T distribution of the Z boson candidates, defined as the transverse component of the summed tag and probe momenta, without (top) and with (bottom) a cut on the angular separation of $\Delta\phi > 2$ between the two muon candidates.

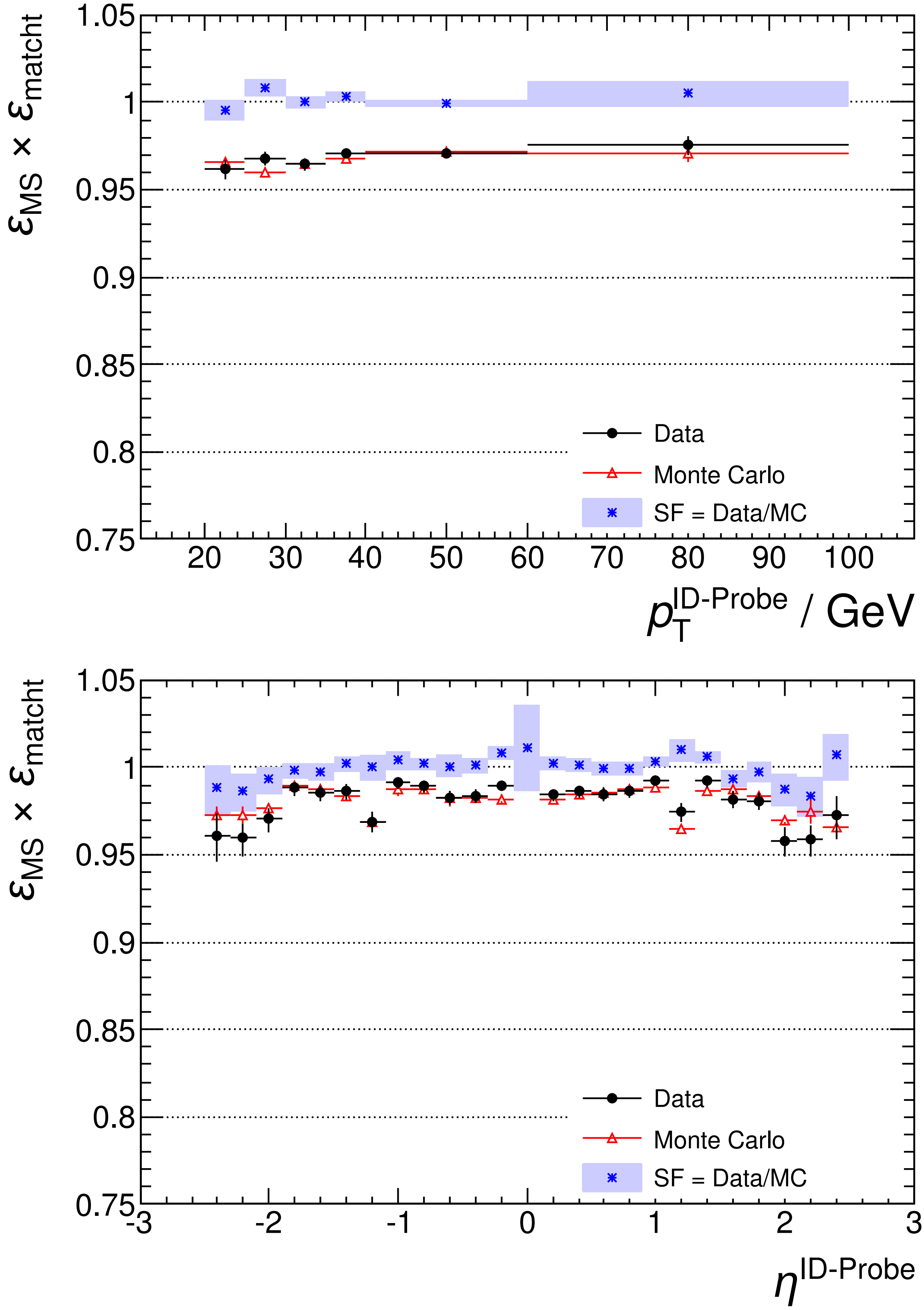

Figure 7.4.: Muon spectrometer and matching efficiencies of baseline muons in ATLAS recorded data (black dots) and Monte Carlo simulation (red triangles) as well as the corresponding scale factors (blue boxes) as a function of p_T (top) and η (bottom).

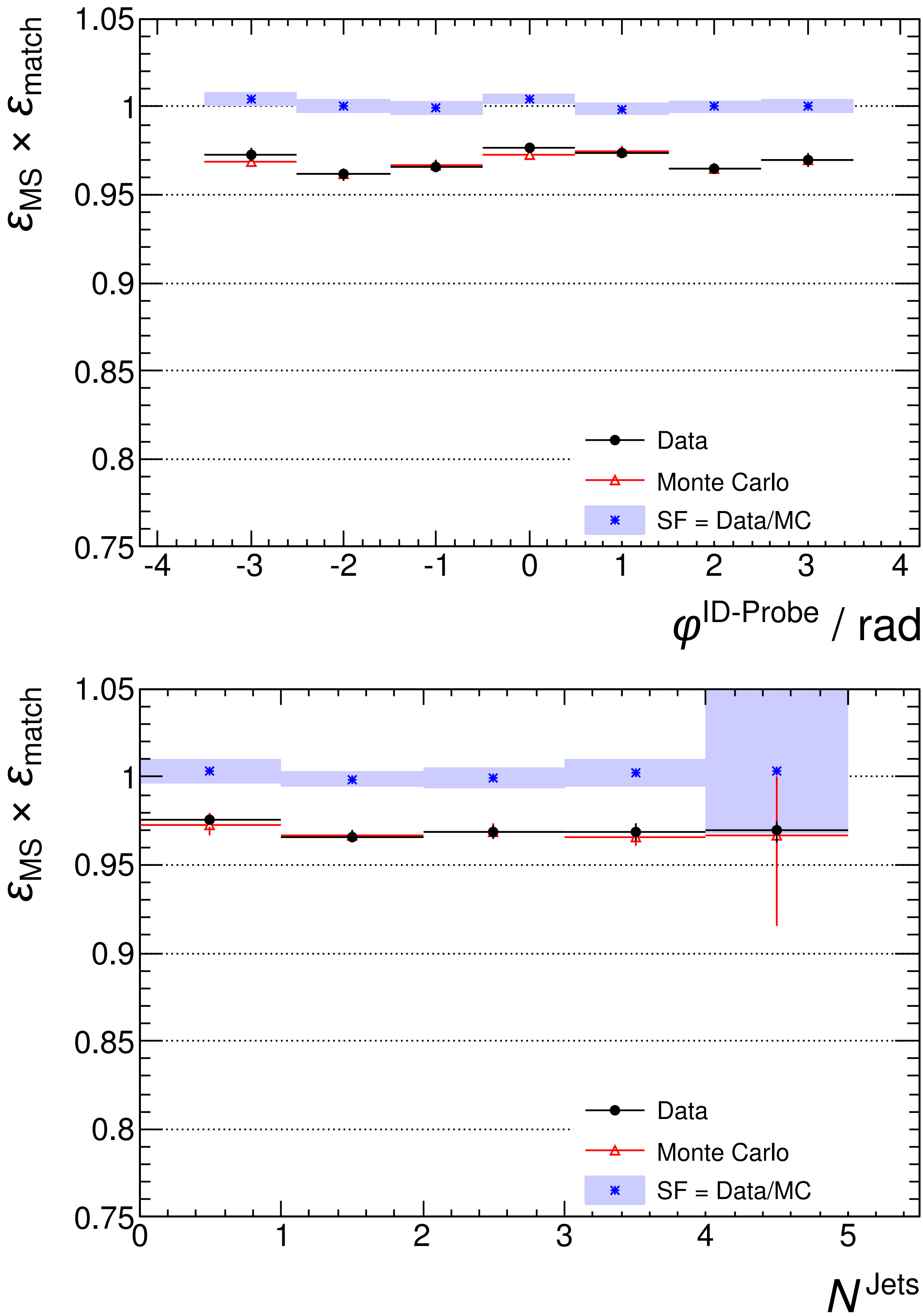

Figure 7.5.: Muon spectrometer and matching efficiencies of baseline muons in ATLAS recorded data (black dots) and Monte Carlo simulation (red triangles) as well as the corresponding scale factors (blue boxes) as a function of ϕ (top) and the number of jets (bottom).

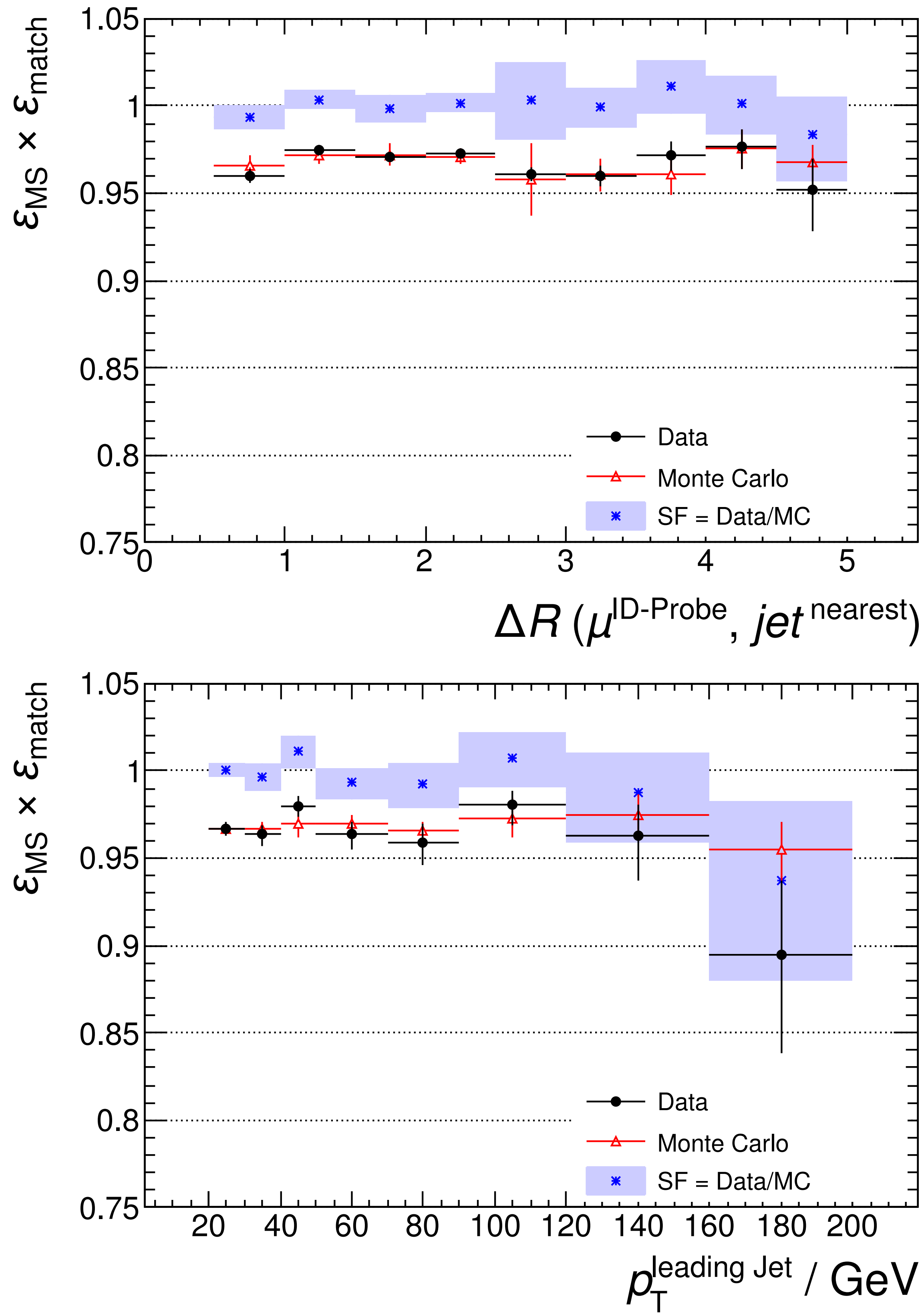

Figure 7.6.: Muon spectrometer and matching efficiencies of baseline muons in ATLAS recorded data (black dots) and Monte Carlo simulation (red triangles) as well as the corresponding scale factors (blue boxes) as a function of ΔR to the nearest jet (top) and the p_T of the leading jet (bottom).

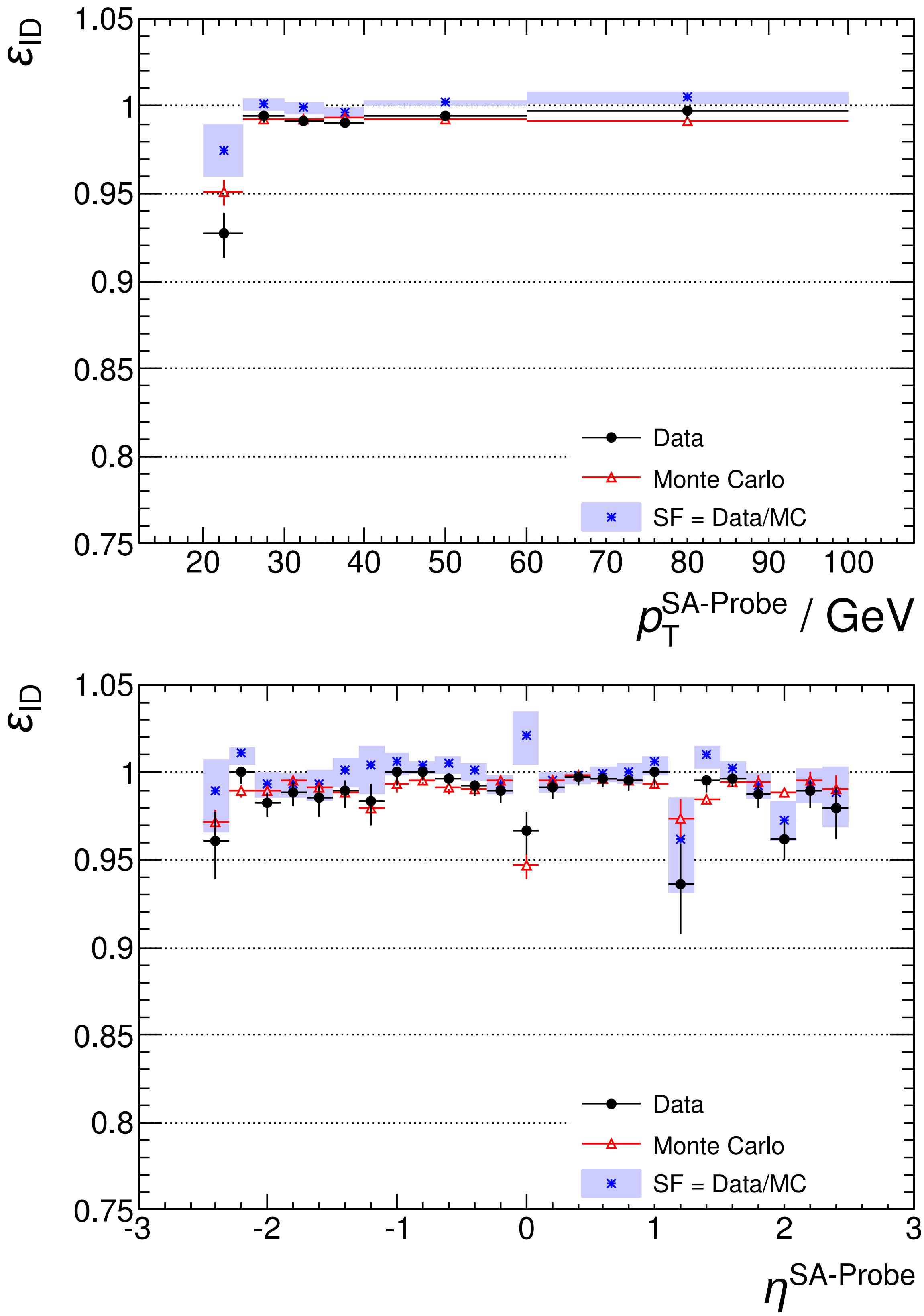

Figure 7.7.: Inner detector efficiencies of baseline muons in ATLAS recorded data (black dots) and Monte Carlo simulation (red triangles) as well as the corresponding scale factors (blue boxes) as a function of p_T (top) and η (bottom).

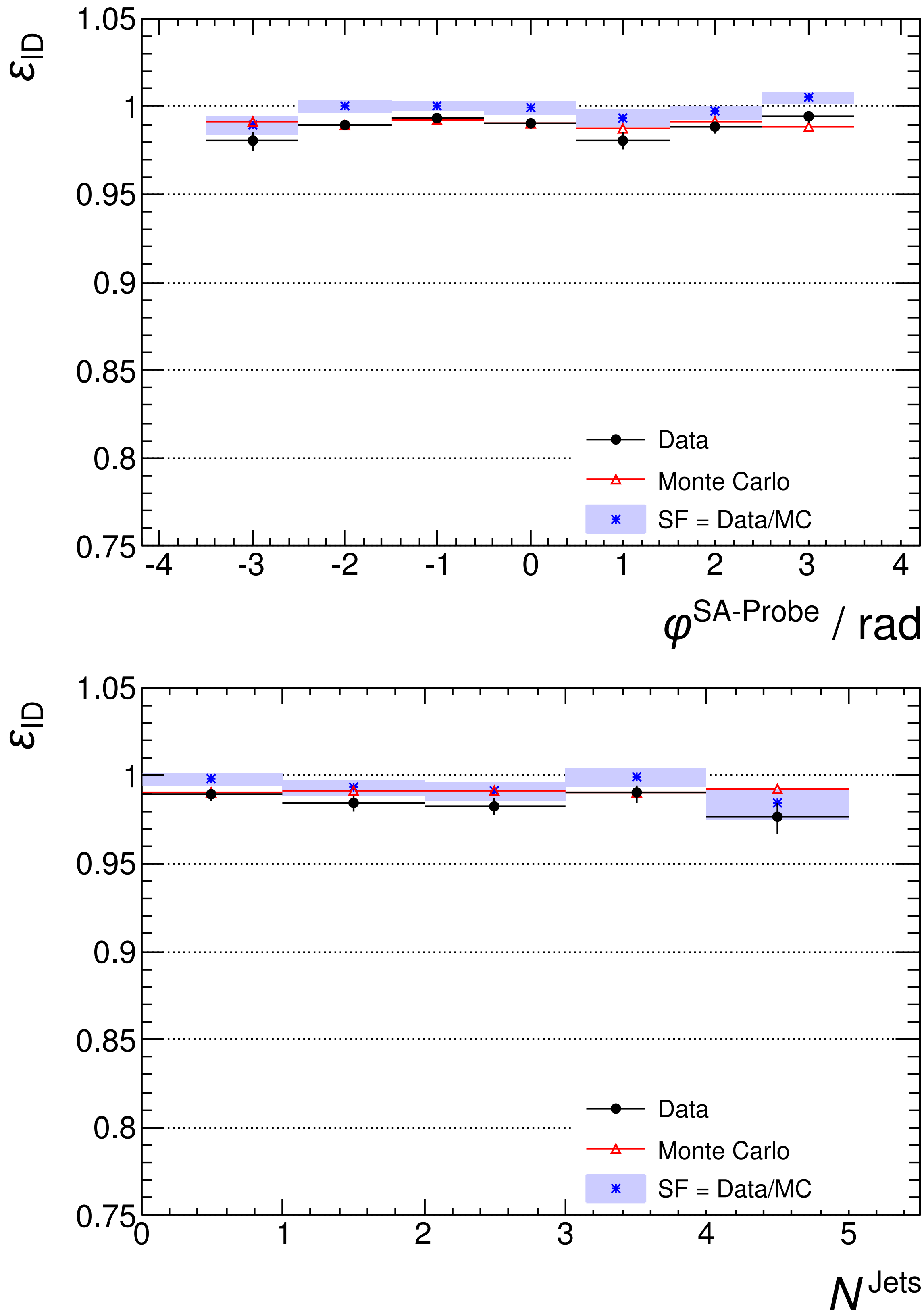

Figure 7.8.: Inner detector efficiencies of baseline muons in ATLAS recorded data (black dots) and Monte Carlo simulation (red triangles) as well as the corresponding scale factors (blue boxes) as a function of ϕ (top) and the number of jets (bottom).

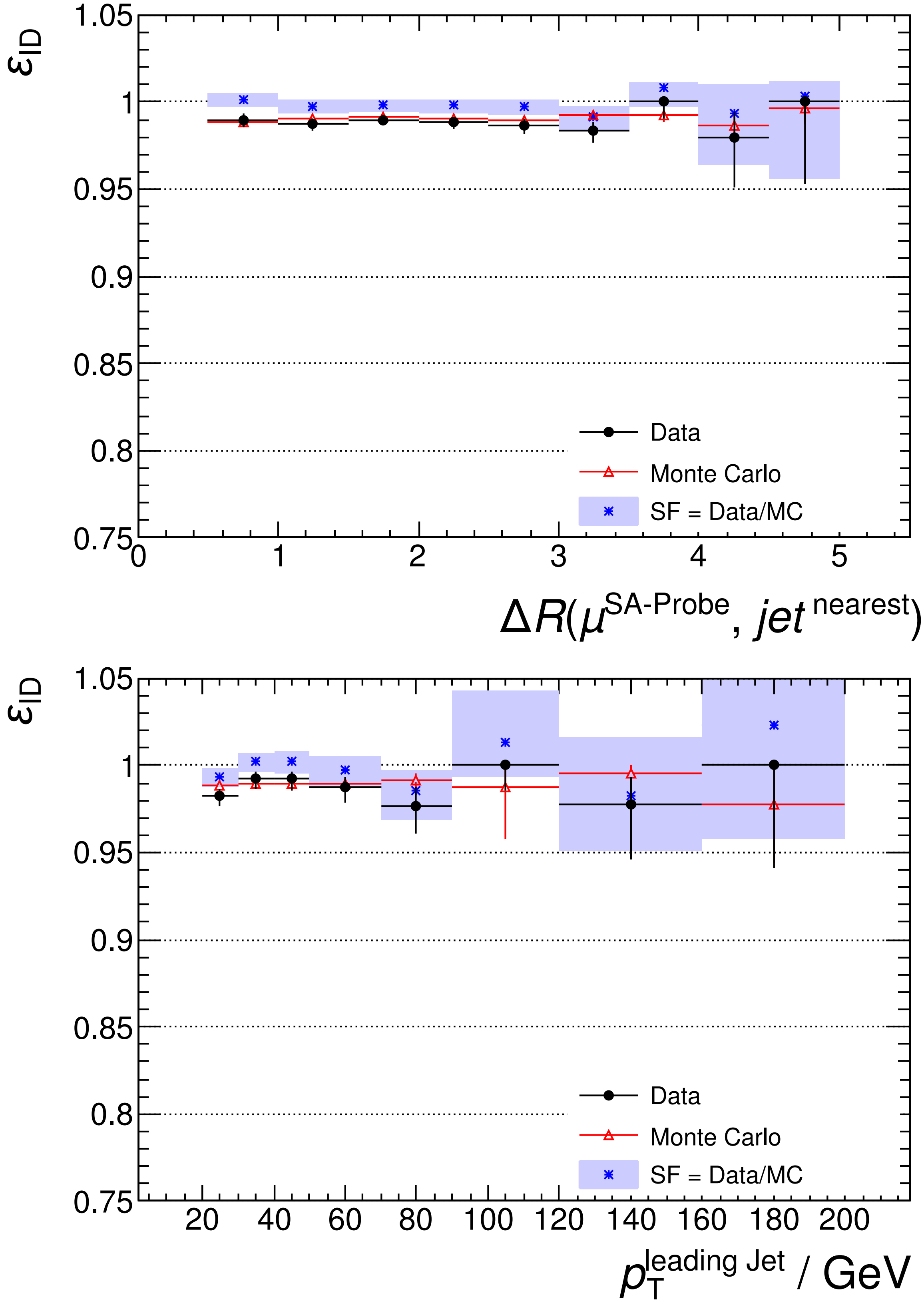

Figure 7.9.: Inner detector efficiencies of baseline muons in ATLAS recorded data (black dots) and Monte Carlo simulation (red triangles) as well as the corresponding scale factors (blue boxes) as a function of ΔR to the nearest jet (top) and the p_{T} of the leading jet (bottom).

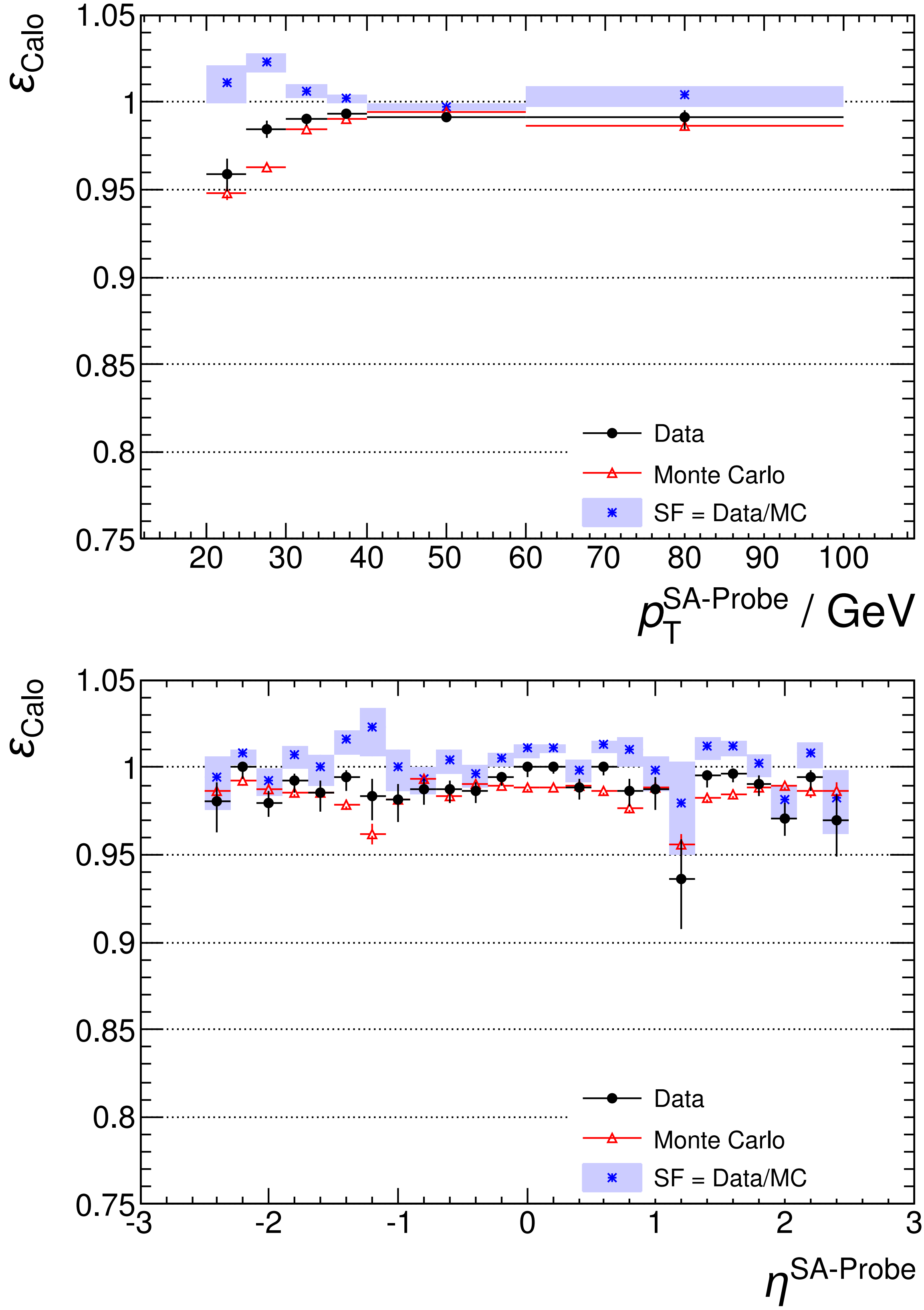

Figure 7.10.: Calorimeter tagged muon efficiency in ATLAS recorded data (black dots) and Monte Carlo simulation (red triangles) as well as the corresponding scale factors (blue boxes) as a function of p_T (top) and η (bottom).

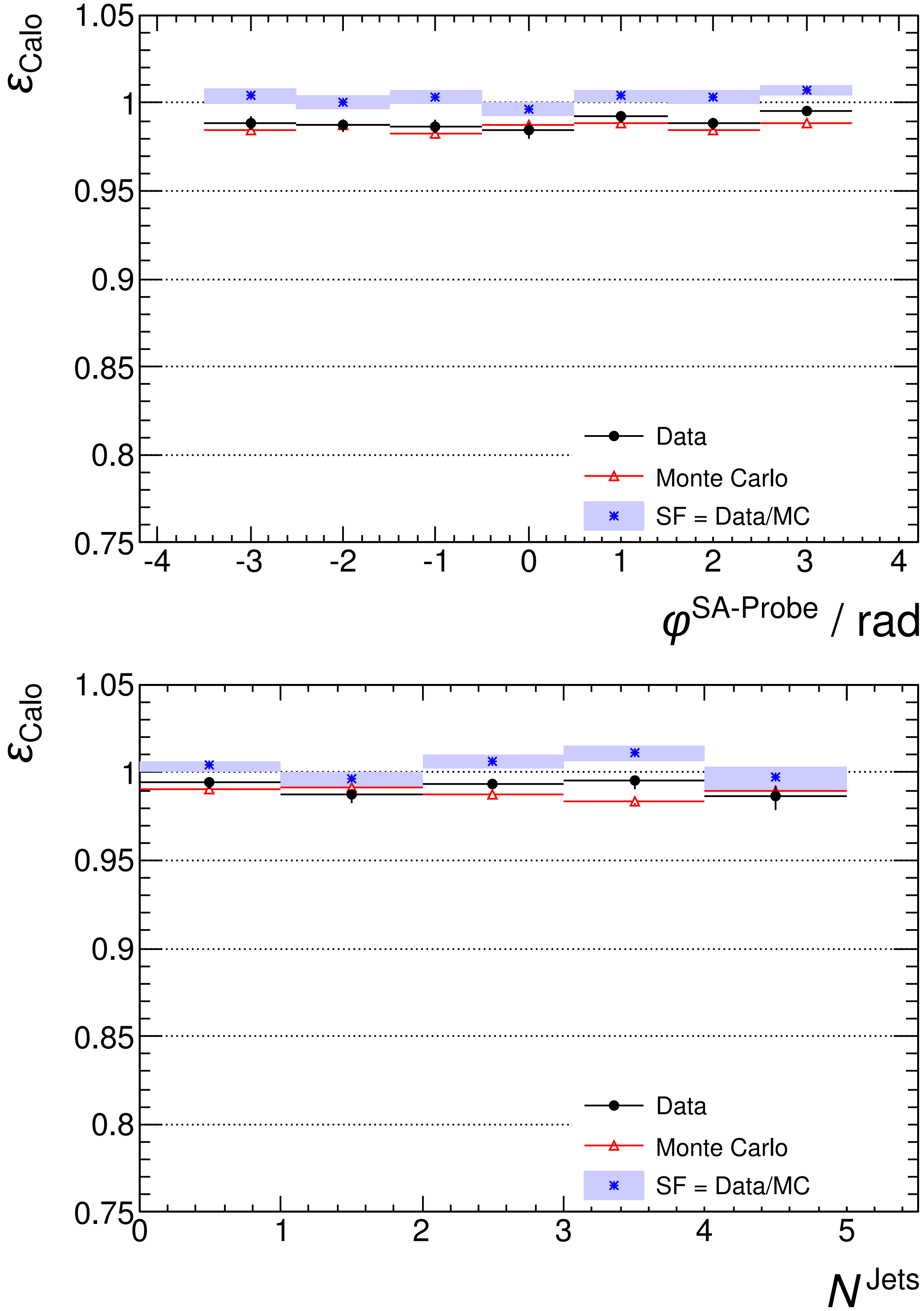

Figure 7.11.: Calorimeter tagged muon efficiency in ATLAS recorded data (black dots) and Monte Carlo simulation (red triangles) as well as the corresponding scale factors (blue boxes) as a function of ϕ (top) and the number of jets (bottom).

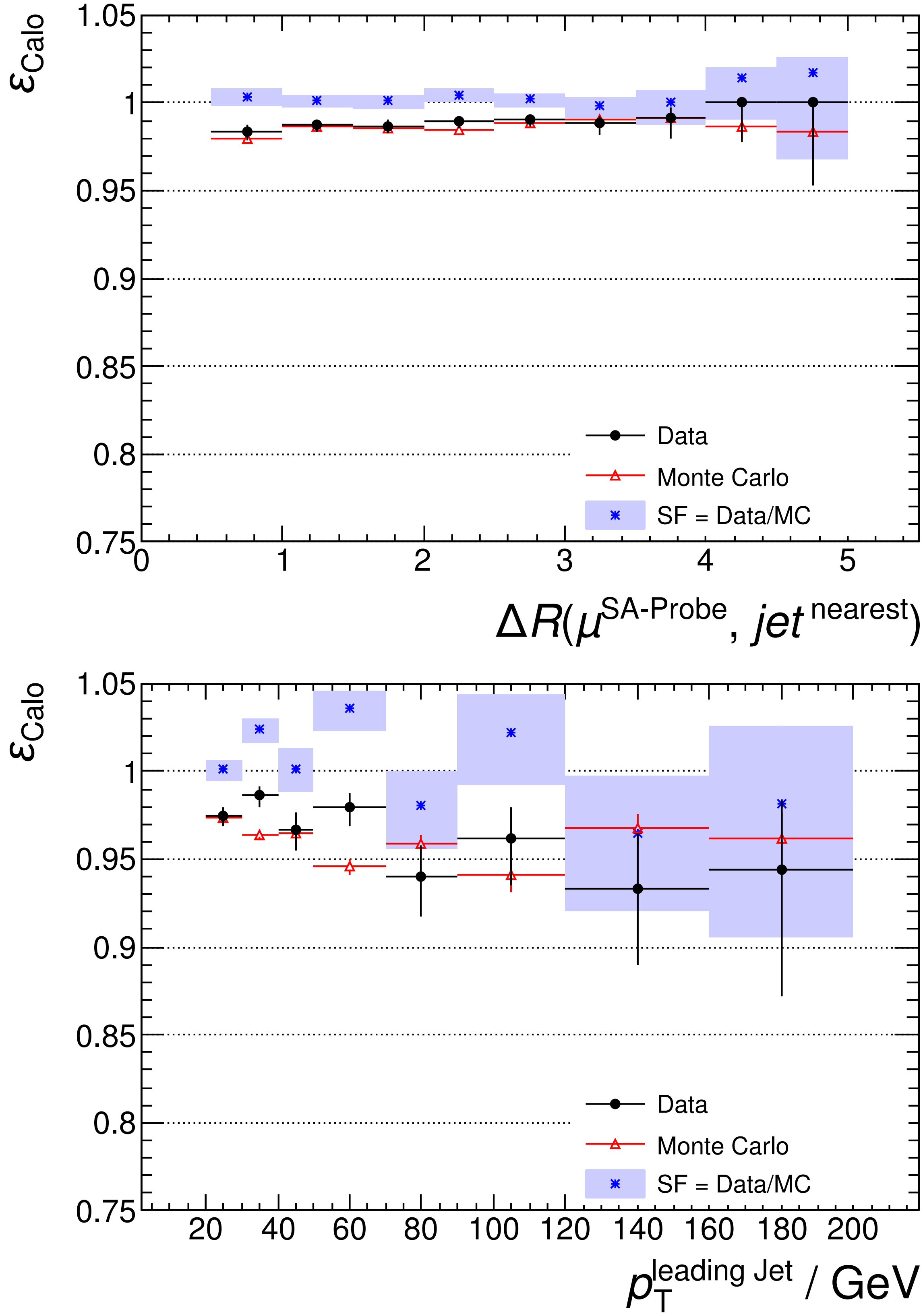

Figure 7.12.: Calorimeter tagged muon efficiency in ATLAS recorded data (black dots) and Monte Carlo simulation (red triangles) as well as the corresponding scale factors (blue boxes) as a function of ΔR to the nearest jet (top) and the p_T of the leading jet (bottom).

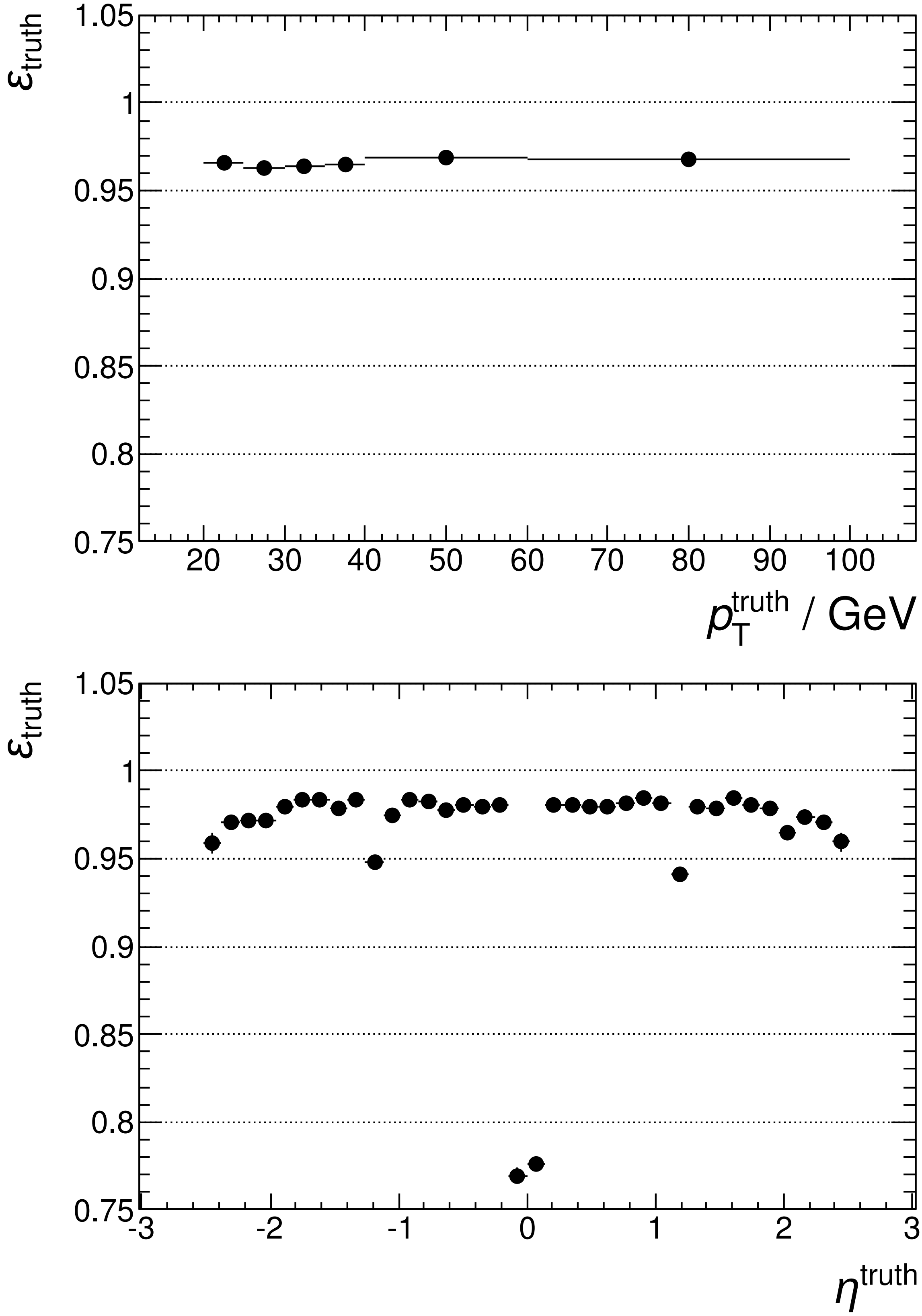

Figure 7.13.: Reconstruction efficiencies of truth muons in Monte Carlo simulated signal events as a function of p_T (top) and η (bottom).

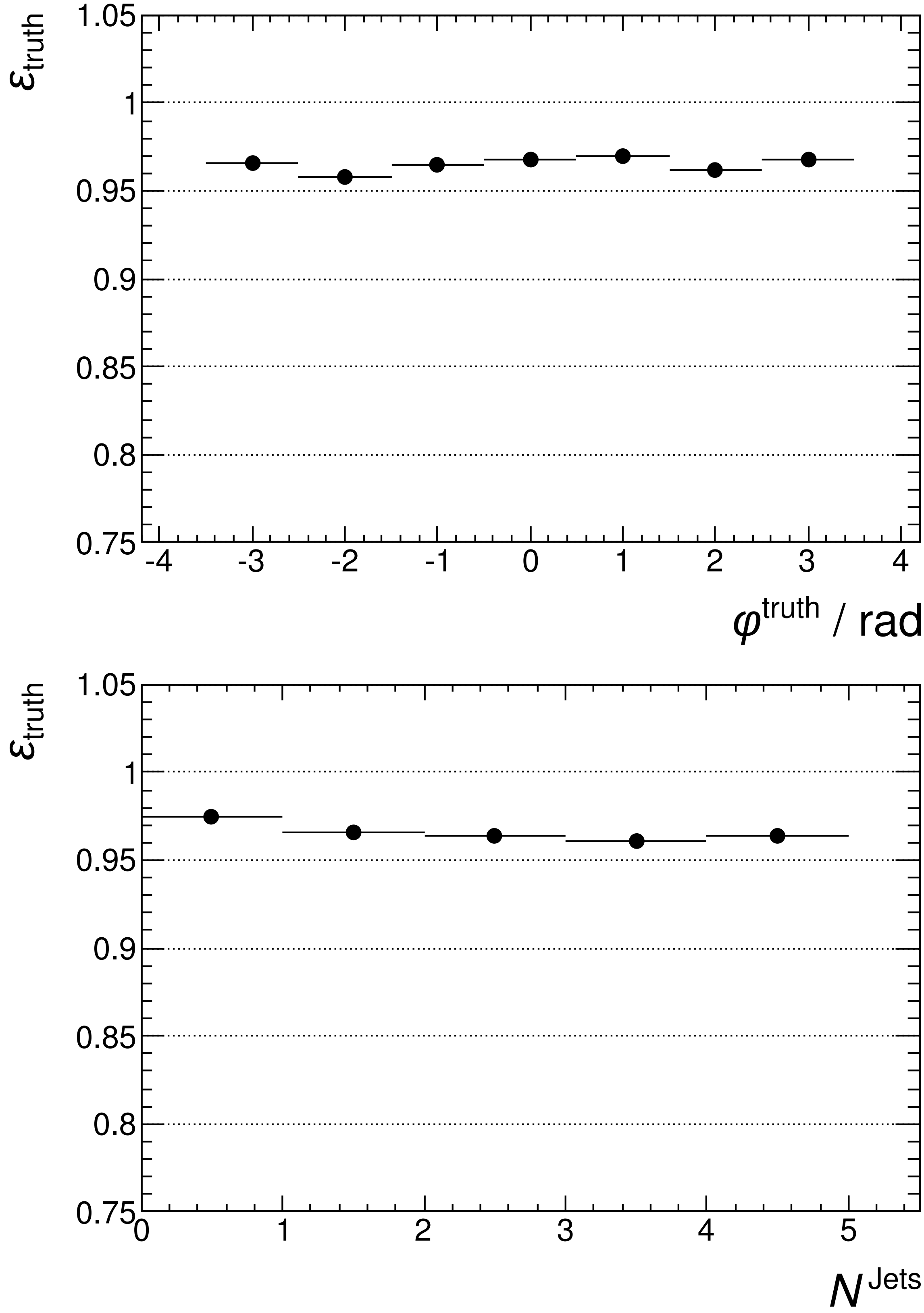

Figure 7.14.: Reconstruction efficiencies of truth muons in Monte Carlo simulated signal events as a function of ϕ (top) and the number of jets (bottom).

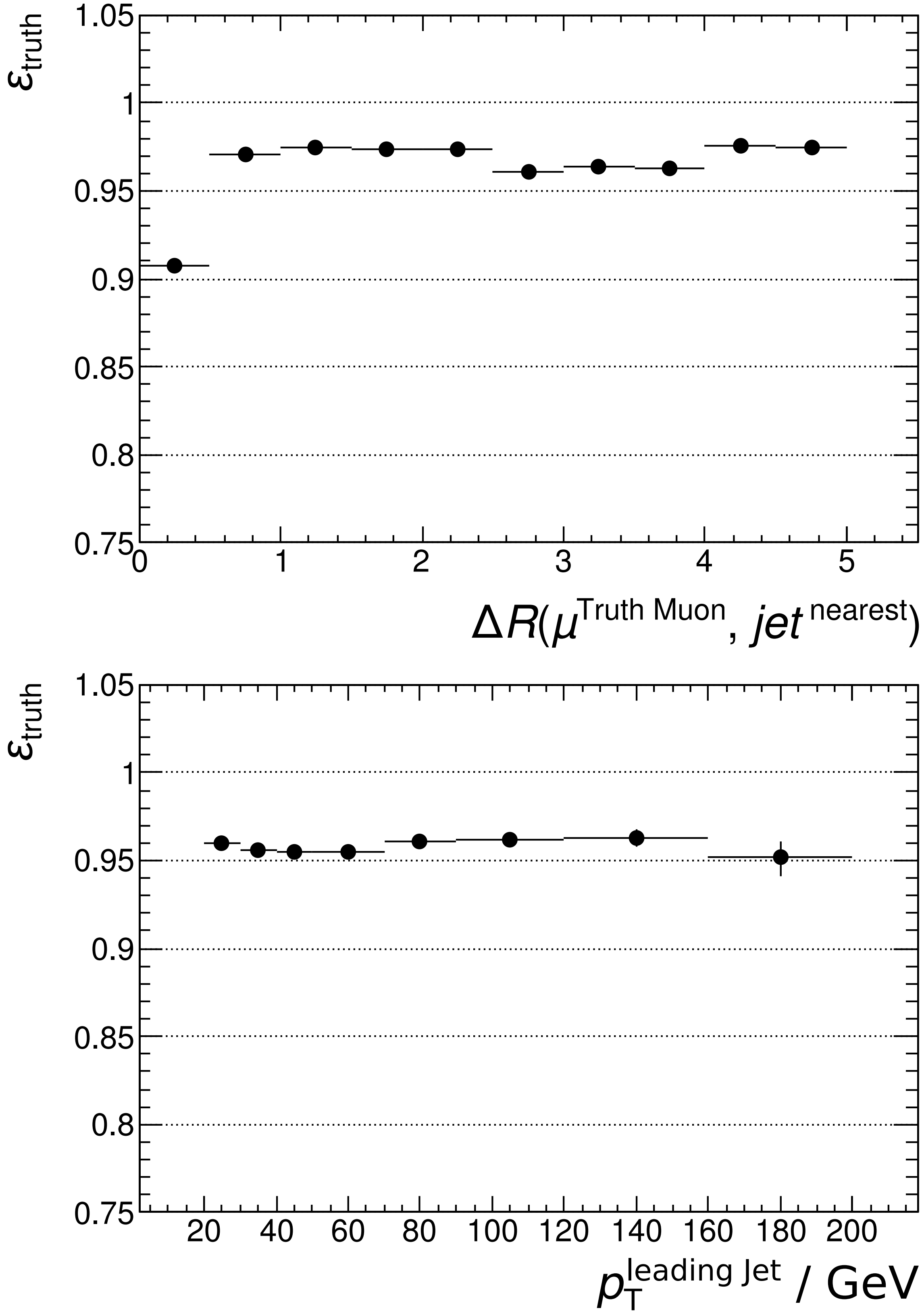

Figure 7.15.: Reconstruction efficiencies of truth muons in Monte Carlo simulated signal events as a function of ΔR to the nearest jet (top) and the p_T of the leading jet (bottom).

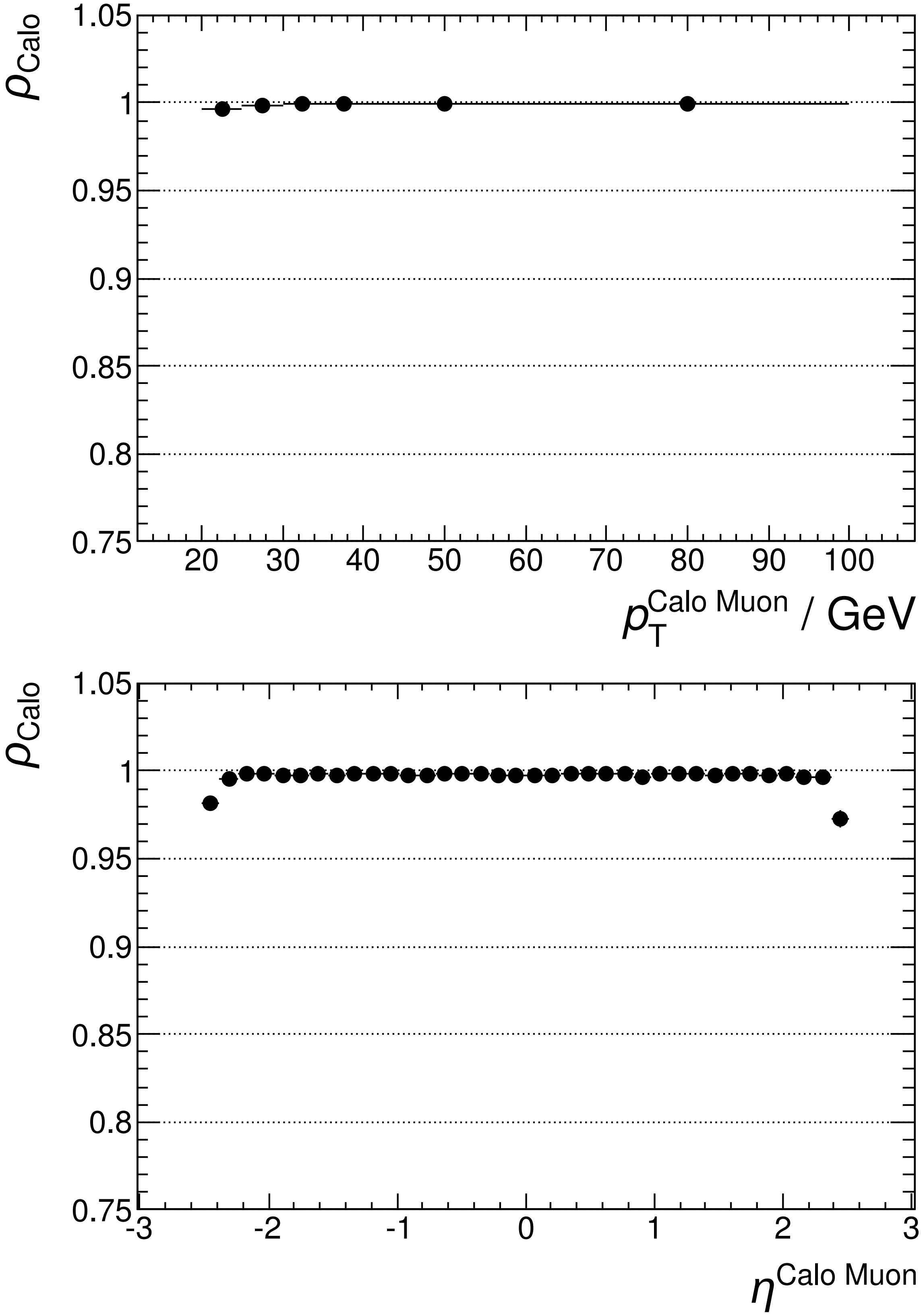

Figure 7.16.: Calorimeter tagged muon purity in Monte Carlo simulated signal events as a function of p_{T} (top) and η (bottom).

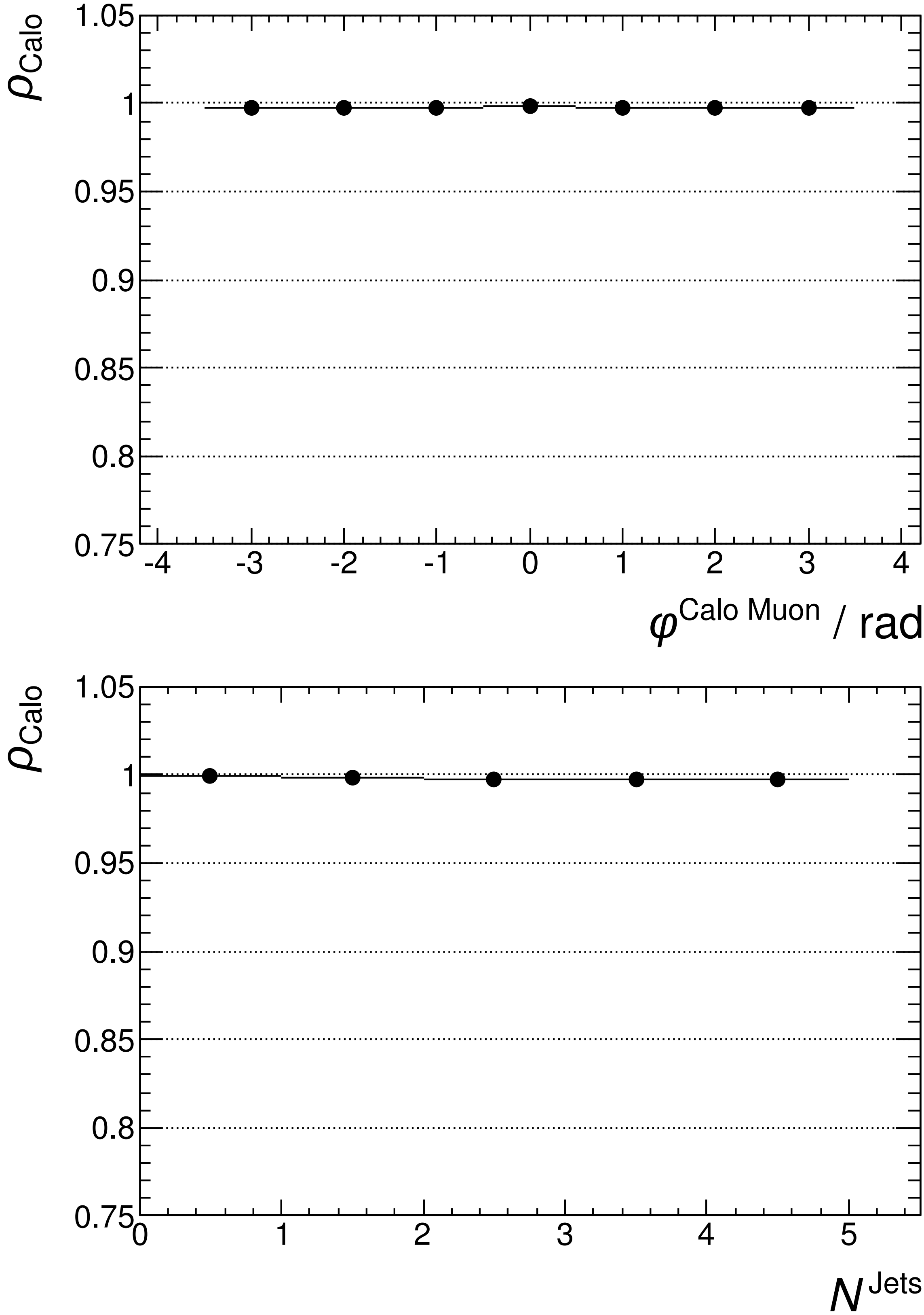

Figure 7.17.: Calorimeter tagged muon purity in Monte Carlo simulated signal events as a function of ϕ (top) and the number of jets (bottom).

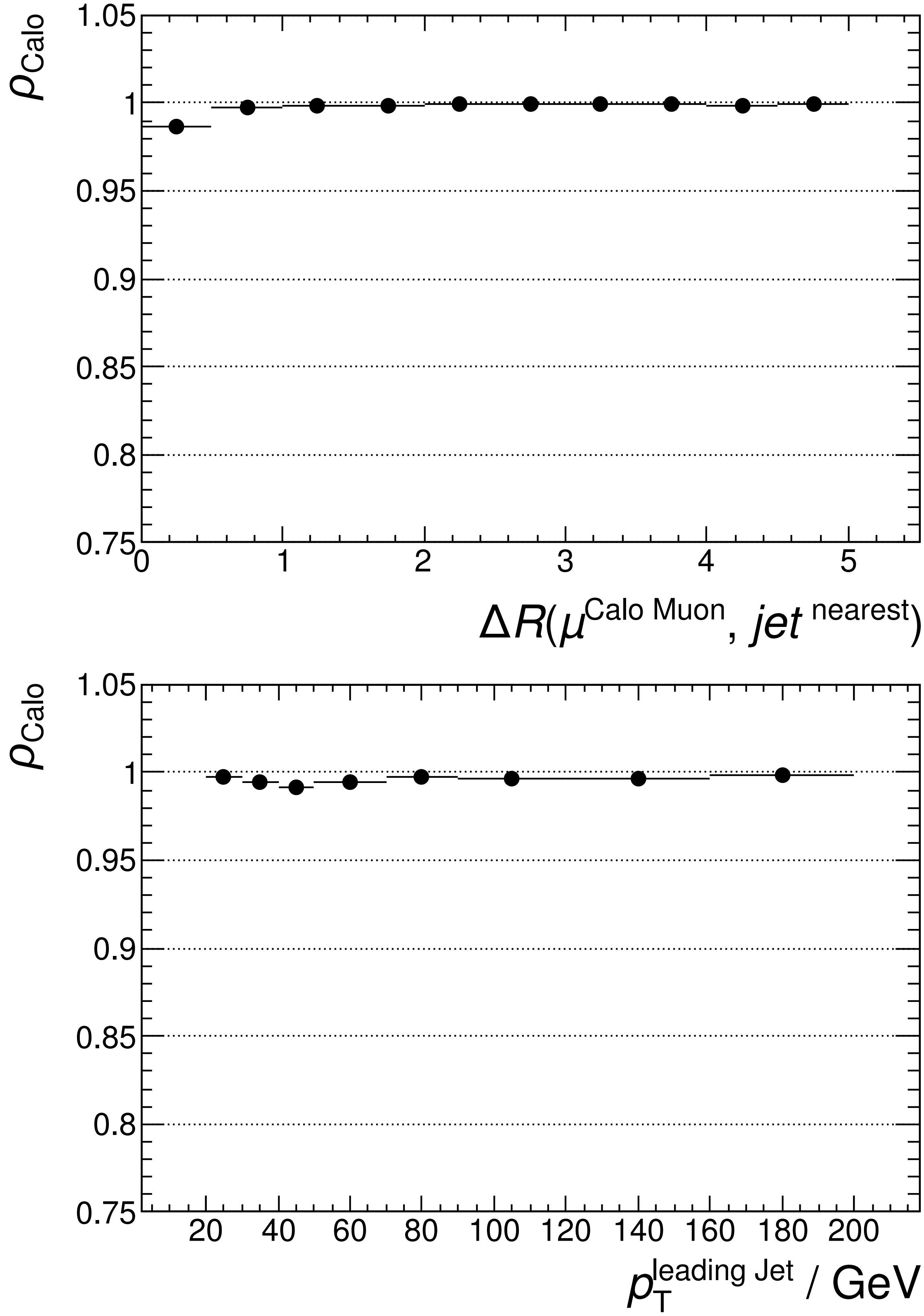

Figure 7.18.: Calorimeter tagged muon purity in Monte Carlo simulated signal events as a function of ΔR to the nearest jet (top) and the p_T of the leading jet (bottom).

8. Conclusion

The efficiency of muon reconstruction has been determined in data recorded by the ATLAS detector as well as in Monte Carlo simulations. For this task, a clean sample of $Z \to \mu\mu$ events has been selected with the tag and probe method. The background contamination was estimated from Monte Carlo simulations and has been determined to one tenth of a percent (0.1%).

The efficiency to reconstruct combined muon candidates in the ATLAS detector is the product of three separate efficiencies: The efficiency that the inner detector reconstructs the muon candidate, that the muon spectrometer reconstructs it and the efficiency of combining this two tracks to a combined one. They have been obtained in two distinct analyses and were combined in the end.

The results of $\varepsilon_{\text{reco}}^{\text{data}} = (95.8 \pm 0.19(\text{stat}))\%$ for data and $\varepsilon_{\text{reco}}^{\text{MC}} = (95.9 \pm 0.07(\text{total}))\%$ for Monte Carlo are mostly independent of all examined variables except for some specific regions in η. The average scale factor $SF_{\text{reco}} = \varepsilon_{\text{reco}}^{\text{data}}/\varepsilon_{\text{reco}}^{\text{MC}} = 0.998 \pm 0.002(\text{total})$ deviates from unity not until the third decimal place and is compatible with one within errors. This shows the excellent understanding of detector and physics in terms of Z bosons and muon reconstruction. Although, the scale factors in the binned distributions can differ significantly from unity, making them indeed necessary.

Statistical errors are of the order of 0.1% in data and half that big in Monte Carlo. As systematical uncertainties the resolution of combined track momenta, inner detector track momenta and jet momenta as well as the jet energy scale uncertainty were taken into account. Average errors are of the order of half a per mil and strongly depend on the phase space point in the binned distributions. For example for high transverse momentum jets and high jet multiplicities, they reach $\gtrsim 10\%$ due to low statistics in that regions. Systematical uncertainties for the calorimeter tagged muon efficiencies still need to be determined.

The method to determine the muon reconstruction efficiency in the ATLAS detector developed in this thesis has shown to deliver a very pure sample of Z decays and to provide the desired values with errors as low as half a per mil. For future increases of luminosity and therefore a rising number of in-time pile-up collisions in the events, a study of the efficiency dependence with respect to the number of reconstructed vertices could be implemented easily. The question of fake rates was left open and would be a topic for further studies.

A. Appendix

A.1. GoodRunsList Flags

A complete list of demanded flags in the used GoodRunsList recommended by the *ATLAS Z+jets cross-section* group. Even though, not every flag is important for this thesis' analysis:

Table A.1.: List of all demanded GLR flags in this analysis.

Flag	Meaning	
atlsol	solenoid on and current is stable	
atltor	toroid on an current is stable	
trig_muo	muon triggers running	
trig_ele	electron triggers running	
trig_jet	jet triggers running	
trig_met_metcalo	missing E_{T} triggers running	
cp_mu_mmuidcb	no obvious problem observed for muid reconstruction algorithms	
cp_mu_mstaco	no obvious problem observed for staco reconstruction algorithm	
cp_eg_electron_barrel		barrel
cp_eg_electron_endcap	no problem for electron reconstruction in	end-caps
cp_eg_electron_forward		forward region
cp_met	no obvious problem observed for missing E_{T} reconstruction	
cp_btag_life	no obvious problem observed for b-tagging	
cp_tracking	no obvious problem observed for tracking	
cp_jet_jetb		barrel
cp_jet_jetea		end-cap a site
cp_jet_jetec	no problem for jet reconstruction in	end-cap c site
cp_jet_jetfa		forward a site
cp_jet_jetfc		forward c site
pix0	well working first pixel layer (B-layer)	
idvx	vertex finding algorithms running	
idbs	good beam spot data including full beam spot determination and beam spot size	
lumi	sub-detector is in good shape and algorithm gives reliable luminosity values	

A.2. Dataset Names

The dataset names give hints of various circumstances in their production:

- *mc10* shows that the dataset contains Monte Carlo simulations produced in 2010,
- *7TeV* is the center of mass energy in the collisions,
- the *RunID* together with the process name and the *effGen*-tag (eXXX) define unambiguously the generator options and the processes which can be found in the sample,
- the sXXX and rXXX present the options used in the event reconstruction.

Table A.2.: The full names of the used Monte Carlo samples with their sample numbers, reconstruction tags and their weight to correspond to a luminosity of $\mathscr{L} = 34\ \mathrm{pb}^{-1}$.

sample name: "mc10_7TeV." +	weight
106051.PythiaZmumu_1Lepton.AOD.e574_s933_s946_r1831_r1700	0.1042
105200.T1_McAtNlo_Jimmy.AOD.e598_s933_s946_r1831_r1700	3.56×10^{-3}
106021.PythiaWmunu_1Lepton.AOD.e574_s933_s946_r1831_r1700	0.357
106022.PythiaWtaunu_1Lepton.AOD.e574_s933_s946_r1831_r1700	0.268
106052.PythiaZtautau.AOD.e574_s934_s946_r1660_r1700	7.3×10^{-2}
106059.PythiaB_ccmu15X.AOD.e574_s933_s946_r1831_r1700	0.897
108341.st_tchan_munu_McAtNlo_Jimmy.AOD.e598_s933_s946_r1831_r1700	2.05×10^{-3}
108344.st_schan_munu_McAtNlo_Jimmy.AOD.e598_s933_s946_r1831_r1700	1.89×10^{-3}
108346.st_Wt_McAtNlo_Jimmy.AOD.e598_s933_s946_r1831_r1700	1.87×10^{-3}
108405.PythiaB_bbmu15X.AOD.e574_s933_s946_r1831_r1700	0.322

A.3. Efficiencies binned in p_{T} and η

A.3.1. MS and matching Efficiency

MS and matching efficiency as a function of p_{T} and η in data (first) and Monte Carlo (second) and the corresponding scale factors (third).

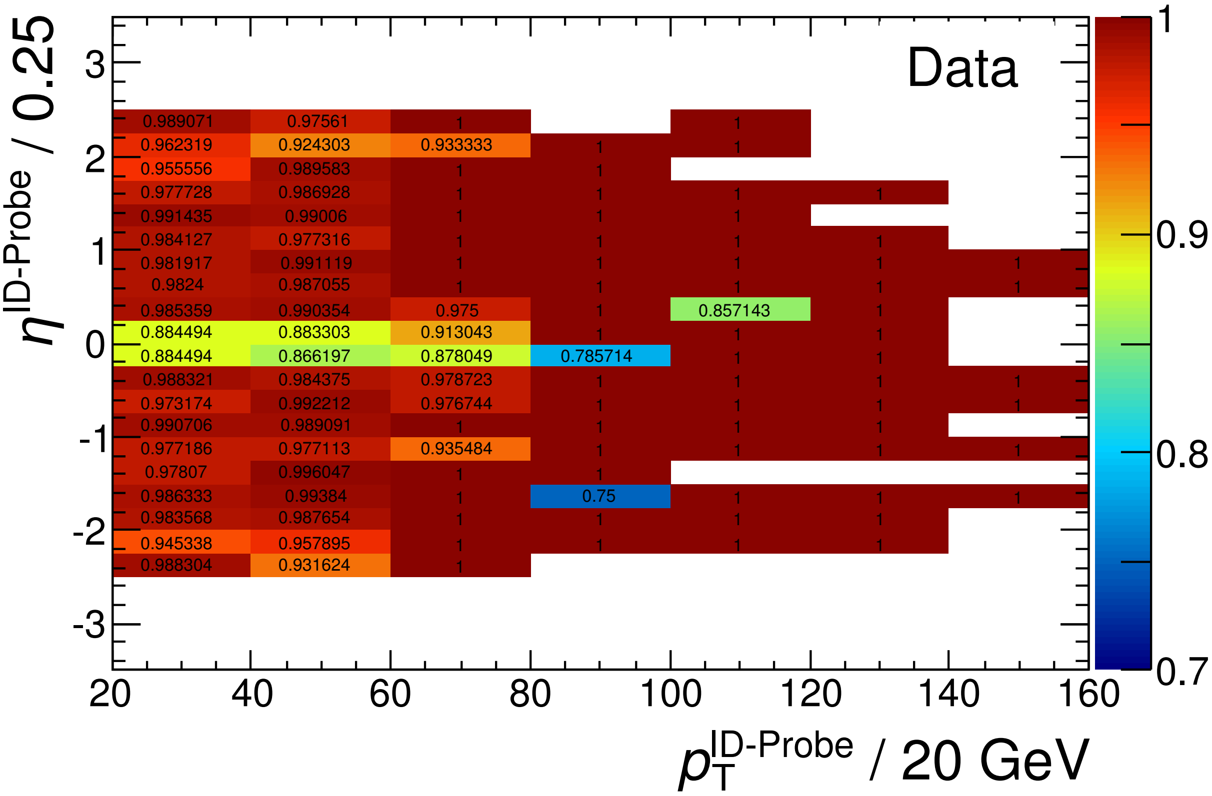

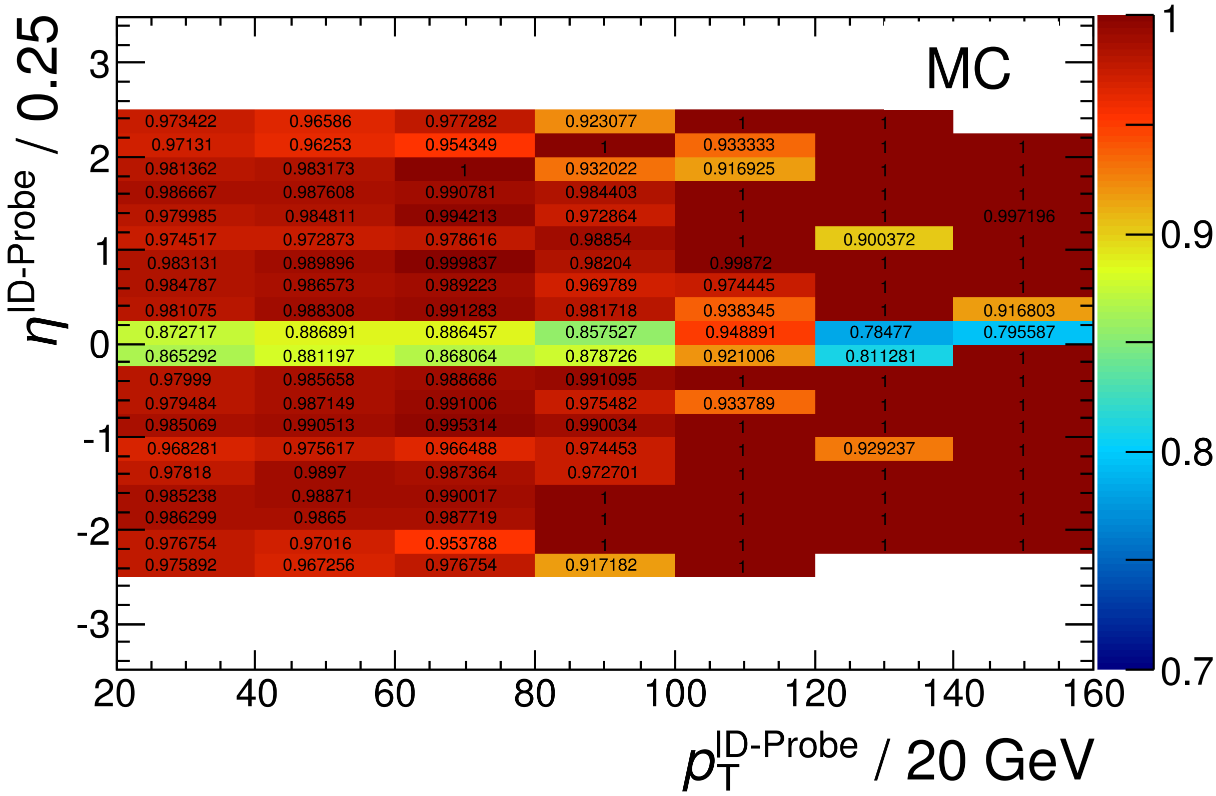
MC
η^ID-Probe / 0.25
p_T^ID-Probe / 20 GeV

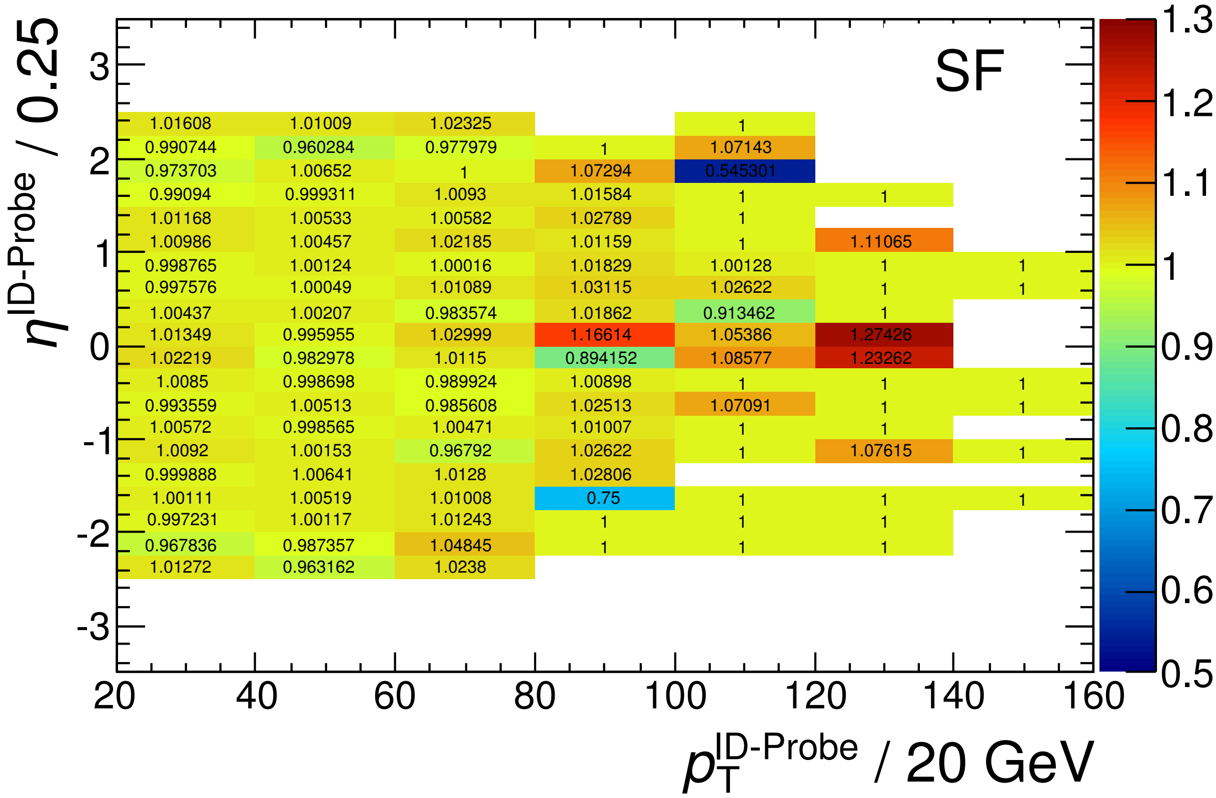
SF
η^ID-Probe / 0.25
p_T^ID-Probe / 20 GeV

A.3.2. ID Efficiency

Inner detector efficiency as a function of p_T and η in data (first) and Monte Carlo (second) and the corresponding scale factors (third):

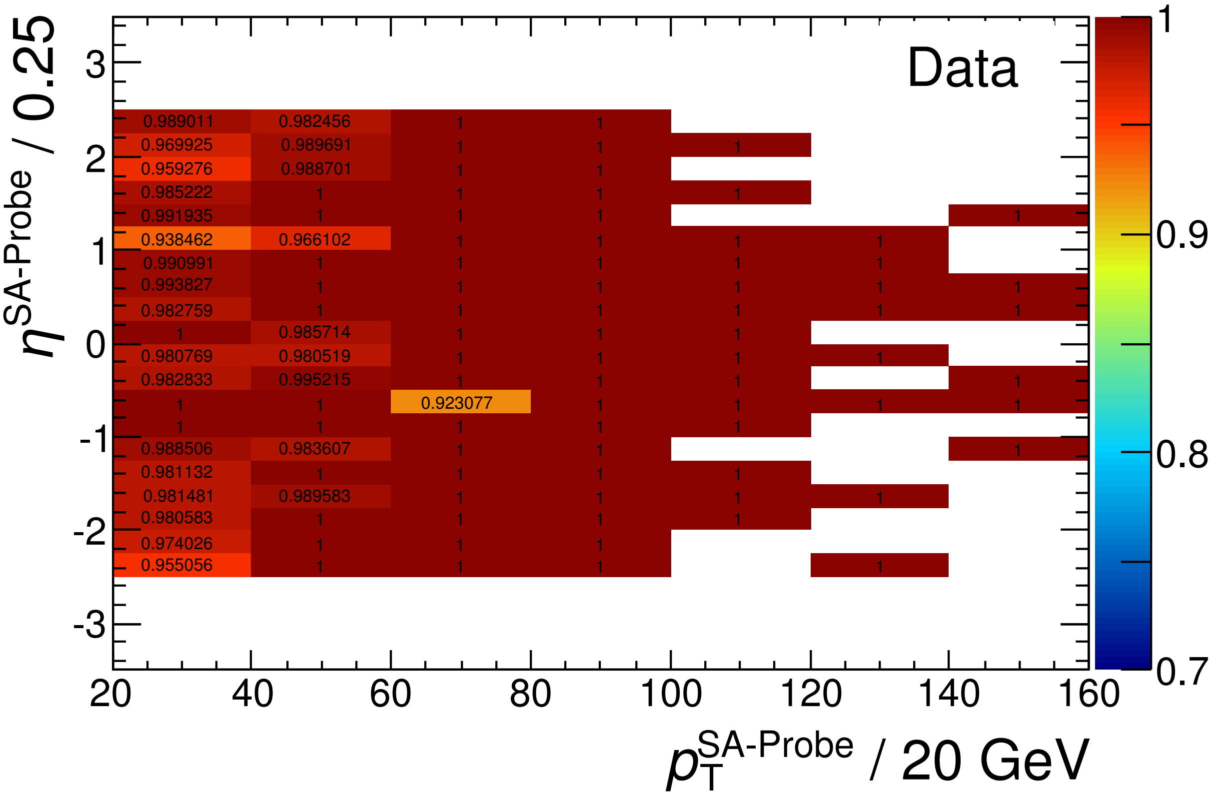

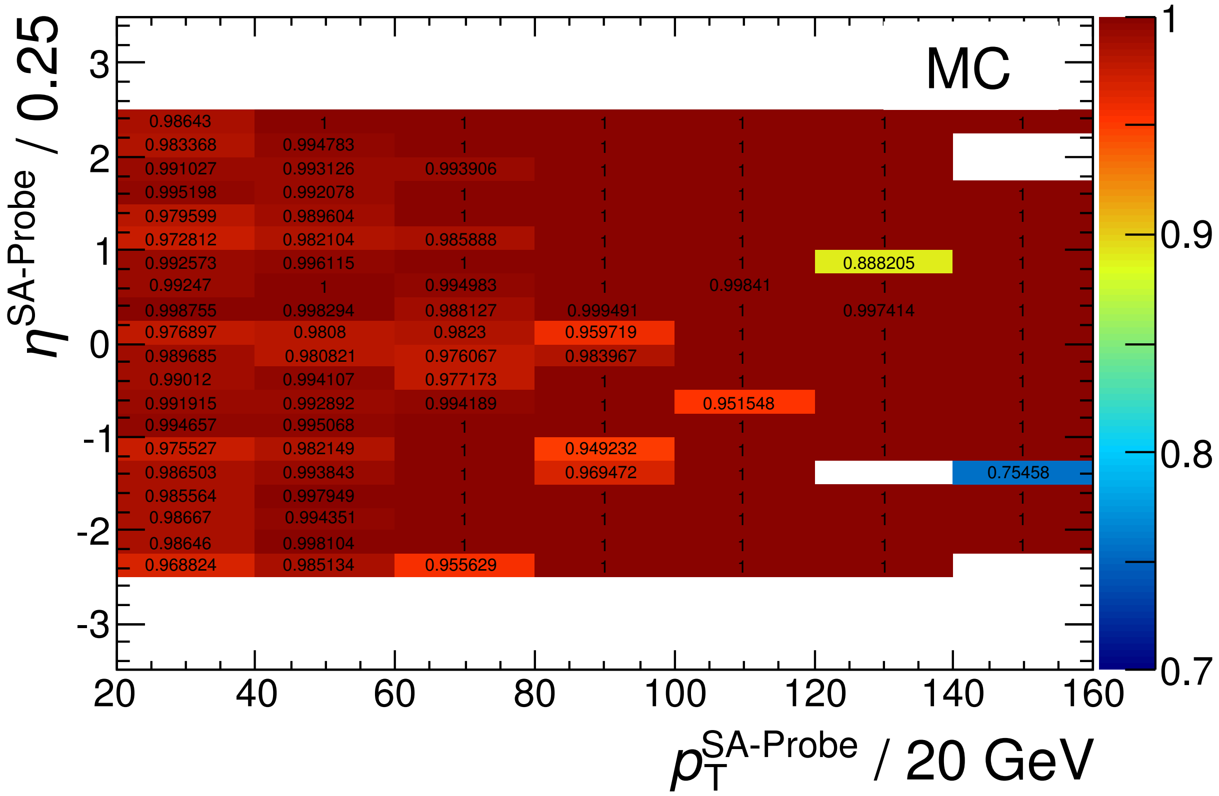
MC
$\eta^{\text{SA-Probe}}$ / 0.25
$p_T^{\text{SA-Probe}}$ / 20 GeV

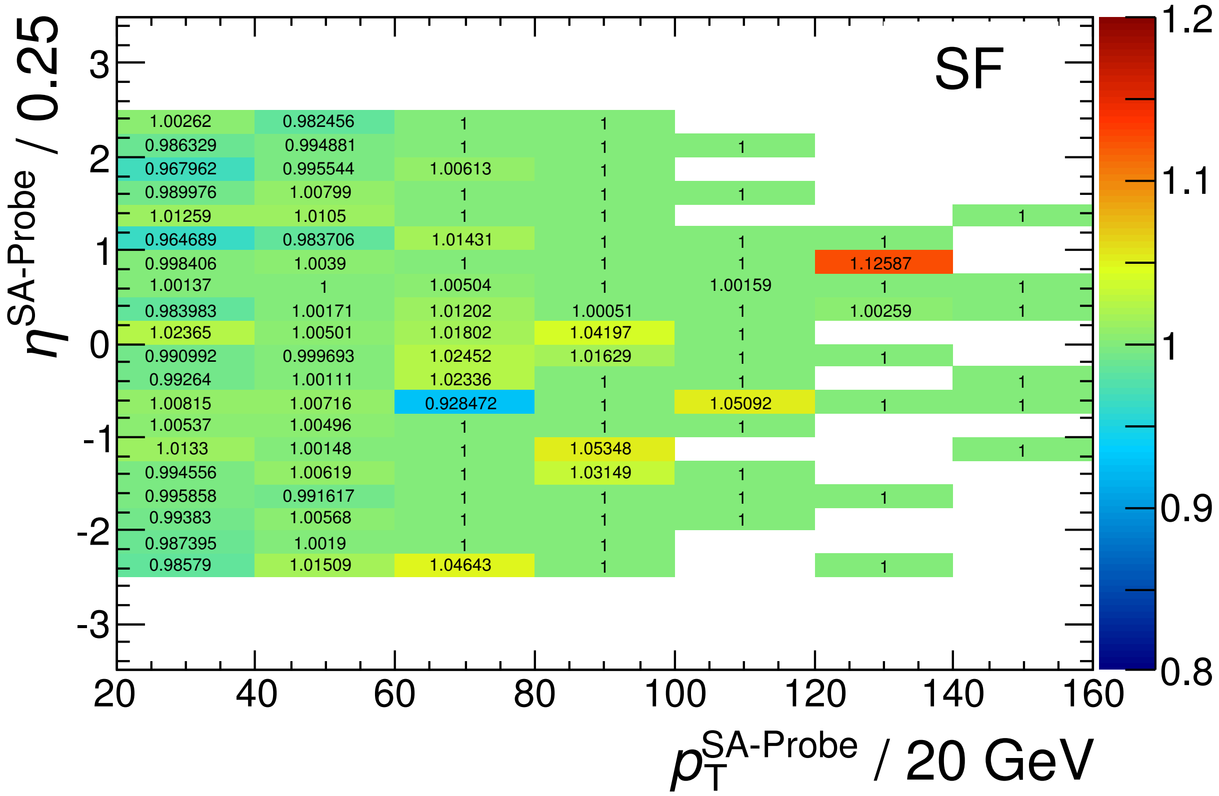
SF
$\eta^{\text{SA-Probe}}$ / 0.25
$p_T^{\text{SA-Probe}}$ / 20 GeV

A.3.3. Calorimeter Efficiency

Calorimeter tagged muon efficiency as a function of p_T and η in data (first) and Monte Carlo (second) and the corresponding scale factors (third).

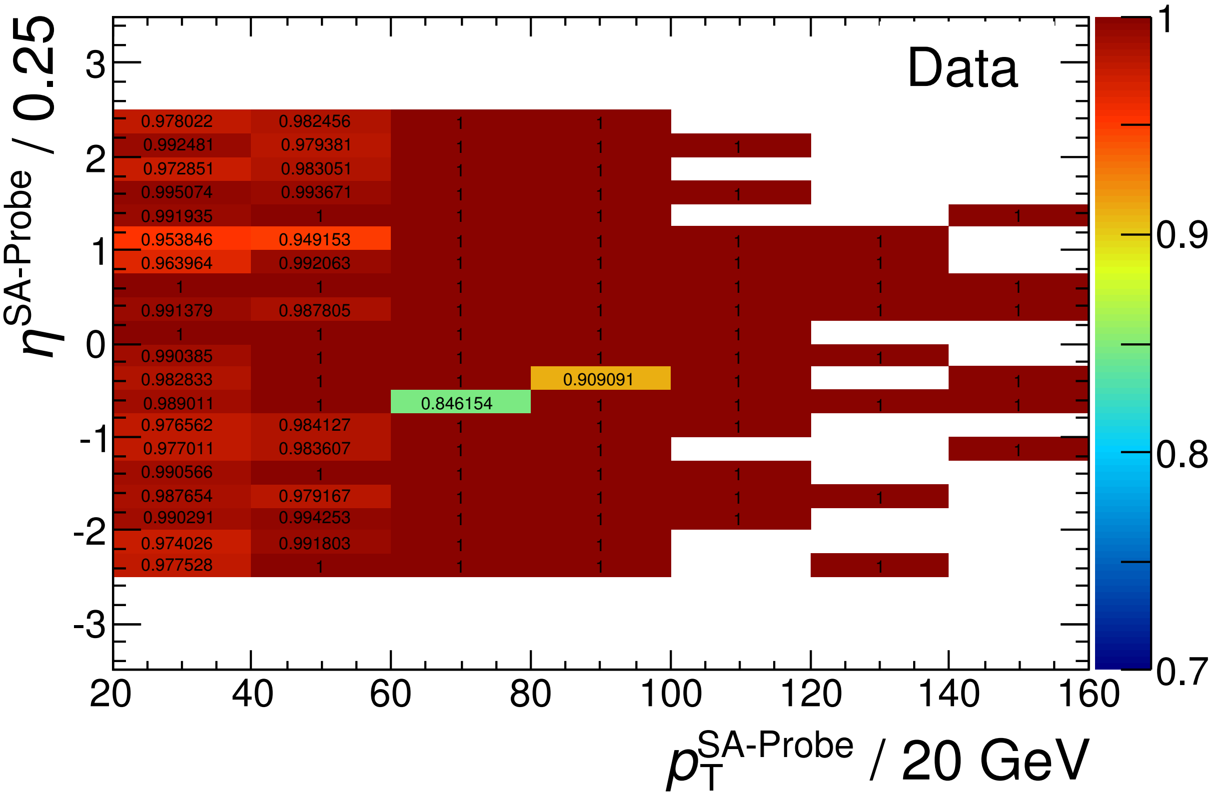

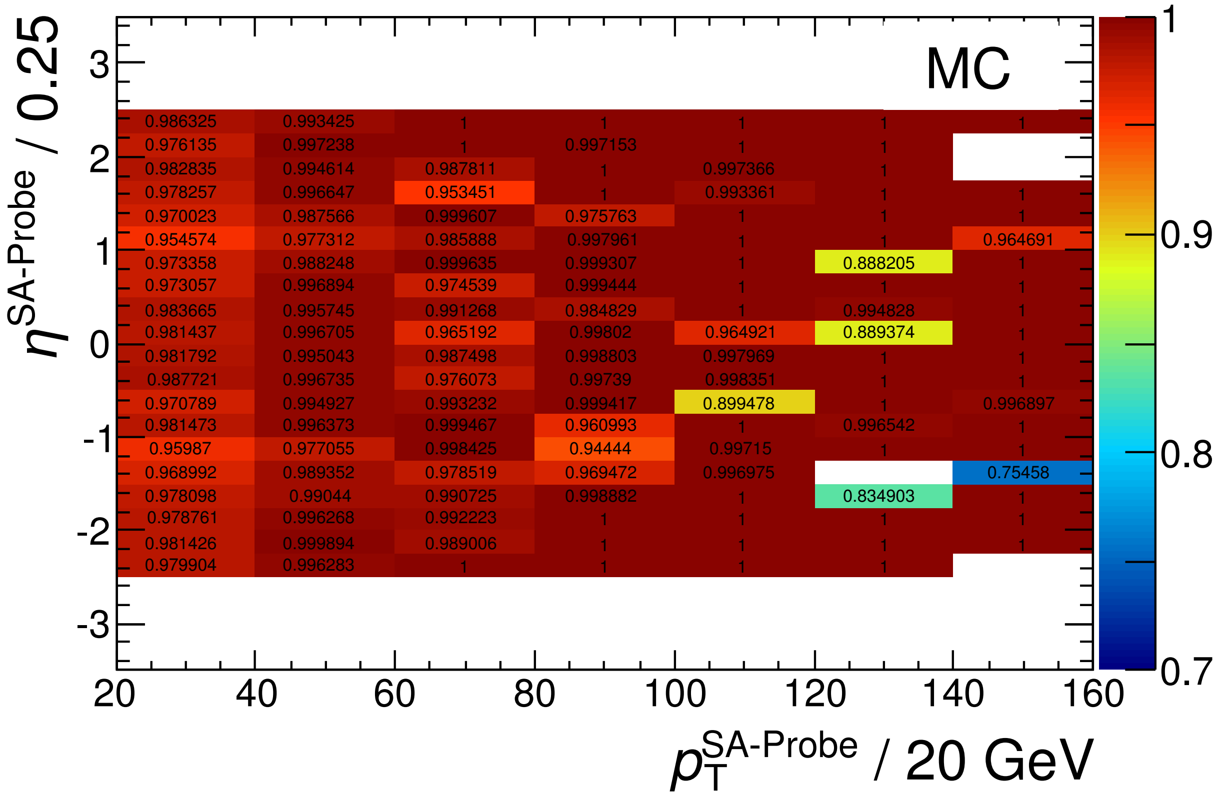
MC
$\eta^{\text{SA-Probe}}$ / 0.25
$p_T^{\text{SA-Probe}}$ / 20 GeV
3 2 1 0 -1 -2 -3
20 40 60 80 100 120 140 160
1 0.9 0.8 0.7
0.986325 0.993425 1 1 1 1 1
0.976135 0.997238 1 0.997153 1 1
0.982835 0.994614 0.987811 1 0.997366 1
0.978257 0.996647 0.953451 1 0.993361 1 1
0.970023 0.987566 0.999607 0.975763 1 1 1
0.954574 0.977312 0.985888 0.997961 1 1 0.964691
0.973358 0.988248 0.999635 0.999307 1 0.888205 1
0.973057 0.996894 0.974539 0.999444 1 1 1
0.983665 0.995745 0.991268 0.984829 1 0.994828 1
0.981437 0.996705 0.965192 0.99802 0.964921 0.889374 1
0.981792 0.995043 0.987498 0.998803 0.997969 1 1
0.987721 0.996735 0.976073 0.99739 0.998351 1 1
0.970789 0.994927 0.993232 0.999417 0.899478 1 0.996897
0.981473 0.996373 0.999467 0.960993 1 0.996542 1
0.95987 0.977055 0.998425 0.94444 0.99715 1 1
0.968992 0.989352 0.978519 0.969472 0.996975 0.75458
0.978098 0.99044 0.990725 0.998882 1 0.834903 1
0.978761 0.996268 0.992223 1 1 1 1
0.981426 0.999894 0.989006 1 1 1 1
0.979904 0.996283 1 1 1 1

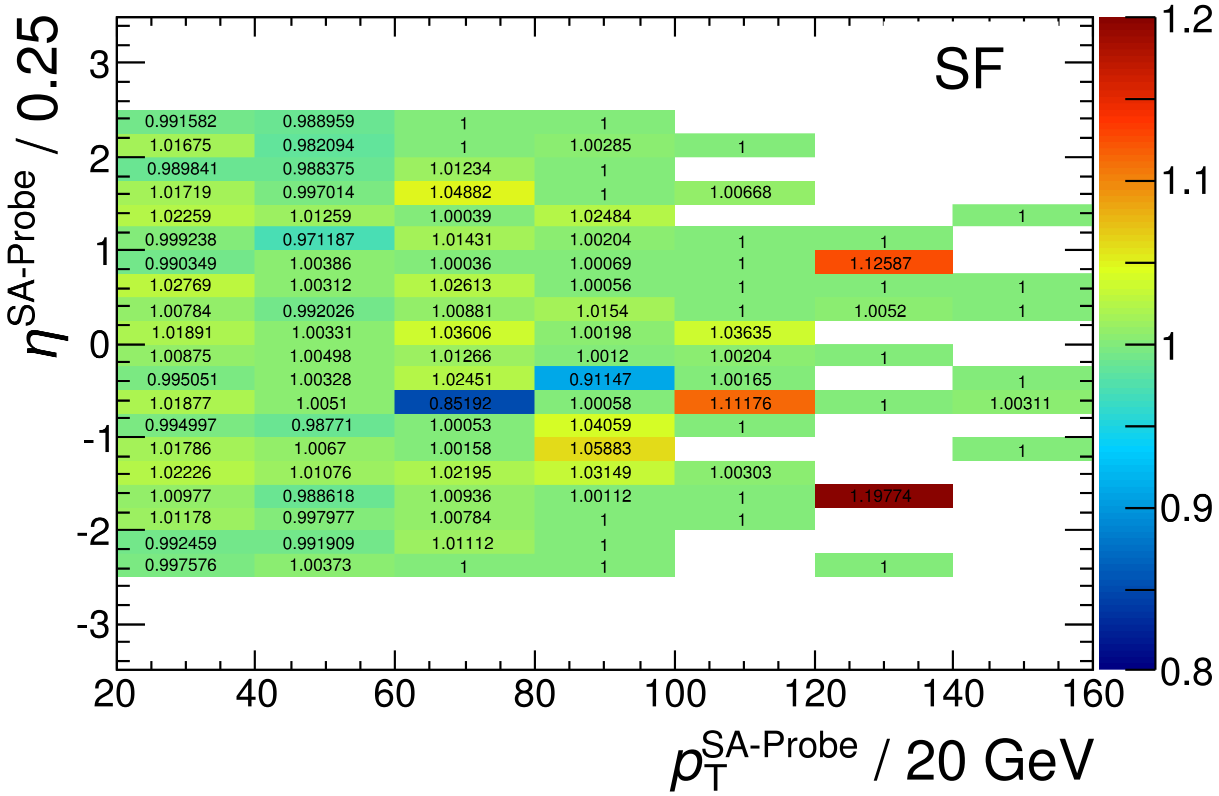
SF
$\eta^{\text{SA-Probe}}$ / 0.25
$p_T^{\text{SA-Probe}}$ / 20 GeV
3 2 1 0 -1 -2 -3
20 40 60 80 100 120 140 160
1.2 1.1 1 0.9 0.8
0.991582 0.988959 1 1
1.01675 0.982094 1 1.00285 1
0.989841 0.988375 1.01234 1
1.01719 0.997014 1.04882 1 1.00668
1.02259 1.01259 1.00039 1.02484 1
0.999238 0.971187 1.01431 1.00204 1 1
0.990349 1.00386 1.00036 1.00069 1 1.12587
1.02769 1.00312 1.02613 1.00056 1 1 1
1.00784 0.992026 1.00881 1.0154 1 1.0052 1
1.01891 1.00331 1.03606 1.00198 1.03635
1.00875 1.00498 1.01266 1.0012 1.00204 1
0.995051 1.00328 1.02451 0.91147 1.00165 1
1.01877 1.0051 0.85192 1.00058 1.11176 1 1.00311
0.994997 0.98771 1.00053 1.04059 1
1.01786 1.0067 1.00158 1.05883 1
1.02226 1.01076 1.02195 1.03149 1.00303
1.00977 0.988618 1.00936 1.00112 1 1.19774
1.01178 0.997977 1.00784 1 1
0.992459 0.991909 1.01112 1
0.997576 1.00373 1 1 1

A.4. Efficiencies and Scale Factors

p_{T}/GeV Bins	$(\varepsilon_{\mathrm{MS}}^{\mathrm{Data}} \times \varepsilon_{\mathrm{match}}^{\mathrm{Data}})$ in %	$(\varepsilon_{\mathrm{MS}}^{\mathrm{MC}} \times \varepsilon_{\mathrm{match}}^{\mathrm{MC}})$ in %	Scale Factors
20–25	$96.14^{+0.53}_{-0.58}$(stat)	$96.54^{+0.17}_{-0.17}$(stat) $\pm$ 0.12(syst)	$0.9959^{+0.0059}_{-0.0063}$(total)
25–30	$96.8\ ^{+0.39}_{-0.42}$(stat)	$96\ ^{+0.15}_{-0.15}$(stat) $\pm$ 0.19(syst)	$1.0083^{+0.0048}_{-0.0051}$(total)
30–35	$96.48^{+0.34}_{-0.36}$(stat)	$96.49^{+0.11}_{-0.12}$(stat) $\pm$ 0.02(syst)	$0.9999^{+0.0037}_{-0.004}$(total)
35–40	$97.08^{+0.26}_{-0.28}$(stat)	$96.75^{+0.09}_{-0.09}$(stat) $\pm$ 0.13(syst)	$1.0035^{+0.0032}_{-0.0034}$(total)
40–60	$97.07^{+0.17}_{-0.18}$(stat)	$97.15^{+0.05}_{-0.06}$(stat) $\pm$ 0.07(syst)	$0.9993^{+0.002}_{-0.0020}$(total)
60–100	$97.56^{+0.50}_{-0.58}$(stat)	$97.05^{+0.18}_{-0.19}$(stat) $\pm$ 0.42(syst)	$1.0053^{+0.0071}_{-0.0077}$(total)

ϕ Bins	$(\varepsilon_{\mathrm{MS}}^{\mathrm{Data}} \times \varepsilon_{\mathrm{match}}^{\mathrm{Data}})$ in %	$(\varepsilon_{\mathrm{MS}}^{\mathrm{MC}} \times \varepsilon_{\mathrm{match}}^{\mathrm{MC}})$ in %	Scale Factors
-3.5 – -2.5	$97.27^{+0.35}_{-0.38}$(stat)	$96.86^{+0.12}_{-0.13}$(stat) $\pm$ 0.02(syst)	$1.0042^{+0.0038}_{-0.0041}$(total)
-2.5 – -1.5	$96.17^{+0.33}_{-0.35}$(stat)	$96.17^{+0.11}_{-0.11}$(stat) $\pm$ 0.13(syst)	$1.0000^{+0.0038}_{-0.0040}$(total)
-1.5 – -0.5	$96.63^{+0.31}_{-0.33}$(stat)	$96.70^{+0.10}_{-0.10}$(stat) $\pm$ 0.15(syst)	$0.9993^{+0.0038}_{-0.0039}$(total)
-0.5 – 0.5	$97.66^{+0.26}_{-0.28}$(stat)	$97.22^{+0.09}_{-0.09}$(stat) $\pm$ 0.12(syst)	$1.0045^{+0.0031}_{-0.0033}$(total)
0.5 – 1.5	$97.4\ ^{+0.28}_{-0.3}$(stat)	$97.52^{+0.09}_{-0.09}$(stat) $\pm$ 0.15(syst)	$0.9988^{+0.0034}_{-0.0036}$(total)
1.5 – 2.5	$96.51^{+0.32}_{-0.34}$(stat)	$96.51^{+0.10}_{-0.11}$(stat) $\pm$ 0.11(syst)	$0.9999^{+0.0037}_{-0.0039}$(total)
2.5 – 3.5	$96.99^{+0.35}_{-0.38}$(stat)	$96.93^{+0.12}_{-0.12}$(stat) $\pm$ 0.14(syst)	$1.0006^{+0.0041}_{-0.0044}$(total)

ΔR Bins	$(\varepsilon_{\mathrm{MS}}^{\mathrm{Data}} \times \varepsilon_{\mathrm{match}}^{\mathrm{Data}})$ in %	$(\varepsilon_{\mathrm{MS}}^{\mathrm{MC}} \times \varepsilon_{\mathrm{match}}^{\mathrm{MC}})$ in %	Scale Factors
0.5–1.0	$96.02^{+0.39}_{-0.41}$(stat)	$96.62^{+0.11}_{-0.11}$(stat) $\pm$ 0.53(syst)	$0.9938^{+0.0069}_{-0.0071}$(total)
1.0–1.5	$97.50^{+0.26}_{-0.28}$(stat)	$97.13^{+0.09}_{-0.09}$(stat) $\pm$ 0.45(syst)	$1.0038^{+0.0054}_{-0.0055}$(total)
1.5–2.0	$97.06^{+0.27}_{-0.29}$(stat)	$97.21^{+0.09}_{-0.09}$(stat) $\pm$ 0.67(syst)	$0.9985^{+0.0075}_{-0.0075}$(total)
2.0–2.5	$97.29^{+0.29}_{-0.31}$(stat)	$97.11^{+0.1}_{-0.1}$ (stat) $\pm$ 0.47(syst)	$1.0018^{+0.0057}_{-0.0058}$(total)
2.5–3.0	$96.06^{+0.39}_{-0.42}$(stat)	$95.78^{+0.13}_{-0.14}$(stat) $\pm$ 2.05(syst)	$1.0029^{+0.0218}_{-0.0219}$(total)
3.0–3.5	$96.00^{+0.54}_{-0.59}$(stat)	$96.07^{+0.18}_{-0.18}$(stat) $\pm$ 0.93(syst)	$0.9993^{+0.0113}_{-0.0116}$(total)
3.5–4.0	$97.20^{+0.73}_{-0.88}$(stat)	$96.1\ ^{+0.32}_{-0.33}$(stat) $\pm$ 1.2 (syst)	$1.0115^{+0.0150}_{-0.0158}$(total)
4.0–4.5	$97.70^{+0.97}_{-1.35}$(stat)	$97.54^{+0.38}_{-0.42}$(stat) $\pm$ 1.04(syst)	$1.0017^{+0.0152}_{-0.0179}$(total)
4.5–5.0	$95.19^{+1.83}_{-2.41}$(stat)	$96.76^{+0.56}_{-0.63}$(stat) $\pm$ 0.83(syst)	$0.9838^{+0.0215}_{-0.0266}$(total)

Table A.3.: Muon spectrometer and matching efficiency with statistical and systematical errors and scale factors in data and Monte Carlo in bins of p_{T}, ϕ and ΔR.

# of Jets	$(\varepsilon_{\text{MS}}^{\text{Data}} \times \varepsilon_{\text{match}}^{\text{Data}})$ in %	$(\varepsilon_{\text{MS}}^{\text{MC}} \times \varepsilon_{\text{match}}^{\text{MC}})$ in %	Scale Factors
0	$97.61^{+0.25}_{-0.27}(\text{stat})$	$97.29^{+0.10}_{-0.11}(\text{stat}) \pm 0.62(\text{syst})$	$1.0032^{+0.007}_{-0.0070}(\text{total})$
1	$96.61^{+0.33}_{-0.36}(\text{stat})$	$96.73^{+0.12}_{-0.12}(\text{stat}) \pm 0.25(\text{syst})$	$0.9986^{+0.0045}_{-0.0047}(\text{total})$
2	$96.86^{+0.38}_{-0.41}(\text{stat})$	$96.91^{+0.14}_{-0.14}(\text{stat}) \pm 0.43(\text{syst})$	$0.9995^{+0.0061}_{-0.0063}(\text{total})$
3	$96.86^{+0.47}_{-0.51}(\text{stat})$	$96.62^{+0.17}_{-0.18}(\text{stat}) \pm 0.54(\text{syst})$	$1.0025^{+0.0076}_{-0.0079}(\text{total})$
4	$96.94^{+0.57}_{-0.64}(\text{stat})$	$96.63^{+0.2}_{-0.20}(\text{stat}) \pm 5.13(\text{syst})$	$1.0032^{+0.0534}_{-0.0355}(\text{total})$

$p_{\text{T}}^{\text{Jet}}$/GeV Bins	$(\varepsilon_{\text{MS}}^{\text{Data}} \times \varepsilon_{\text{match}}^{\text{Data}})$ in %	$(\varepsilon_{\text{MS}}^{\text{MC}} \times \varepsilon_{\text{match}}^{\text{MC}})$ in %	Scale Factors
20–30	$96.71^{+0.36}_{-0.39}(\text{stat})$	$96.68^{+0.11}_{-0.12}(\text{stat}) \pm 0.1\ (\text{syst})$	$1.0003^{+0.0041}_{-0.0044}(\text{total})$
30–40	$96.34^{+0.55}_{-0.61}(\text{stat})$	$96.66^{+0.17}_{-0.17}(\text{stat}) \pm 0.43(\text{syst})$	$0.9967^{+0.0074}_{-0.0078}(\text{total})$
40–50	$98.01^{+0.50}_{-0.60}(\text{stat})$	$96.94^{+0.21}_{-0.22}(\text{stat}) \pm 0.68(\text{syst})$	$1.0111^{+0.0090}_{-0.0096}(\text{total})$
50–70	$96.34^{+0.73}_{-0.84}(\text{stat})$	$97.02^{+0.21}_{-0.22}(\text{stat}) \pm 0.38(\text{syst})$	$0.9930^{+0.0087}_{-0.0097}(\text{total})$
70–90	$95.89^{+1.06}_{-1.27}(\text{stat})$	$96.60^{+0.33}_{-0.35}(\text{stat}) \pm 0.38(\text{syst})$	$0.9926^{+0.0121}_{-0.0141}(\text{total})$
90–120	$98.06^{+0.82}_{-1.14}(\text{stat})$	$97.31^{+0.39}_{-0.43}(\text{stat}) \pm 1.09(\text{syst})$	$1.0077^{+0.0147}_{-0.0168}(\text{total})$
120–160	$96.25^{+1.77}_{-2.56}(\text{stat})$	$97.43^{+0.53}_{-0.61}(\text{stat}) \pm 1.09(\text{syst})$	$0.9879^{+0.0221}_{-0.0288}(\text{total})$
160–200	$89.47^{+4.27}_{-5.63}(\text{stat})$	$95.47^{+1.17}_{-1.4}(\text{stat}) \pm 1.09(\text{syst})$	$0.9372^{+0.0458}_{-0.0577}(\text{total})$

Table A.4.: Muon spectrometer and matching efficiency with statistical and systematical errors and scale factors in data and Monte Carlo in bins of number of jets and p_{T} of the leading jet.

η Bins	$(\varepsilon_{\text{MS}}^{\text{Data}} \times \varepsilon_{\text{match}}^{\text{Data}})$ in %	$(\varepsilon_{\text{MS}}^{\text{MC}} \times \varepsilon_{\text{match}}^{\text{MC}})$ in %	Scale Factors
-2.5 – -2.3	$96.14^{+1.20}_{-1.50}$(stat)	$97.26^{+0.36}_{-0.39}$(stat) $\pm$ 0.35(syst)	$0.9884^{+0.0133}_{-0.0161}$(total)
-2.3 – -2.1	$95.95^{+0.87}_{-1.01}$(stat)	$97.25^{+0.23}_{-0.24}$(stat) $\pm$ 0.43(syst)	$0.9866^{+0.0102}_{-0.0114}$(total)
-2.1 – -1.9	$97.03^{+0.66}_{-0.77}$(stat)	$97.71^{+0.19}_{-0.2}$(stat) $\pm$ 0.17(syst)	$0.993^{+0.0072}_{-0.0082}$(total)
-1.9 – -1.7	$98.82^{+0.37}_{-0.47}$(stat)	$98.96^{+0.12}_{-0.13}$(stat) $\pm$ 0.07(syst)	$0.9986^{+0.0040}_{-0.0049}$(total)
-1.7 – -1.5	$98.55^{+0.4}_{-0.48}$(stat)	$98.75^{+0.13}_{-0.14}$(stat) $\pm$ 0.01(syst)	$0.9979^{+0.0042}_{-0.0050}$(total)
-1.5 – -1.3	$98.64^{+0.37}_{-0.45}$(stat)	$98.39^{+0.14}_{-0.15}$(stat) $\pm$ 0.01(syst)	$1.0026^{+0.0041}_{-0.0048}$(total)
-1.3 – -1.1	$96.91^{+0.55}_{-0.62}$(stat)	$96.88^{+0.17}_{-0.19}$(stat) $\pm$ 0.38(syst)	$1.0003^{+0.0072}_{-0.0078}$(total)
-1.1 – -0.9	$99.14^{+0.27}_{-0.34}$(stat)	$98.75^{+0.12}_{-0.12}$(stat) $\pm$ 0.37(syst)	$1.004^{+0.0048}_{-0.0053}$(total)
-0.9 – -0.7	$98.97^{+0.29}_{-0.36}$(stat)	$98.78^{+0.11}_{-0.12}$(stat) $\pm$ 0.02(syst)	$1.0019^{+0.0032}_{-0.0039}$(total)
-0.7 – -0.5	$98.3^{+0.36}_{-0.42}$(stat)	$98.22^{+0.13}_{-0.14}$(stat) $\pm$ 0.46(syst)	$1.0008^{+0.0061}_{-0.0064}$(total)
-0.5 – -0.3	$98.38^{+0.35}_{-0.41}$(stat)	$98.28^{+0.13}_{-0.13}$(stat) $\pm$ 0.25(syst)	$1.0011^{+0.0046}_{-0.0050}$(total)
-0.3 – -0.1	$98.99^{+0.28}_{-0.34}$(stat)	$98.19^{+0.13}_{-0.13}$(stat) $\pm$ 0.20(syst)	$1.0081^{+0.0038}_{-0.0042}$(total)
-0.1 – 0.1	$69.77^{+1.50}_{-1.53}$(stat)	$68.99^{+0.49}_{-0.49}$(stat) $\pm$ 0.61(syst)	$1.0114^{+0.0248}_{-0.0252}$(total)
0.1 – 0.3	$98.43^{+0.35}_{-0.41}$(stat)	$98.19^{+0.13}_{-0.13}$(stat) $\pm$ 0.01(syst)	$1.0024^{+0.0038}_{-0.0044}$(total)
0.3 – 0.5	$98.62^{+0.33}_{-0.39}$(stat)	$98.49^{+0.12}_{-0.12}$(stat) $\pm$ 0.03(syst)	$1.0014^{+0.0036}_{-0.0041}$(total)
0.5 – 0.7	$98.49^{+0.35}_{-0.41}$(stat)	$98.5^{+0.12}_{-0.13}$(stat) $\pm$ 0.08(syst)	$0.9997^{+0.0038}_{-0.0044}$(total)
0.7 – 0.9	$98.66^{+0.34}_{-0.41}$(stat)	$98.71^{+0.11}_{-0.12}$(stat) $\pm$ 0.1 (syst)	$0.9994^{+0.0038}_{-0.0044}$(total)
0.9 – 1.1	$99.24^{+0.25}_{-0.33}$(stat)	$98.88^{+0.11}_{-0.12}$(stat) $\pm$ 0.08(syst)	$1.0037^{+0.003}_{-0.0036}$(total)
1.1 – 1.3	$97.47^{+0.51}_{-0.59}$(stat)	$96.49^{+0.2}_{-0.21}$(stat) $\pm$ 0.04(syst)	$1.0102^{+0.0058}_{-0.0065}$(total)
1.3 – 1.5	$99.25^{+0.27}_{-0.35}$(stat)	$98.65^{+0.13}_{-0.14}$(stat) $\pm$ 0.05(syst)	$1.0060^{+0.0031}_{-0.0039}$(total)
1.5 – 1.7	$98.18^{+0.44}_{-0.53}$(stat)	$98.78^{+0.12}_{-0.13}$(stat) $\pm$ 0.12(syst)	$0.9939^{+0.0048}_{-0.0056}$(total)
1.7 – 1.9	$98.10^{+0.48}_{-0.57}$(stat)	$98.34^{+0.15}_{-0.16}$(stat) $\pm$ 0.2 (syst)	$0.9976^{+0.0055}_{-0.0063}$(total)
1.9 – 2.1	$95.81^{+0.80}_{-0.91}$(stat)	$97.00^{+0.22}_{-0.23}$(stat) $\pm$ 0.23(syst)	$0.9877^{+0.0088}_{-0.0099}$(total)
2.1 – 2.3	$95.86^{+0.85}_{-0.97}$(stat)	$97.47^{+0.22}_{-0.23}$(stat) $\pm$ 0.65(syst)	$0.9834^{+0.0111}_{-0.0121}$(total)
2.3 – 2.5	$97.31^{+1.03}_{-1.38}$(stat)	$96.59^{+0.40}_{-0.44}$(stat) $\pm$ 0.04(syst)	$1.0075^{+0.0117}_{-0.015}$(total)

Table A.5.: Muon spectrometer and matching efficiency with statistical and systematical errors and scale factors in data and Monte Carlo in bins of η.

$p_{\mathrm{T}}/\mathrm{GeV}$ Bins	$\varepsilon_{\mathrm{ID}}^{\mathrm{Data}}$ in %	$\varepsilon_{\mathrm{ID}}^{\mathrm{MC}}$ in %	Scale Factors
20–25	$92.69^{+1.18}_{-1.31}$(stat)	$95.07^{+0.36}_{-0.38}$(stat) $\pm$ 0.64(syst)	$0.9750^{+0.0144}_{-0.0155}$(total)
25–30	$99.4\ ^{+0.26}_{-0.36}$(stat)	$99.25^{+0.11}_{-0.12}$(stat) $\pm$ 0.07(syst)	$1.0015^{+0.003}_{-0.0039}$(total)
30–35	$99.17^{+0.28}_{-0.35}$(stat)	$99.26^{+0.09}_{-0.1}$(stat) $\pm$ 0.07(syst)	$0.9991^{+0.0030}_{-0.0037}$(total)
35–40	$99.03^{+0.26}_{-0.32}$(stat)	$99.37^{+0.07}_{-0.08}$(stat) $\pm$ 0.02(syst)	$0.9967^{+0.0028}_{-0.0033}$(total)
40–60	$99.43^{+0.14}_{-0.17}$(stat)	$99.21^{+0.05}_{-0.05}$(stat) $\pm$ 0.03(syst)	$1.0022^{+0.0015}_{-0.0018}$(total)
60–100	$99.70^{+0.22}_{-0.44}$(stat)	$99.14^{+0.15}_{-0.16}$(stat) $\pm$ 0.09(syst)	$1.0057^{+0.0029}_{-0.0048}$(total)

ϕ Bins	$\varepsilon_{\mathrm{ID}}^{\mathrm{Data}}$ in %	$\varepsilon_{\mathrm{ID}}^{\mathrm{MC}}$ in %	Scale Factors
-3.5 – -2.5	$98.1\ ^{+0.5}_{-0.6}$ (stat)	$99.13^{+0.11}_{-0.12}$(stat) $\pm$ 0.15(syst)	$0.9896^{+0.0053}_{-0.0063}$(total)
-2.5 – -1.5	$98.98^{+0.29}_{-0.36}$(stat)	$98.98^{+0.1}_{-0.11}$(stat) $\pm$ 0.12(syst)	$1.0000^{+0.0033}_{-0.0039}$(total)
-1.5 – -0.5	$99.33^{+0.24}_{-0.32}$(stat)	$99.24^{+0.09}_{-0.09}$(stat) $\pm$ 0.05(syst)	$1.0008^{+0.0027}_{-0.0034}$(total)
-0.5 – 0.5	$99.06^{+0.28}_{-0.35}$(stat)	$99.09^{+0.09}_{-0.1}$(stat) $\pm$ 0.13(syst)	$0.9998^{+0.0033}_{-0.0039}$(total)
0.5 – 1.5	$98.10^{+0.42}_{-0.49}$(stat)	$98.71^{+0.11}_{-0.12}$(stat) $\pm$ 0.19(syst)	$0.9939^{+0.0048}_{-0.0055}$(total)
1.5 – 2.5	$98.82^{+0.32}_{-0.39}$(stat)	$99.12^{+0.09}_{-0.1}$(stat) $\pm$ 0.04(syst)	$0.997\ ^{+0.0034}_{-0.0041}$(total)
2.5 – 3.5	$99.40^{+0.26}_{-0.36}$(stat)	$98.89^{+0.13}_{-0.14}$(stat) $\pm$ 0.07(syst)	$1.0052^{+0.0030}_{-0.0039}$(total)

ΔR Bins	$\varepsilon_{\mathrm{ID}}^{\mathrm{Data}}$ in %	$\varepsilon_{\mathrm{ID}}^{\mathrm{MC}}$ in %	Scale Factors
0.5–1.0	$98.99^{+0.32}_{-0.40}$(stat)	$98.82^{+0.11}_{-0.12}$(stat) $\pm$ 0.16(syst)	$1.0017^{+0.0038}_{-0.0045}$(total)
1.0–1.5	$98.76^{+0.30}_{-0.36}$(stat)	$99.00^{+0.09}_{-0.09}$(stat) $\pm$ 0.13(syst)	$0.9975^{+0.0035}_{-0.004}$(total)
1.5–2.0	$98.98^{+0.29}_{-0.36}$(stat)	$99.16^{+0.09}_{-0.09}$(stat) $\pm$ 0.14(syst)	$0.9982^{+0.0034}_{-0.004}$(total)
2.0–2.5	$98.82^{+0.33}_{-0.41}$(stat)	$99.01^{+0.1}_{-0.11}$(stat) $\pm$ 0.08(syst)	$0.9981^{+0.0036}_{-0.0044}$(total)
2.5–3.0	$98.66^{+0.38}_{-0.47}$(stat)	$98.96^{+0.11}_{-0.12}$(stat) $\pm$ 0.10(syst)	$0.9970^{+0.0041}_{-0.005}$(total)
3.0–3.5	$98.35^{+0.55}_{-0.71}$(stat)	$99.22^{+0.13}_{-0.14}$(stat) $\pm$ 0.06(syst)	$0.9912^{+0.0057}_{-0.0072}$(total)
3.5–4.0	$100.0^{+0.00}_{-0.95}$(stat)	$99.23^{+0.23}_{-0.29}$(stat) $\pm$ 0.17(syst)	$1.0078^{+0.0034}_{-0.0101}$(total)
4.0–4.5	$98.00^{+1.44}_{-2.86}$(stat)	$98.62^{+0.49}_{-0.64}$(stat) $\pm$ 0.34(syst)	$0.9937^{+0.0163}_{-0.0295}$(total)
4.5–5.0	$100.0^{+0.00}_{-4.67}$(stat)	$99.67^{+0.24}_{-0.49}$(stat) $\pm$ 0.75(syst)	$1.0033^{+0.0090}_{-0.0472}$(total)

Table A.6.: Inner detector efficiency with statistical and systematical errors and scale factors in data and Monte Carlo in bins of p_{T}, ϕ and ΔR.

# of Jets	$\varepsilon_{\mathrm{ID}}^{\mathrm{Data}}$ in %	$\varepsilon_{\mathrm{ID}}^{\mathrm{MC}}$ in %	Scale Factors
0	$98.93^{+0.32}_{-0.4}(\mathrm{stat})$	$99.1\ ^{+0.11}_{-0.12}(\mathrm{stat}) \pm 0.06(\mathrm{syst})$	$0.9983^{+0.0035}_{-0.0042}(\mathrm{total})$
1	$98.47^{+0.40}_{-0.48}(\mathrm{stat})$	$99.1\ ^{+0.11}_{-0.12}(\mathrm{stat}) \pm 0.06(\mathrm{syst})$	$0.9936^{+0.0042}_{-0.0050}(\mathrm{total})$
2	$98.29^{+0.46}_{-0.57}(\mathrm{stat})$	$99.15^{+0.12}_{-0.14}(\mathrm{stat}) \pm 0.16(\mathrm{syst})$	$0.9913^{+0.0051}_{-0.0060}(\mathrm{total})$
3	$99.02^{+0.41}_{-0.58}(\mathrm{stat})$	$99.08^{+0.15}_{-0.17}(\mathrm{stat}) \pm 0.11(\mathrm{syst})$	$0.9994^{+0.0046}_{-0.0061}(\mathrm{total})$
4	$97.7\ ^{+0.76}_{-0.98}(\mathrm{stat})$	$99.22^{+0.16}_{-0.18}(\mathrm{stat}) \pm 0.14(\mathrm{syst})$	$0.9846^{+0.0079}_{-0.0099}(\mathrm{total})$

$p_{\mathrm{T}}^{\mathrm{Jet}}$/GeV Bins	$\varepsilon_{\mathrm{ID}}^{\mathrm{Data}}$ in %	$\varepsilon_{\mathrm{ID}}^{\mathrm{MC}}$ in %	Scale Factors
20–30	$98.21^{+0.45}_{-0.54}(\mathrm{stat})$	$98.87^{+0.11}_{-0.12}(\mathrm{stat}) \pm 0.10(\mathrm{syst})$	$0.9934^{+0.0048}_{-0.0056}(\mathrm{total})$
30–40	$99.25^{+0.38}_{-0.55}(\mathrm{stat})$	$98.96^{+0.16}_{-0.17}(\mathrm{stat}) \pm 0.05(\mathrm{syst})$	$1.0026^{+0.0042}_{-0.0059}(\mathrm{total})$
40–50	$99.25^{+0.43}_{-0.69}(\mathrm{stat})$	$98.98^{+0.2}_{-0.23}(\mathrm{stat}) \pm 0.24(\mathrm{syst})$	$1.0027^{+0.0055}_{-0.0077}(\mathrm{total})$
50–70	$98.77^{+0.59}_{-0.87}(\mathrm{stat})$	$98.98^{+0.19}_{-0.22}(\mathrm{stat}) \pm 0.34(\mathrm{syst})$	$0.9979^{+0.0072}_{-0.0096}(\mathrm{total})$
70–90	$97.69^{+1.10}_{-1.61}(\mathrm{stat})$	$99.17^{+0.24}_{-0.29}(\mathrm{stat}) \pm 0.34(\mathrm{syst})$	$0.9851^{+0.0118}_{-0.0165}(\mathrm{total})$
90–120	$100.0^{+0.00}_{-1.44}(\mathrm{stat})$	$98.73^{+0.38}_{-0.47}(\mathrm{stat}) \pm 2.89(\mathrm{syst})$	$1.0129^{+0.0297}_{-0.0197}(\mathrm{total})$
120–160	$97.78^{+1.60}_{-3.16}(\mathrm{stat})$	$99.5\ ^{+0.28}_{-0.46}(\mathrm{stat}) \pm 2.89(\mathrm{syst})$	$0.9827^{+0.0334}_{-0.0316}(\mathrm{total})$
160–200	$100.0^{+0.00}_{-5.87}(\mathrm{stat})$	$97.73^{+1.08}_{-1.58}(\mathrm{stat}) \pm 2.89(\mathrm{syst})$	$1.0233^{+0.0338}_{-0.0657}(\mathrm{total})$

Table A.7.: Inner detector efficiency with statistical and systematical errors and scale factors in data and Monte Carlo in bins of # of jets and leading jet p_{T}.

η Bins	$\varepsilon_{\mathrm{ID}}^{\mathrm{Data}}$ in %	$\varepsilon_{\mathrm{ID}}^{\mathrm{MC}}$ in %	Scale Factors
-2.5 – -2.3	$96.12^{+1.63}_{-2.24}$(stat)	$97.16^{+0.53}_{-0.6}$(stat) $\pm$ 0.42(syst)	$0.9893^{+0.0182}_{-0.0238}$(total)
-2.3 – -2.1	$100.0^{+0.00}_{-0.61}$(stat)	$98.92^{+0.24}_{-0.28}$(stat) $\pm$ 0.19(syst)	$1.0109^{+0.0034}_{-0.007}$(total)
-2.1 – -1.9	$98.28^{+0.61}_{-0.80}$(stat)	$98.93^{+0.17}_{-0.19}$(stat) $\pm$ 0.08(syst)	$0.9935^{+0.0065}_{-0.0083}$(total)
-1.9 – -1.7	$98.89^{+0.53}_{-0.79}$(stat)	$99.5^{+0.13}_{-0.15}$(stat) $\pm$ 0.15(syst)	$0.9937^{+0.0057}_{-0.0081}$(total)
-1.7 – -1.5	$98.53^{+0.70}_{-1.03}$(stat)	$99.14^{+0.18}_{-0.20}$(stat) $\pm$ 0.09(syst)	$0.9939^{+0.0074}_{-0.0106}$(total)
-1.5 – -1.3	$98.94^{+0.60}_{-0.97}$(stat)	$98.82^{+0.23}_{-0.26}$(stat) $\pm$ 0.07(syst)	$1.0012^{+0.0067}_{-0.0101}$(total)
-1.3 – -1.1	$98.40^{+0.90}_{-1.45}$(stat)	$98.01^{+0.41}_{-0.47}$(stat) $\pm$ 0.42(syst)	$1.004^{+0.0113}_{-0.0160}$(total)
-1.1 – -0.9	$100.0^{+0.00}_{-0.71}$(stat)	$99.34^{+0.19}_{-0.23}$(stat) $\pm$ 0.39(syst)	$1.0067^{+0.0046}_{-0.0084}$(total)
-0.9 – -0.7	$100.0^{+0.00}_{-0.47}$(stat)	$99.56^{+0.13}_{-0.16}$(stat) $\pm$ 0.09(syst)	$1.0045^{+0.0018}_{-0.0050}$(total)
-0.7 – -0.5	$99.68^{+0.23}_{-0.47}$(stat)	$99.17^{+0.15}_{-0.17}$(stat) $\pm$ 0.34(syst)	$1.0052^{+0.0045}_{-0.0061}$(total)
-0.5 – -0.3	$99.21^{+0.38}_{-0.56}$(stat)	$99.1^{+0.14}_{-0.16}$(stat) $\pm$ 0.09(syst)	$1.0011^{+0.0042}_{-0.0059}$(total)
-0.3 – -0.1	$98.93^{+0.46}_{-0.64}$(stat)	$99.55^{+0.09}_{-0.11}$(stat) $\pm$ 0.04(syst)	$0.9938^{+0.0047}_{-0.0064}$(total)
-0.1 – 0.1	$96.7^{+1.09}_{-1.39}$(stat)	$94.68^{+0.42}_{-0.44}$(stat) $\pm$ 0.60(syst)	$1.0213^{+0.0141}_{-0.0169}$(total)
0.1 – 0.3	$99.12^{+0.43}_{-0.63}$(stat)	$99.57^{+0.09}_{-0.11}$(stat) $\pm$ 0.21(syst)	$0.9954^{+0.0049}_{-0.0067}$(total)
0.3 – 0.5	$99.71^{+0.21}_{-0.43}$(stat)	$99.88^{+0.05}_{-0.06}$(stat) $\pm$ 0.06(syst)	$0.9983^{+0.0023}_{-0.0044}$(total)
0.5 – 0.7	$99.64^{+0.26}_{-0.53}$(stat)	$99.66^{+0.09}_{-0.12}$(stat) $\pm$ 0.15(syst)	$0.9999^{+0.0033}_{-0.0057}$(total)
0.7 – 0.9	$99.57^{+0.32}_{-0.64}$(stat)	$99.51^{+0.13}_{-0.16}$(stat) $\pm$ 0.30(syst)	$1.0005^{+0.0047}_{-0.0073}$(total)
0.9 – 1.1	$100.0^{+0.00}_{-0.72}$(stat)	$99.37^{+0.18}_{-0.22}$(stat) $\pm$ 0.17(syst)	$1.0064^{+0.0028}_{-0.0077}$(total)
1.1 – 1.3	$93.62^{+2.22}_{-2.84}$(stat)	$97.38^{+0.48}_{-0.54}$(stat) $\pm$ 0.95(syst)	$0.9614^{+0.0246}_{-0.0301}$(total)
1.3 – 1.5	$99.52^{+0.35}_{-0.71}$(stat)	$98.49^{+0.25}_{-0.29}$(stat) $\pm$ 0.12(syst)	$1.0104^{+0.0048}_{-0.0078}$(total)
1.5 – 1.7	$99.65^{+0.25}_{-0.52}$(stat)	$99.42^{+0.12}_{-0.16}$(stat) $\pm$ 0.19(syst)	$1.0024^{+0.0036}_{-0.0057}$(total)
1.7 – 1.9	$98.73^{+0.54}_{-0.75}$(stat)	$99.43^{+0.13}_{-0.16}$(stat) $\pm$ 0.35(syst)	$0.9929^{+0.0066}_{-0.0084}$(total)
1.9 – 2.1	$96.15^{+1}_{-1.19}$(stat)	$98.81^{+0.19}_{-0.21}$(stat) $\pm$ 0.16(syst)	$0.9731^{+0.0102}_{-0.0120}$(total)
2.1 – 2.3	$98.91^{+0.61}_{-0.99}$(stat)	$99.54^{+0.18}_{-0.24}$(stat) $\pm$ 0.52(syst)	$0.9937^{+0.0084}_{-0.0109}$(total)
2.3 – 2.5	$97.98^{+1.14}_{-1.82}$(stat)	$99.1^{+0.38}_{-0.54}$(stat) $\pm$ 0.65(syst)	$0.9887^{+0.0142}_{-0.0197}$(total)

Table A.8.: Inner detector efficiency with statistical and systematical errors and scale factors in data and Monte Carlo in bins of η.

$p_{\mathrm{T}}/\mathrm{GeV}$ Bins	$\varepsilon_{\mathrm{Calo}}^{\mathrm{Data}}$ in %	$\varepsilon_{\mathrm{Calo}}^{\mathrm{MC}}$ in %	Scale Factors
20–25	$95.89^{+0.88}_{-1.02}$(stat)	$94.83^{+0.37}_{-0.39}$(stat)	$1.0112^{+0.0103}_{-0.0116}$(total)
25–30	$98.49^{+0.43}_{-0.53}$(stat)	$96.26^{+0.25}_{-0.26}$(stat)	$1.0232^{+0.0053}_{-0.0062}$(total)
30–35	$99.06^{+0.3}_{-0.38}$(stat)	$98.41^{+0.13}_{-0.14}$(stat)	$1.0066^{+0.0034}_{-0.0041}$(total)
35–40	$99.3\ ^{+0.22}_{-0.28}$(stat)	$99.08^{+0.091}_{-0.09}$(stat)	$1.0022^{+0.0024}_{-0.003}$(total)
40–60	$99.19^{+0.17}_{-0.19}$(stat)	$99.40^{+0.04}_{-0.05}$(stat)	$0.9979^{+0.0018}_{-0.0020}$(total)
60–100	$99.11^{+0.43}_{-0.63}$(stat)	$98.66^{+0.18}_{-0.20}$(stat)	$1.0045^{+0.0048}_{-0.0067}$(total)

ϕ Bins	$\varepsilon_{\mathrm{Calo}}^{\mathrm{Data}}$ in %	$\varepsilon_{\mathrm{Calo}}^{\mathrm{MC}}$ in %	Scale Factors
-3.5 – -2.5	$98.89^{+0.37}_{-0.48}$(stat)	$98.5\ ^{+0.15}_{-0.16}$(stat)	$1.0040^{+0.0041}_{-0.0051}$(total)
-2.5 – -1.5	$98.78^{+0.32}_{-0.39}$(stat)	$98.71^{+0.11}_{-0.12}$(stat)	$1.0007^{+0.0035}_{-0.0041}$(total)
-1.5 – -0.5	$98.65^{+0.35}_{-0.43}$(stat)	$98.28^{+0.13}_{-0.14}$(stat)	$1.0038^{+0.0039}_{-0.0046}$(total)
-0.5 – 0.5	$98.44^{+0.37}_{-0.44}$(stat)	$98.78^{+0.11}_{-0.11}$(stat)	$0.9965^{+0.0039}_{-0.0045}$(total)
0.5 – 1.5	$99.22^{+0.26}_{-0.34}$(stat)	$98.80^{+0.11}_{-0.11}$(stat)	$1.0042^{+0.0029}_{-0.0036}$(total)
1.5 – 2.5	$98.82^{+0.32}_{-0.39}$(stat)	$98.46^{+0.12}_{-0.13}$(stat)	$1.0037^{+0.0035}_{-0.0042}$(total)
2.5 – 3.5	$99.55^{+0.22}_{-0.32}$(stat)	$98.82^{+0.13}_{-0.14}$(stat)	$1.0074^{+0.0026}_{-0.0035}$(total)

ΔR Bins	$\varepsilon_{\mathrm{Calo}}^{\mathrm{Data}}$ in %	$\varepsilon_{\mathrm{Calo}}^{\mathrm{MC}}$ in %	Scale Factors
0.5–1.0	$98.36^{+0.41}_{-0.5}$(stat)	$97.99^{+0.15}_{-0.15}$(stat)	$1.0038^{+0.0045}_{-0.0053}$(total)
1.0–1.5	$98.76^{+0.30}_{-0.36}$(stat)	$98.65^{+0.10}_{-0.11}$(stat)	$1.0011^{+0.0033}_{-0.0038}$(total)
1.5–2.0	$98.68^{+0.33}_{-0.40}$(stat)	$98.59^{+0.11}_{-0.12}$(stat)	$1.0009^{+0.0036}_{-0.0042}$(total)
2.0–2.5	$98.94^{+0.32}_{-0.39}$(stat)	$98.48^{+0.12}_{-0.13}$(stat)	$1.0046^{+0.0035}_{-0.0042}$(total)
2.5–3.0	$99.07^{+0.31}_{-0.40}$(stat)	$98.87^{+0.12}_{-0.13}$(stat)	$1.0020^{+0.0034}_{-0.0042}$(total)
3.0–3.5	$98.82^{+0.46}_{-0.62}$(stat)	$99.01^{+0.15}_{-0.16}$(stat)	$0.9981^{+0.0049}_{-0.0064}$(total)
3.5–4.0	$99.16^{+0.61}_{-1.24}$(stat)	$99.14^{+0.24}_{-0.30}$(stat)	$1.0002^{+0.0069}_{-0.0127}$(total)
4.0–4.5	$100.0^{+0.00}_{-2.23}$(stat)	$98.62^{+0.49}_{-0.64}$(stat)	$1.014\ ^{+0.0065}_{-0.0234}$(total)
4.5–5.0	$100.0^{+0.00}_{-4.67}$(stat)	$98.34^{+0.64}_{-0.86}$(stat)	$1.0169^{+0.0087}_{-0.0488}$(total)

Table A.9.: Calorimeter tagged muon efficiency with statistical and systematical errors and scale factors in data and Monte Carlo in bins of p_{T}, ϕ and ΔR.

# of Jets	$\varepsilon_{\text{Calo}}^{\text{Data}}$ in %	$\varepsilon_{\text{Calo}}^{\text{MC}}$ in %	Scale Factors
0	$99.41^{+0.23}_{-0.31}$(stat)	$99.02^{+0.12}_{-0.13}$(stat)	$1.0039^{+0.0027}_{-0.0034}$(total)
1	$98.72^{+0.36}_{-0.45}$(stat)	$99.1\ ^{+0.11}_{-0.12}$(stat)	$0.9962^{+0.0038}_{-0.0046}$(total)
2	$99.38^{+0.26}_{-0.37}$(stat)	$98.72^{+0.15}_{-0.16}$(stat)	$1.0067^{+0.0032}_{-0.0041}$(total)
3	$99.51^{+0.28}_{-0.45}$(stat)	$98.38^{+0.2}_{-0.22}$(stat)	$1.0115^{+0.0036}_{-0.0050}$(total)
4	$98.68^{+0.56}_{-0.78}$(stat)	$98.96^{+0.18}_{-0.21}$(stat)	$0.9972^{+0.0060}_{-0.0081}$(total)

$p_{\text{T}}^{\text{Jet}}$ Bins	$\varepsilon_{\text{Calo}}^{\text{Data}}$ in %	$\varepsilon_{\text{Calo}}^{\text{MC}}$ in %	Scale Factors
20–30	$97.46^{+0.53}_{-0.62}$(stat)	$97.38^{+0.17}_{-0.18}$(stat)	$1.0009^{+0.0058}_{-0.0066}$(total)
30–40	$98.69^{+0.51}_{-0.68}$(stat)	$96.41^{+0.29}_{-0.30}$(stat)	$1.0236^{+0.0062}_{-0.0078}$(total)
40–50	$96.69^{+0.98}_{-1.21}$(stat)	$96.52^{+0.37}_{-0.4}$(stat)	$1.0018^{+0.0109}_{-0.0131}$(total)
50–70	$97.96^{+0.79}_{-1.05}$(stat)	$94.57^{+0.45}_{-0.48}$(stat)	$1.0359^{+0.01}_{-0.0125}$(total)
70–90	$93.99^{+1.85}_{-2.29}$(stat)	$95.86^{+0.55}_{-0.6}$(stat)	$0.9805^{+0.0199}_{-0.0241}$(total)
90–120	$96.15^{+1.82}_{-2.63}$(stat)	$94.09^{+0.85}_{-0.93}$(stat)	$1.022\ ^{+0.0221}_{-0.0299}$(total)
120–160	$93.33^{+3.11}_{-4.39}$(stat)	$96.74^{+0.82}_{-0.97}$(stat)	$0.9648^{+0.0326}_{-0.0446}$(total)
160–200	$94.44^{+3.91}_{-7.29}$(stat)	$96.21^{+1.45}_{-1.92}$(stat)	$0.9816^{+0.0446}_{-0.0759}$(total)

Table A.10.: Calorimeter tagged muon efficiency with statistical and systematical errors and scale factors in data and Monte Carlo in bins of # of jets an leading jet p_{T}.

η Bins	$\varepsilon_{\text{Calo}}^{\text{Data}}$ in %	$\varepsilon_{\text{Calo}}^{\text{MC}}$ in %	Scale Factors
-2.5 – -2.3	$98.06^{+1.09}_{-1.75}$(stat)	$98.64^{+0.36}_{-0.43}$(stat)	$0.9941^{+0.0118}_{-0.018}$(total)
-2.3 – -2.1	$100.0^{+0.00}_{-0.61}$(stat)	$99.22^{+0.2}_{-0.24}$(stat)	$1.0079^{+0.0024}_{-0.0065}$(total)
-2.1 – -1.9	$97.99^{+0.67}_{-0.85}$(stat)	$98.72^{+0.18}_{-0.20}$(stat)	$0.9927^{+0.0070}_{-0.0088}$(total)
-1.9 – -1.7	$99.26^{+0.42}_{-0.68}$(stat)	$98.58^{+0.22}_{-0.25}$(stat)	$1.0069^{+0.005}_{-0.0073}$(total)
-1.7 – -1.5	$98.53^{+0.70}_{-1.03}$(stat)	$98.52^{+0.23}_{-0.26}$(stat)	$1.0001^{+0.0076}_{-0.0108}$(total)
-1.5 – -1.3	$99.47^{+0.39}_{-0.79}$(stat)	$97.88^{+0.31}_{-0.34}$(stat)	$1.0163^{+0.0053}_{-0.0088}$(total)
-1.3 – -1.1	$98.40^{+0.90}_{-1.45}$(stat)	$96.22^{+0.57}_{-0.63}$(stat)	$1.0226^{+0.0116}_{-0.0165}$(total)
-1.1 – -0.9	$98.14^{+0.89}_{-1.30}$(stat)	$98.14^{+0.33}_{-0.37}$(stat)	$0.9999^{+0.0098}_{-0.0137}$(total)
-0.9 – -0.7	$98.76^{+0.6}_{-0.88}$(stat)	$99.38^{+0.15}_{-0.18}$(stat)	$0.9937^{+0.0062}_{-0.0089}$(total)
-0.7 – -0.5	$98.74^{+0.54}_{-0.75}$(stat)	$98.31^{+0.22}_{-0.24}$(stat)	$1.0043^{+0.0060}_{-0.008}$(total)
-0.5 – -0.3	$98.68^{+0.51}_{-0.69}$(stat)	$99.07^{+0.14}_{-0.16}$(stat)	$0.9960^{+0.0054}_{-0.0070}$(total)
-0.3 – -0.1	$99.46^{+0.30}_{-0.49}$(stat)	$98.94^{+0.14}_{-0.16}$(stat)	$1.0053^{+0.0035}_{-0.0052}$(total)
-0.1 – 0.1	$100.0^{+0.00}_{-0.54}$(stat)	$98.88^{+0.19}_{-0.21}$(stat)	$1.0113^{+0.0022}_{-0.0058}$(total)
0.1 – 0.3	$100.0^{+0.00}_{-0.34}$(stat)	$98.85^{+0.15}_{-0.17}$(stat)	$1.0116^{+0.0017}_{-0.0038}$(total)
0.3 – 0.5	$98.83^{+0.5}_{-0.69}$(stat)	$98.95^{+0.15}_{-0.17}$(stat)	$0.9989^{+0.0053}_{-0.0072}$(total)
0.5 – 0.7	$100.0^{+0.00}_{-0.41}$(stat)	$98.68^{+0.19}_{-0.21}$(stat)	$1.0133^{+0.0022}_{-0.0046}$(total)
0.7 – 0.9	$98.70^{+0.62}_{-0.92}$(stat)	$97.7\ ^{+0.30}_{-0.33}$(stat)	$1.0103^{+0.0073}_{-0.01}$(total)
0.9 – 1.1	$98.74^{+0.71}_{-1.14}$(stat)	$98.86^{+0.25}_{-0.29}$(stat)	$0.9988^{+0.0077}_{-0.0118}$(total)
1.1 – 1.3	$93.62^{+2.22}_{-2.84}$(stat)	$95.56^{+0.62}_{-0.69}$(stat)	$0.9797^{+0.0239}_{-0.0299}$(total)
1.3 – 1.5	$99.52^{+0.35}_{-0.71}$(stat)	$98.3\ ^{+0.27}_{-0.30}$(stat)	$1.0124^{+0.0047}_{-0.0078}$(total)
1.5 – 1.7	$99.65^{+0.25}_{-0.52}$(stat)	$98.48^{+0.23}_{-0.25}$(stat)	$1.0119^{+0.0037}_{-0.0058}$(total)
1.7 – 1.9	$99.05^{+0.46}_{-0.67}$(stat)	$98.86^{+0.19}_{-0.22}$(stat)	$1.0019^{+0.0051}_{-0.0071}$(total)
1.9 – 2.1	$97.12^{+0.85}_{-1.06}$(stat)	$98.98^{+0.17}_{-0.19}$(stat)	$0.9812^{+0.0087}_{-0.0106}$(total)
2.1 – 2.3	$99.46^{+0.4}_{-0.81}$(stat)	$98.62^{+0.33}_{-0.39}$(stat)	$1.0085^{+0.0056}_{-0.0089}$(total)
2.3 – 2.5	$96.97^{+1.44}_{-2.09}$(stat)	$98.65^{+0.48}_{-0.63}$(stat)	$0.9830^{+0.0157}_{-0.0214}$(total)

Table A.11.: Calorimeter tagged muon efficiency with statistical and systematical errors and scale factors in data and Monte Carlo in bins of η.

List of Figures

List of Tables

Bibliography

[1] D. Griffiths. *Introduction to Elementary Particles*. 2008.

[2] The ATLAS Collaboration. Discovery Reach for Black Hole Production. In *Expected performance of the ATLAS experiment: detector, trigger and physics*, pages 1803–1828, 2008.

[3] A. Einstein. Die Grundlage der allgemeinen Relativitätstheorie (The foundation of the general theory of relativity). *AdP*, **14**:517–571, 1916.

[4] Y. Fukuda and T. Hayakawa. Solar neutrino data covering solar cycle 22. *Phys. Rev. Lett.*, 77(9):1683–1686, 1996.

[5] K. Nakamura *et al.* (Particle Data Group). *J. Phys. G*, **37**, 075021, 2010.

[6] R. Alkofer and J. Greensite. Quark Confinement: The Hard Problem of Hadron Physics. *J. Phys. G*, **34** S3, 2007. arXiv:hep-ph/0610365v2.

[7] G. P. Salam. Perturbative QCD for the LHC. arXiv:hep-ph/1103.1318v1.

[8] S. Dawson. Radiative corrections to Higgs Boson production. *Nucl. Phys. B*, **359**:283, 1991.

[9] M. Rubin, G. P. Salam, S. Sapeta. Giant QCD K-factors beyond NLO. arXiv:hep-ph/1006.2144v2.

[10] M. Dasgupta, L. Magnea, G. P. Salam. Non-perturbative QCD effects in jets at hadron colliders. *JHEP*, **2**, 2008. arXiv:hep-ph/0712.3014v1.

[11] S. L. Glashow. Partial-symmetries of weak interactions. *Nuclear Physics*, **22**(4):579 – 588, 1961.

[12] S. Weinberg. A Model of Leptons. *Phys. Rev. Lett.*, **19**(21):1264–1266, 1967.

[13] A. Salam. Weak and Electromagnetic Interactions. *Elementary Particle Theory*, 1968.

[14] The Nobel Prize in Physics 1979. Nobelprize.org. 18 May 2011. *http://nobelprize.org*.

[15] E. Fermi. Versuch einer Theorie der Betastrahlen. *Zeitschrift für Physik*, **88**:161, 1934.

[16] F. L. Wilson. Fermi's Theory of Beta Decay. *American Journal of Physics*, **36**:1150–1160, 1968.

[17] J. W. Moffat. Finite nonlocal gauge field theory. *Phys. Rev. D*, **41**(4):1177–1184, Feb 1990.

[18] L. Evans and P. Bryant. LHC machine. *JINST*, **3** S08001, 2008.

[19] The ATLAS Collaboration. The ATLAS experiment at the CERN Large Hadron Collider. *JINST*, **3** S08003, 2008.

[20] The CMS Collaboration. The CMS experiment at the CERN LHC. *JINST*, **3** S08004, 2008.

[21] The ALICE Collaboration. The ALICE experiment at the CERN LHC. *JINST*, **3** S08002, 2008.

[22] The LHCb Collaboration. The LHCb Detector at the LHC. *JINST*, **3** S08005, 2008.

[23] ATLAS Experiment © 2011 CERN. *http://www.atlas.ch/photos/*.

[24] G. Aad *et. al*, editor. *Expected performance of the ATLAS experiment: detector, trigger and physics*, Geneva, 2009. CERN.

[25] *http://root.cern.ch/*.

[26] ATLAS Collaboration. ATLAS detector and physics performance - Technical Design Report. 1, 25 May 1999.

[27] The ATLAS Collaboration. Muon Reconstruction and Identification: Studies with Monte Carlo Samples. In *Expected performance of the ATLAS experiment: detector, trigger and physics*, pages 162–184, 2008.

[28] T. Lagouri *et al*. A muon identification and combined reconstruction procedure for the ATLAS detector at the LHC at CERN. *IEEE Transactions on Nuclear Science*, **51**(6):3030–3033, 2004.

[29] S. Hassini *et al*. A muon identification and combined reconstruction procedure for the ATLAS detector at the LHC using the (MUONBOY, STACO, MuTag) reconstruction packages. *NIM A*, **572**:77–79.

[30] The ATLAS Collaboration. Muons in the Calorimeters: Energy Loss Corrections and Muon Tagging. In *Expected performance of the ATLAS experiment: detector, trigger and physics*, pages 185–207, 2008.

[31] M. Cacciari and G. P. Salam. The anti-k_t jet clustering algorithm. *JHEP*. arXiv:hep-ph/0802.1189v2.

[32] S. D. Ellis, D. E. Soper. Successive Combination Jet Algorithm For Hadron Collisions. *Phys.Rev.D*, **48**:3160–3166, 1993. arXiv:hep-ph/9305266v1.

[33] Y. L. Dokshitzer, G. D. Leder, S. Moretti, B. R. Webber. Better Jet Clustering Algorithms. *JHEP **9708** 001*, 1997. arXiv:hep-ph/9707323v2.

[34] M. Wobisch, T. Wengler. Hadronization Corrections to Jet Cross Sections in Deep-Inelastic Scattering. http://arxiv.org/abs/hep-ph/9907280v1.

[35] G. C. Blazey *et al.* Run II Jet Physics: Proceedings of the Run II QCD and Weak Boson Physics Workshop. http://arxiv.org/abs/hep-ex/0005012v2.

[36] J. Fleckner. Performance of Track and Vertex Reconstruction and b-Tagging Studies with ATLAS in pp Collisions at $\sqrt{s}$ = 7 TeV. Technical report, CERN, Geneva, 2010.

[37] N. Metropolis and S. Ulam. The Monte Carlo Method. *Journal of the American Statistical Association*, **44**(247):335–341, Sep. 1949.

[38] S. Agostinelli *et al.* Geant4—a simulation toolkit. *Nuclear Instruments and Methods in Physics Research A*, 506:250–303, 2003.

[39] T. Sjöstrand. A Brief Introduction to PYTHIA 8.1. arXiv:hep-ph/0710.3820v1.

[40] T. Sjöstrand. PYTHIA 6.4 Physics and Manual. arXiv:hep-ph/0603175v2.

[41] S. Frixione and B. R. Webber. Matching NLO QCD computations and parton shower simulations. *JHEP*, **06**(029), 2002. arxiv:hep-ph/0204244.

[42] M. L. Mangano, M. Moretti, F. Piccinini, R. Pittau, A.D. Polosa. ALPGEN, a generator for hard multiparton processes in hadronic collisions. atXiv:hep-ph/0206293v2.

[43] C. J. Clopper and E. S. Pearson. The use of confidence or fiducial limits illustrated in the case of the binomial. *Biometrika*, **26**(4):404–413, 1934.

Danksagung

Zu allererst gilt mein Dank natürlich Prof. Michael Kobel, Dr. Anja Vest und dem gesamten Institut für Kern- und Teilchenphysik, die mir meine Diplomarbeit, insbesondere als Teil der ATLAS-Kollaboration, ermöglicht haben. Vor allem Prof. Kobel hat mit seiner Einführungsvorlesung mein Interesse an der Teilchenphysik geweckt. Jun.-Prof. Arno Straessner möchte ich für die Möglichkeit danken, sowohl das Laborpraktikum des IKTP als auch eine Exkursion an das CERN als Betreuer begleiten zu können.

Desweiteren gilt mein Dank sowohl Peter Steinbach, durch dessen starkes Engagement für das institutsinterne Software Café ich sehr viel lernen konnte, als auch Christian Rudolph, der immer für anregende Diskussionen zur Verfügung stand, sowie Tobias Reinhardt und Frank Seifert, die zu einem phantastischen Büroklima beigetragen haben.

Zum Schluss aber nicht zuletzt gilt ganz besonderer Dank auch meinen Eltern und Großeltern, die immer an mich geglaubt haben und ohne deren Unterstützung ich es sicher nie soweit gebracht hätte.

Erklärung

Hiermit versichere ich, dass ich die vorliegende Arbeit ohne unzulässige Hilfe Dritter und ohne Benutzung anderer als der angegebenen Hilfsmittel angefertigt habe. Die aus fremden Quellen direkt oder indirekt übernommenen Gedanken sind als solche kenntlich gemacht. Die Arbeit wurde bisher weder im Inland noch im Ausland in gleicher oder ähnlicher Form einer anderen Prüfungsbehörde vorgelegt.

Tino Michael
Dresden, August 2011